Chapter 2: Overview of Atmospheric Ionizing Radiation (*AIR*)

J. W. Wilson*, D. L. Maiden*, P. Goldhagen, H. Tai*, J. L. Shinn***

***NASA Langley Research Center, Hampton, VA 23681**
****DOE Environmental Measurements Laboratory, New York, NY 10014**

Overview of Atmospheric Ionizing Radiation (*AIR*)

Preface

The SuperSonic Transport (SST) development program within the US was based at the Langley Research Center as was the Apollo radiation testing facility (Space Radiation Effects Laboratory) with associated radiation research groups. It was natural for the issues of the SST to be first recognized by this unique combination of research programs. With a re-examination of the technologies for commercial supersonic flight and the possible development of a High Speed Civil Transport (HSCT), the remaining issues of the SST required resolution. It was the progress of SST radiation exposure research program founded by T. Foelsche at the Langley Research Center and the identified remaining issues after that project over twenty-five years ago which became the launch point of the current atmospheric ionizing radiation (*AIR*) research project. Added emphasis to the need for reassessment of atmospheric radiation resulted from the major lowering of the recommended occupational exposure limits, the inclusion of aircrew as radiation workers, and the recognition of civil aircrew as a major source of occupational exposures. Furthermore, the work of Ferenc Hajnal of the Environmental Measurements Laboratory brought greater focus to the uncertainties in the neutron flux at high altitudes. A re-examination of the issues involved was committed at the Langley Research Center and by the National Council on Radiation Protection (NCRP). As a result of the NCRP review, a new flight package was assembled and flown during solar minimum at which time the galactic cosmic radiation is at a maximum (June 1997). The present workshop is the initial analysis of the new data from that flight. The present paper is an overview of the status of knowledge of atmospheric ionizing radiations. We will re-examine the exposures of the world population and examine the context of aircrew exposures with implications for the results of the present research. A condensed version of this report was given at the 1998 Annual Meeting of the NCRP with proceedings published in the journal of *Health Physics* (Wilson 2000).

Introduction

Within a year of the discovery of X-rays comes reports of adverse biological consequences such as dermatitis, smarting of the eyes, and epilation followed by the first reported cancer within an X-ray produced ulcer (von Frieben 1903) and other adverse biological consequences (Upton 1989). As a result, various national and international commissions were established to provide protection guidelines against exposures to X-ray devices and radium (ICR 1928). These early recommendations were mainly to limit adverse consequences of acute exposures to individual workers and allowable limits remained high by today's standards. With the growing awareness of chronic exposure effects, the advent of nuclear technology, and the expansion of medical technology in the mid-twentieth century the recommended allowable limits of exposure were reduced dramatically (by 1/3 from 1934 to 1950 and a further factor of 3 by 1958, ICRP 1991). In the case of public exposures (non-occupational exposure) the judgement on acceptable limitations are based on the background levels experienced in ordinary life and great interest in understanding these exposures from natural radiation has developed over recent years. Furthermore, the largest contribution to exposure of human tissues is from the natural background since every living individual is

unavoidably exposed throughout their lifetime. The background exposures are important in assessing the natural radiation risks to the society at large for comparison with the added risks of a new process or technology (NCRP 1995). In addition to the development of nuclear and medical technologies, air and space travel result in elevated natural exposure levels, which have received greater attention in the last half of the twentieth century.

It had long been known that ions were present in the atmosphere since charged condensers (electrometers) would slowly discharge over a period of time. Furthermore the discharge rate was increased by the known radioactivity rays, cathode rays, and X-rays. Over most of the land mass approximately 10 to 20 ion pairs per cubic centimeter are formed every second. Assuming the Earth's natural radioactivity as the source, repeat of the experiments over bodies of water in fact reduced the electrometer discharge rate (Hess and Eugster 1949). The estimated attenuation of the most penetrating rays resulting from radioactivity in the atmosphere was 300 meters leading Th. Wulf, S.J. to compare discharge rates on the ground with those on top of the Eiffel Tower. He found the rate to be only half the ground level value and not a greatly reduced value as expected. Wulf rightly concluded that radiations must have been penetrating from the top of the atmosphere, although that interpretation was controversial. Balloon flight data was obtained by various investigators, but it was not until V. F. Hess developed an adequate electrometer experiment able to operate in the temperature and pressure extremes at balloon altitudes that conclusive evidence was found of radiations arriving at the top of the Earth's atmosphere. Hess's studies found the ionization rates to decrease with altitude up to 500 meters followed by a steady increase at higher altitudes to where the ground level rate is matched at 1500 meters. For this discovery, Hess would receive a Noble prize in physics (1936). Observations during a solar eclipse (incorrectly) brought the conclusion that the source was not the sun (solar cosmic rays arrive nearly isotropically) and probably came from deep space and the term "cosmic radiation" came into use in 1926 (Hess and Eugster 1949). Prior to this date the term "high altitude radiation" was in common use. J. Clay would discover that the ionization rates were smaller at lower latitudes in several voyages from Europe to the Dutch Indies in the period of 1927-1929 demonstrating that many of the rays are charged resulting in deflection in the geomagnetic field near the equator and allowing greater access in polar regions (Hess and Eugster 1949).

In the electrometer experiments, it was found that fresh air would result in faster discharge rates than older air (Hess and Eugster 1949). This is now understood to be due to short lived radon decay products and cosmogenic radioisotopes produced by the cosmic rays from atmospheric atoms. These are later recognized as important sources of human exposures.

That the cosmic rays consisted in part of charged particles was directly demonstrated by coincidence experiments using Geiger-Mueller tubes and resolving individual charged particle tracks within a Wilson cloud chamber. The cloud chamber lead to the discovery of the positron as part of the cosmic rays, followed by the discovery of the charged mesons, and further shed light on the important neutron component of the cosmic radiations in the atmosphere (Bethe et al. 1940). Worldwide surveys of cosmic ionization during the years 1931-1932 were made by several groups and Hess of Austria studied time variations associated with solar activity cycle on a mountaintop from 1931-1937. Global radiation levels correlated well with the expected effects of the geomagnetic deflection of cosmic radiations. A world wide network of stations began to develop leading to observed short term fluctuations

in the global ionization rates simultaneously in both the southern and northern hemispheres and correlated with solar disturbances (Hess and Eugster 1949). Observed large increases in the ionization rates would be attributed to particles coming directly from the solar events (figure 1) while more modest decreases over a few days as seen for the July-August 1946 event were attributed to disturbance of the local interplanetary medium by which approaching cosmic rays were excluded from the local Earth environment (Forbush decrease). It was now clear that extraterrestrial radiations from both the sun and the galaxy were contributing to the atmospheric ionization levels. The next-to-last piece of important evidence from a human exposure perspective was the discovery of heavy ion tracks by Phyllis Frier and coworkers (1948) using nuclear emulsion track detectors in high altitude balloon flight. Although the initial emphasis of this discovery was the ability to sample cosmic matter, attention would turn to the possibility of human exposure by these ions in high altitude aircraft and future space travel (Armstrong et al. 1949, Schaefer 1950).

E. Goldstein introduced the term "cathode rays" at the time (1876) of his discovery of the canal rays (positive ion beams, Hess and Eugster 1949). He suggested (incorrectly) that "cathode rays" from the sun were responsible for the observed aurora. C. Störmer (1955) studied the equations of charged particle motion in the geomagnetic field to understand the auroral patterns and found a general equation for the solutions that were open to asymptotic motion. He also found solutions which were bound with no asymptotic solution which he (incorrectly) recognized as not contributing to aurora but failed to suggest that these regions may be filled with trapped particles which are in fact the source of the aurora during conditions of extreme geomagnetic disturbance. The trapped radiations were directly observed by the first US satellite with a Geiger-Mueller tube (Van Allen et al. 1958) and are largely confined to the "forbidden" regions of Störmer's theory on the motion of charged particles in a magnetic dipole field (left hand proton contours in figure 2). The inner zone particles shown on the left of figure 2 consist of stable trapped radiations while the so-called outer zone particles on the right of figure 2 consist of a transient zone where particles of the solar wind are inserted into the magnetosphere through the geomagnetic tail and radially diffuse inward until they are depleted by precipitation into the Earth's atmosphere near the poles. It is these outer zone particles that mainly form the aurorae during geomagnetic disturbances.

Since the discovery of the magnetically trapped radiations, no new sources of natural radiations important to human exposure have been found (except of course those of the same classes in other planetary bodies). Even so, human activity has enhanced human exposures to natural radiations due to technological development. In what follows we will give a quantitative presentation of the various components of natural radiations and the extent of human exposures. Special attention will be given to the quality of the radiations involved as this also relates to the interpretation of the associated risks. Of particular interest will be the comparison of the level of exposures and the radiation quality of various groups of exposed individuals.

In the present chapter we will review the sources of atmospheric radiation exposure where most human exposures occur. This will include sources in the lower atmosphere dominated by natural radioactivity to the higher altitudes incountered by aircraft. There will be special emphasis on the most biologically effective components.

The Origin of Atmospheric Radiation

Terrestrial Atmospheric Radiation Sources

Ionization in the lower atmosphere is dominated by radionuclides in the Earth's crust. Over deep water, there are few dissolved radionuclides so that the ionization is dominated by radiation incident on the top of the atmosphere. The ionization over the landmass is complicated and depends on many physical and chemical factors.

Natural radioactivity. The radioactive elements remaining from the formation of the Earth are sustained by the unusually long lifetimes of U-235, U-238, Th-232, Rb-87, and K-40. They are chemically bound and found in various mineral formations either in quantity or as trace elements in the bulk. The decay of U-235, U-238, and Th-232 consists of a complex sequence of events terminating with stable nuclei (see tables 1-3). The Rb-87 and K-40 decay through simple beta emission directly into stable isotopes. The decay sequences are determined by the binding properties of neutrons and protons in nuclear matter. Nuclear instability is characterized by an excess of either protons or neutrons over what is required for a stable configuration. Heavy nuclei tend to have more neutrons than protons since the proton charge leads to large repulsive forces tending towards nuclear instability and is the source of nuclear fission. An important decay mode is alpha particle decay (emission of a He-4 nucleus, which is unusually tightly bound). Emission of beta particles (electrons of both charges, negatrons and positrons) to reduce the nuclear neutron excess (negatron emission) or the nuclear coulomb repulsion (positron emission). Angular momentum conservation requirements often result in an excited nuclear state that must be reduced in energy by gamma ray emission.

Although the decay energies of these various processes are similar, the differing types of decay particles have vastly differing penetration powers. The penetration of charged decay products is limited by the interaction with atomic electrons. The alpha particles have typical ranges in air of few to several centimeters but only tens of micrometers in condensed material. As an external source, alpha particle emitters are relatively harmless. If ingested or inhaled and thereby brought into contact with sensitive cells the alpha particle emissions can be most hazardous. The typical emitted electron has a range in air of tens of centimeters to meters but at most a few centimeters in condensed matter. The decay electrons pose a limited hazard as an external source since they do not penetrate deeply into the body. The stopping positrons undergo annihilation events with atomic electrons in which two energetic gamma rays (0.511 MeV) are emitted. The nuclear-decay gamma rays as well as the energetic annihilation gamma rays have no charge resulting in a slower attenuation rate penetrating even hundreds of meters of air and passing through large thickness of condensed matter. Gamma rays are the major source of external exposure and a contributor to atmospheric radiation from naturally occurring radioactivity.

The radioactive nuclei are chemically bound and reside as minerals of the Earth's crust. As such they are generally immobile and limited in human exposure except as an external source. Indeed only the upper 25-cm of the crust provides the escaping gamma rays for exposure. This is true for all except the radioisotopes of Radon (Rn) which appear in all three decay sequences. Radon has a closed electronic shell structure and is therefore chemically inert and normally in a gaseous state but is still limited in movement by its physical interactions. Although the U-235,

U-238, and Th-232 decay sequences all pass through this noble gas, the atom is trapped within the mineral matrix with little chance of escape depending on the materials porosity. Generally diffusion within minerals occurs mainly along the grain boundaries wherein escape to the atmosphere or to ground water is possible. The decay of Radium (Ra) by alpha emission results in nuclear recoil of the Radon atom which near grain boundaries allows escape from the mineral matrix. The lifetimes of Rn–219 and Rn-220 are short allowing little time for escape prior to decay into chemically active Polonium. Consequently most exposure to radioactive alpha emission is related to the single isotope Rn-222.

Distribution of terrestrial radioactive nuclei. The Earth's mantle is a relatively uniform mixture of molten minerals. The formation of the crust in cooling processes differentiates among mineral content. The early formation of silicate crystals is rich in iron and magnesium (dark colored mafic rocks). Later cooling results in silicates rich in silicon and aluminum (light colored salic rocks). Final cooling provides silicates rich in potassium and rubidium. Thorium and uranium are incompatible with the silicate crystal structure and appear only as trace elements within the silicate rocks and reside mainly as constituents of minor minerals in which they are the main or important constituents. The identification of specific igneous rock types is an indicator of radioactivity content (see table 4).

Physical and chemical processes collectively known as weathering further separate mineral types. Erosion by water, wind and ice mechanically breaks down the grain sizes and separates them into weather resistant and subjective mineral grains. Although only slightly soluble in water, leaching by dissolution into unsaturated running water transports mineral types to sedimentation points with mixing with other sedimentation products. Weather resistant mineral grains such as zircon and monazite leads to small mineral grains rich in thorium and uranium ultimately appearing as small dense grains in coarse sands and gravel in alluvium. Dissolved thorium and uranium minerals add to the clay deposits. Thus weathering the igneous rock leads to sands depleted in radioactivity, fine clays rich in radioactivity, and dense grains rich in thorium and uranium. In addition, decomposing organic materials produce organic acids that form complexes with uranium minerals to increase their mobility.

Water carries dissolved minerals and mechanically reduced particulates to places with a downward thrust to where sedimentation occurs. The buildup of successive layers of sedimentation forms an insulating layer against the outward transport of heat from the mantle and increased pressure in the lower layers. This heat and pressure causes phase transitions resulting in new segregation of mineral types. Within this same general process is the formation of coal, crude oil, and natural gas. Uranium has a particular affinity to these organic products. The radionuclide content is reasonably correlated with sedimentary rock type as noted in table 4. Eighty-five percent of the US population lives over sedimentary bedrock, as does a majority of other national populations (see for example, van Dongen and Stoute 1985 and Ibrahiem et al. 1993).

Activity of the soil is related first to the rock from which it is produced but altered by leaching, dilution by organic root systems and the associated changes in water content, and augmented by sorption and precipitation (NCRP 1987, Weng et al. 1991). Soil is transported laterally by water and wind. Modified by human activities as

erosion, topsoil transport, and fertilizers. Biochemical processes modify activity several ways. Root systems increase porosity and water content. Humic acids decompose rock into smaller fragments increasing water content and leaching action. The lower soil is changed from an oxidizing to a reducing medium. The overall effect of natural soil development is to reduce the radioactivity. The activity of a specific soil type depends on the local region and the specific processes in action as seen by comparing same soil types in tables 5 and 6. Although geological maps based on the uppermost bed rock is useful for a general characterization of activity, it is not a reliable guide to quantitative evaluation.

Plants selectively take up radionuclides dissolved in water. The reducing action of floodwater in paddy rice greatly reduces the Tc-95 activity of the rice grain compared to upland rice (Yanagisawa and Muramatsu 1995). Similar reducing environments reduce the mobility of uranium. Leafy vegetables tend to have high concentration compared to non-leaf vegetables (Yanagisawa and Muramatsu 1993). Similar metabolic differences are expected for other radionuclides. Field corn was found to expire Rn-222 at a rate several times higher than the soil on which the corn was growing (Pearson 1967).

External exposures from terrestrial radiation. The larger fraction of the earth's surface where people live and work has as natural cover the soil resulting from weathering processes. As noted, the lower atmospheric radiation and the associated external exposures are mainly from gamma rays emitted from the top 25 cm of the surface layer of the earth and the construction materials of the buildings. The buildings will reduce the exposure from the surface layer but may themselves be constructed from radioactive material that may add to the radiation exposure more than the shielding reduces it. The soil activity concentrations of China and the United States (UNSCEAR 1993) and the associated dose rate in air are given in table 7. There is a broad range of dose rates. The activity concentration and the associated dose rates for various building materials have been compiled by UNSCEAR (1993) and are given in table 8 dependent on the fraction of the materials in the specific building. Conversion of air kerma (assumed to be numerically equal to dose under equilibrium conditions) to effective dose depends on the geometry of the individual and values are given for adults, children, and infants in table 9.

Results from national surveys representing 60 percent of the world population of outdoor dose rates have been complied by UNSCEAR (1993). National average outdoor dose rates vary from 24 nGy/h for Canada to 120 nGy/h for Nambia. The population average is 57nGy/h. Many of the surveys included indoor and outdoor dose rates, which depends on construction materials used. The average indoor to outdoor dose rate ratio was 1.44 and varied from 0.80 (United States) to 2.02 (Netherlands). There are areas of exceptionally high dose rates associated with Th-232 and U-238 heavy minerals. Two such sites are Kerala, India with 200-4000 nGy/h (Sunta 1993) and the coast of Espirto Santo, Brazil with 100-4000 nGy/h (Pfeiffer et al. 1981). Unusually high dose rates have been reported in Kenya (12000 nGy/h, Paul et al. as reported in UNSCEAR 1993) and Ramsar, Iran (up to 30000 nGy/h, Schrabi as reported by UNSCEAR 1993). These radiation exposures decline with distance above the surface due to absorption by atmospheric constituents with an absorption length on the order of 300 m.

Extraterrestrial Atmospheric Radiation Sources

The ionization in the upper atmosphere results in part from the extraterrestrial particles incident on the top of the atmosphere. These particles are of two sources. A continuous stream of particles come from deep within the galaxy while a more intense but transient source is from our own sun.

Galactic cosmic rays. Cosmic rays originating in the galaxy by processes not entirely understood (Hall et al. 1996) upon entering the solar system interact with the outward propagating solar wind in which is embedded the solar magnetic field. A solution of the Fokker-Planck equation was found by Parker (1965) in which the inward diffusion of galactic cosmic rays is balanced by the outward convection by the solar wind. The density of cosmic ions within the solar system assuming spherical symmetry is then related to the external density as

$$\mu(r,R) = \mu_0(R)\ exp\ [\ -\ \int_r V(r')\ dr'/\ D(r',R)] \qquad (1)$$

where $\mu(r,R)$ is the ion density at radial distance r and rigidity R (particle momentum per unit charge), $\mu_0(R)$ is the density in interstellar space, $V(r)$ is the solar wind speed, and $D(r,R)$ is the diffusion coefficient (Balasubramanyan et al. 1967). The wind velocity and diffusion coefficient depend on the solar activity usually measured by the number of sunspots seen in the solar surface and there is a phase shift between sunspot number and modulation as the wind generated at the solar surface diffuses into the modulation cavity which extends far out into the solar system. The relation of sunspot number to the cosmic ray induced neutron monitor count rate in Deep River, Canada is shown in figure 3 during some of the more recent solar activity cycles. The inverse relation of solar activity and cosmic ray intensity is clearly seen in the figure. A simplified version of the diffusion model was implemented by Badhwar et al. (1994) in which the solar wind is held constant at 400 km/s and the diffusion coefficient is taken as a function of time and is correlated with the Mt. Washington neutron monitor count rate. The diffusion was found to be bimodal with unique dependence on the orientation of the solar magnetic dipole. Assuming an isotropic diffusion coefficient in which the diffusion coefficient generally increases with radial distance as $D(r,R) = D_0(R)\ r^s$ where s is on the order of 0 to 2. The above assumptions lead to

$$\mu(r,R) = \mu_0(R)\ exp\ \{ - V_0\ (r_0^{1-s}\ - r^{1-s})/[(1-s)D_0(R)]\} \qquad (2)$$

where V_0 ,r_0, and $D_0(R)$ are the wind speed, size of the modulation cavity (50 to 100 AU), and diffusion coefficient at 1 AU respectively. Equation (2) is used to scale the modulated flux at 1 AU to arbitrary distance. Modulation studies using various Pioneer, Voyager, and IMP spacecraft show variability of s with solar cycle for some restricted energy ranges but the gross behavior for all energies above 70 MeV is well represented by s = 0.5 (Fujii and McDonald 1997).

The GCR differential energy flux from the diffusion model is compared with measurements made in the near earth environment in figure 4 near minimum solar activity. The most prominent particles are in a broad energy range between 100 and 1,000 MeV per nucleon. These are very penetrating radiations able to penetrate deep into the atmosphere although only the most energetic particles produce effects at ground levels. The flux near solar

minimum or maximum depends on the degree of solar activity during the specific cycle as seen in the Deep River neutron monitor data. The "worst-case" observed flux is shown in figure 5 for which all other recent solar minima and maxima are expected to fall below the respective curves in the figure. A peculiarity of the GCR is the significant number of multiple charged ions as displayed in figure 6. The means by which they interact with the atmosphere and shield materials is still under active investigation as are the biological risk to such radiations (Schimmerling et al. 1998, Wilson 2000, Cucinotta et al. 2001).

Solar sources. Solar cosmic rays or solar particle events (SPEs) were first observed as sudden short-term increases in the ground level ionization rate (figure 1). The close correlation with solar flare events first identified them as originating in the solar surface plasma with eventual release into the solar system (Meyer et al. 1956). Thus it was assumed that the observation of solar surface phenomena would allow forecasting the possibility of such events (FAA 1975). Modern opinion considers the particle acceleration region not to be on the sun at all. Rather large coronal mass ejections from active regions of the solar surface propagate into the interplanetary environment carrying along with them the local solar surface magnetic field frozen into the ejected mass that is a good electrical conductor. There is a transition (shock) region between the normal sectored magnetic field structure of interplanetary space and the fields frozen into the ejected mass which forms a transition region (shock) in which the interplanetary gas is accelerated forming the solar particle event. The escape of the particles from the acceleration region is diffusion limited so that a maximum intensity is implied (Reames 1999). However, when the acceleration region passes the observation point the intensity is observed to increase by an order of magnitude to high levels in so-called shock events and no upper limit in intensity is known within the shock region. The SPE energies obtained in the acceleration process are related to the plasma density and velocity of propagation of the ejected mass. To understand the SPE is then to understand the release of coronal mass and its propagation into interplanetary space relative to the observation point.

The only solar particle events of interest to aircraft are those capable of ground level observations with ion chambers (figure 1) or neutron monitors. The rate of occurrence of such events (Shea and Smart 1993) is shown in figure 7. The ground level events vary greatly in intensity and only the most intense events are important to high-altitude aircraft protection. The largest ground level event yet observed occurred on Feb. 23, 1956 in which neutron monitor count rates rose to 3,600 percent above background levels (figure 8). No other events of this scale have been observed in over fifty years. The next largest ground level event (370 percent over background) was that of September 29, 1989 shown in figure 9 in comparison with a second series of events starting October 19, 1989. A list of particle intensities of the larger events is shown in table 10. The low-energy intensities for dates before November 1960 are most uncertain. The November 1960 event was probed by a series of sounding rockets using nuclear emulsion. SPE data of the 70's and 80's are supported by satellite measurements using active detectors and are most reliable.

It was found by Nymmik (1997) that the particle spectra tend to display a similar dependence above 30 MeV. From the model of Nymmik, the event-integrated proton fluence of the September 29, 1989 event above 30 MeV is given by

$$\int_{30}^{\infty} \phi(E)dE = 1.39 \times 10^9 \text{ protons/cm}^2 \tag{3}$$

where E is the kinetic energy and $\phi(E)$ is the differential fluence in protons/(cm^2-MeV). In this model, $\phi(E)$ is given as a power law above 30 MeV by

$$\phi(E)dE = \frac{C}{\beta} \times \left(\frac{P(E)}{P_{30}} \right)^{-4.5} dE \tag{4}$$

where, β is the proton speed relative to the speed of light, $p(E)$ is the momentum, p_{30} = 239.15 MeV/c is the momentum corresponding to a proton energy of 30 MeV. The coefficient C is given by

$$C = \frac{1.39 \times 10^9}{\int_{30}^{\infty} \left(\frac{239.15}{p(E)} \right)^{4.5} \frac{1}{\beta} dE} = 2.034 \times 10^7 \tag{5}$$

The differential fluence in protons/(cm^2-MeV) below 30 MeV is calculated by using an exponential distribution (Shea and Smart 1990), since there is a flattening of the spectra below that energy based upon observations of this event (Cleghorn and Badhwar 1997). This addition gives a very good empirical description of data below 30 MeV and the event-integrated fluence for protons of the entire measured energy range is well described as illustrated in figure 10.

Geomagnetic Effects. Charged particles arriving at some location within the geomagnetosphere are deflected by the Lorentz force $e\boldsymbol{v} \times \boldsymbol{B}$ which prevents penetration for some directions of incidence and some energies. Such phenomena were extensively studied by Störmer (1930) for a dipole magnetic field which provides the basis for classifying the orbital trajectories of charged particles arriving at some location within the field. As a part of Störmer's theory, allowed trajectories with no connection to asymptotic trajectories exist; these are now recognized as trapping regions associated with Van Allen radiation.

The geomagnetic field can be reasonably approximated by a tilted dipole with moment $M = r_e^3 31\,500$ nT displaced from the Earth's center by 430 km or $0.068r_e$, where r_e = 6378 km. The tilt angle is 11.7° at 69° W longitude. The magnetic quadrupole contributions are then about 10 percent at the surface and decrease to 5 percent at $2r_e$. Higher order moments are even smaller. The motion of charged particles in the geomagnetic field was studied extensively by Störmer. We outline his methods herein. In spherical coordinates, Störmer showed that the azimuth angle ϕ is an ignorable coordinate possessing an integral for the particle's trajectories such that

$$\cos\ \omega = \frac{\gamma}{m\upsilon r} - \left(\frac{ZeM}{m\upsilon r} \right) \frac{\sin\theta}{r^2} \tag{6}$$

where m is the mass of the particle, Ze is the charge, υ is the speed, c is the speed of light, r is radial distance from the center of the field, θ is magnetic colatitude, γ is an integration constant, and ω is the angle between the velocity vector and the azimuthal direction. The allowed Störmer regions consist of the space for which

$$|\cos\ \omega| \equiv \left| \frac{\gamma}{m\upsilon r\ \sin\ \theta} - \left(\frac{ZeM}{m\upsilon c} \right) \frac{\sin\theta}{r^2} \right| \leq 1 \tag{7}$$

Further analysis of the condition in equation (7) shows stable trapping regions as well as the Störmer main cone of transmission given for $\gamma = 2m\upsilon(ZeM / m\upsilon c)^{1/2}$. The Störmer main cone is represented (Kuhn, Schwamb, and Payne, 1965) by the solid angle element

$$\Omega = 2\pi(1 + \cos\omega) \tag{8}$$

which contains the allowed directions of arrival for particles of rigidity R (momentum per unit charge) given by

$$R = \frac{M}{c} \frac{\sin^4\theta}{r^2\left[1 + (1 - \sin^3\theta\cos\omega)^{1/2}\right]^2} \tag{9}$$

Henceforth we change variables from the magnetic colatitude θ to the magnetic latitude λ_m and note that Ω varies form 0 to 4π reaching its half-value at $\omega = \pi/2$ including angles up to the vertical direction. The vertical cutoff model is expressed as

$$\Omega \approx 4\pi\, U\left[R - R_C(\lambda_m)\right] \tag{10}$$

where the vertical cutoff rigidity from equation (9) is

$$R_C(\lambda_m) = \frac{M}{4cr^2} \cos^4\ \lambda_m \tag{11}$$

and U(x) is the unit step function.

Not included in the above formalism are those trajectories that are cut off by the shadow cast by the solid Earth. The fraction of the solid angle covered by the shadow of the Earth is estimated with the assumption that the curvature of the local trajectories is large compared with the radius of the Earth (Kuhn, Schwamb, and Payne, 1965). Then the solid angle fraction is

$$\frac{\Omega_{\text{sh}}}{4\pi} = \frac{1}{2}\left[1 + \cos\left(\sin^{-1}\frac{1}{r}\right)\right] \tag{12}$$

The corrected solid angle for the vertical cutoff model is then

$$\Omega = \Omega_{\text{sh}} U\left[R - R_C(\lambda_m)\right] \tag{13}$$

which leaves the local solid angle open to transmission of charged particles of rigidity R at altitude r and geomagnetic latitude λ_m.

During times of intense solar activity, the solar plasma emitted in solar flares and subflares advances outward and arrives at 1 AU from the Sun. If the Earth is locally present, the plasma interacts with the geomagnetic field in which the plasma pressure performs work on the local geomagnetic field. The initial impact produces hydromagnetic waves causing a general increase in geomagnetic intensity. As plasma flow is established, it generates large electric ring currents and a corresponding impressed magnetic storm field. In the initial phase (hydromagnetic wave), the storm field is parallel to the equatorial field after which the storm field reverses in the main phase of the storm caused by ring currents within the magnetopause and opposes the quiet field, causing a net decrease of the field strength. The main phase is followed by slow recovery to the quiet field conditions (Johnson, 1965).

The magnetic storm model used here assumes a uniform magnetic field impressed on the normal quiet field (Kuhn, Schwamb, and Payne, 1965). The storm field strength can be found from the change in the horizontal field component around the geomagnetic equator. We represent this field by H_{st}. Typical values of H_{st} in the main phase range from substorm values -10 nT to severe storms with -500 nT. On rare occasions, for very intense storms, the storm field exceeds -1000 nT.

Magnetic disturbances have been observed for many years, and various classification schemes for such disturbances have been proposed. The planetary magnetic index K_p is based on magnetometer measurements of 12 stations worldwide. The K_p index is related to a derived planetary index a_p and storm field strength by Bartels (Johnson, 1965) given in the table 11.

The vertical cutoff rigidity as given by equation (11) is further modified to approximate the effects of geomagnetic disturbances. It was shown by Kuhn, Schwamb, and Payne (1965) that the appropriate equation is

$$R_C(\lambda_m) = \frac{14.9}{r^2}\cos^4\lambda_m\left[1 + \frac{H_{\mathrm{st}}r^3}{M}\left(\frac{4}{\cos^6\lambda_m} - 1\right)\right] \tag{14}$$

This vertical cutoff replaces equation (11) and applies to storm conditions. Note the cutoff is zero whenever the result of equation (14) is negative. The geomagnetic field is in fact not a simple dipole. The vertical cutoff for the realistic field is shown in figure 11. Numerical solutions to the charged particle equations of motion in a more realistic geomagnetic field model were introduced by McCracken (1962) and further advanced by Shea and Smart (1983). The numerical work of Smart and Shea is indispensable in understanding extraterrestrial radiation in the Earth's atmosphere.

Atmospheric Interactions. The number of galactic cosmic rays incident on the Earth's atmosphere is modified first by the modulating effects of the solar wind and second by the deflections in the Earth's magnetic field as discussed in the prior sections. Upon entering the Earth's atmosphere, they collide through coulomb interaction with the air molecules delivering small amounts of energy to orbital electrons leaving behind an electron-ion pair. The ejected electron has sufficient energy to undergo similar additional ionizing events. The cosmic ions loose a small fraction

of their energy in these molecular collisions and must suffer many collisions before significantly slowing down. On rare occasions the cosmic ion will collide with the nucleus of an air atom in which large energies are exchanged and the ion and the nucleus are dramatically changed by the violence of the event. If the cosmic ion is a simple proton then the outcome of the reaction is limited compared to the more complex ions such as Si or Fe. The proton will under go collisions with constituents of the air atomic nucleus in which the constituents (neutrons, protons, and small nuclear clusters) are directly ejected from the air nucleus. The remnant of the air nucleus is highly disfigured and unstable emitting further air nuclear constituents in a cooling process similar to evaporation of water molecules from a water droplet and final decay through the usual radioactivity channels of gamma, beta, and electron conversion. Even protons and neutrons have unstable excited states that may emerge from the direct knockout process and subsequently decay by emitting mesons. The more complex ions may also lose particles through direct knockout with subsequent cooling adding decay products to the high-energy radiation field. As a result of nuclear reactions with air nuclei the already complex cosmic radiations increases in complexity as the atmosphere is penetrated. Even beyond the description above, the field further grows in complexity as a result of the mesons produced.

Most of the mesons produced are π-mesons or pions. The energy required to produce a pion depends on charge state and is about 135 MeV for neutral pions and 139.6 MeV for charged pions to which kinetic energy must be added. The pions are unstable particles appearing in three charge states (-1, 0, +1) with decay products depending on the charge. The decay process of charged pions is limited to so-called weak interactions as net charge must remain in the final products and the relatively long lifetime is 26 nanoseconds with the following decay scheme

$$\pi^{\pm} \rightarrow \mu^{\pm} + \nu \tag{15}$$

The $\mu^{\pm}$ (muon) decays with a relatively long lifetime of a 2.2 microseconds as

$$\mu^{\pm} \rightarrow e^{\pm} + \nu + \nu \tag{16}$$

where $e^{\pm}$ is a stable positive or negative electron and the neutrino ν are stable massless (or nearly massless) particles (actually there are at least two different neutrino's having opposite spin polarization states). The lifetimes are modified by the relativistic effect of time dilation depending on speed of the decaying particle. The neutrinos, having no charge, interact only weakly passing through the Earth with relative ease. The neutral pion, having no charge, decays quickly ($\approx 10^{-16}$ s) by electromagnetic processes into two very high-energy gamma rays

$$\pi^{0} \rightarrow \gamma + \gamma \tag{17}$$

It is the two gamma rays that add prolifically to the radiation field in a process known as the electromagnetic cascade. This process is initiated by collision of the gamma rays with air atoms (A) producing high-energy electron/positron pairs as

$$\gamma + A \rightarrow e^{+} + e^{-} + A \tag{18}$$

which in turn interact with air atoms to produce additional high-energy gamma rays as bremsstrahlung radiation

$$e^{\pm} + A \rightarrow \gamma + e^{\pm} + A \tag{19}$$

which in turn produce more electron/positron pairs. The positron also undergoes annihilation events

$$e^{+} + A \rightarrow \gamma + \gamma + A^{+} \tag{20}$$

resulting in energetic gamma rays adding to the cascade process and the resulting radiation field. Other mesons are produced in smaller number, as are antiprotons and antineutrons but are less important in human exposures because of their low frequency of occurrence.

The specification of the atmospheric radiation environment requires solution of the appropriate equations describing the above processes. The relevant transport equations are the linear Boltzmann equations for the flux density $\phi_j(\mathbf{x}, \mathbf{\Omega}, E)$ of type j particles given by

$$\mathbf{\Omega} \cdot \nabla\phi_j(\mathbf{x},\mathbf{\Omega},E) = \sum\int \sigma_{jk}(\mathbf{\Omega},\mathbf{\Omega}',E,E')\, \phi_k(\mathbf{x},\mathbf{\Omega}',E')\, d\mathbf{\Omega}'\, dE' - \{1/[v\tau_j(E)] + \sigma_j(E)\}\, \phi_j(\mathbf{x},\mathbf{\Omega},E) \tag{21}$$

where $\sigma_j(E)$ and $\sigma_{jk}(\mathbf{\Omega},\mathbf{\Omega}',E,E')$ are the media macroscopic cross sections, v is the particle speed, and $\tau_j(E)$ is the particle lifetime in the Earth's rest frame. The $\sigma_{jk}(\mathbf{\Omega},\mathbf{\Omega}',E,E')$ represent all those processes by which type k particles moving in direction $\mathbf{\Omega}'$ with energy E' produce a type j particle in direction $\mathbf{\Omega}$ with energy E. Note that there may be several reactions which produce a particular product, and the appropriate cross sections for equation (21) are the inclusive ones. The total cross section σ_j (E) with the medium for each particle type of energy E may be expanded as

$$\sigma_j\,(E) = \sigma_{j,at}\,(E) + \sigma_{j,el}\,(E) + \sigma_{j,r}\,(E) \tag{22}$$

where the first term refers to collision with atomic electrons, the second term is for elastic nuclear scattering, and the third term describes nuclear reactions. The microscopic cross sections and average energy transfer for most particles are ordered as follows:

$$\sigma_{j,at}\,(E) \sim 10^{-16}\ \text{cm}^2 \quad \text{for which } \Delta E_{at} \sim 10^2\ \text{eV} \tag{23}$$

$$\sigma_{j,el}\,(E) \sim 10^{-19}\ \text{cm}^2 \quad \text{for which } \Delta E_{el} \sim 10^6\ \text{eV} \tag{24}$$

$$\sigma_{j,r}\,(E) \sim 10^{-24}\ \text{cm}^2 \quad \text{for which } \Delta E_{r} \sim 10^8\ \text{eV} \tag{25}$$

This ordering allows flexibility in expanding solutions to the Boltzmann equation as a sequence of physical perturbative approximations. It is clear that many atomic collisions ($\sim 10^6$) occur in a centimeter of ordinary matter, whereas $\sim 10^3$ nuclear coulomb elastic collisions occur per centimeter. In contrast, nuclear reactions are separated by a fraction to many centimeters depending on energy and particle type. Special problems arise in the perturbation approach for neutrons for which $\sigma_{j,at}\,(E) \sim 0$, and the nuclear elastic process appears as the first-order perturbation.

As noted in the development of equation (21), the cross sections appearing in the Boltzmann equation are the inclusive ones so that the time-independent fields contain no spatial (or time) correlations. However, space- and time-correlated events are functions of the fields themselves and may be evaluated once the fields are known (Wilson et al. 1991a, Cucinotta et al. 1996). Such correlations are important to the biological injury of living tissues. For example, the correlated release of target fragments in biological systems due to ion or neutron collisions have high probabilities of cell injury with low probability of repair, resulting in potentially large relative biological effectiveness (RBE) and quality factor (Shinn and Wilson 1991). Similarly, the passage of a single ion releases an abundance of low energy electrons from the medium resulting in intense fields of correlated electrons near the ion path. For example, electron tracks are visualized in nuclear emulsion in figure 12. The ions in the figure are cosmic ions of about 400 A MeV resulting in an energy deposit which is laterally spread from the ion path by distances which are large compared to a cell nucleus as seen in the figure (see also Cucinotta et al. 1998).

The solution of equation (21) involves hundreds of multi-dimensional integro-differential equations which are coupled together by thousands of cross terms and must be solved self-consistently subject to boundary conditions ultimately related to the environment at the boundary, the distribution and composition of the atmosphere, and the geometry of the person's body and/or a complex vehicle. In order to implement a solution one must have available the atomic and nuclear cross section data. The development of an atomic/nuclear database is a major task in code development.

The transport coefficients relate to the atomic/molecular and nuclear processes by which the particle fields are modified by the presence of a material medium. As such, basic atomic and nuclear theories as evaluated by critical experiments provide the input to the transport code database. It is through the nuclear processes that the particle fields of different radiation types are transformed from one type to another. The atomic/molecular interactions are the principal means by which the physical insult is delivered to biological systems in producing the chemical precursors to biological change within the cells. The temporal and spatial distributions of such precursors within the cell system govern the rates of diffusive and reactive processes leading to the ultimate biological effects.

The solution to equation (21) can be written in operational form as $\phi = G\ \phi_B$ where ϕ_B is the inbound flux at the boundary, and G is the Green's function which reduces to a unit operator on the boundary. A guiding principle in radiation-protection practice is that if errors are committed in risk estimates, they should be overestimates. The presence of strong scattering terms in equation (21) provides lateral diffusion along a given ray. Such diffusive processes result in leakage near boundaries. If ϕ_Γ is the solution of the Boltzmann equation for a source of particles on the boundary surface Γ, then the solution for the same source on Γ within a region enclosed by Γ_o denoted by $\phi_{\Gamma o}(\Gamma)$ has the property

$$\phi_{\Gamma o}(\Gamma) = \phi_\Gamma + \varepsilon_\Gamma \tag{26}$$

where ε_Γ is positive provided Γ_o completely encloses Γ. The most strongly scattered component is the neutron field, for which an 0.2 percent error results for infinite media in most practical problems (Wilson et al. 1991b). Standard practice in radiation protection replaces Γ as required at some point on the boundary and along a given ray by the corresponding Γ_N evaluated for normal incidence on a semi-infinite slab. The errors in this approximation are second order in the ratio of beam divergence and radius of curvature of the object, rarely exceed a few percent for space radiations as those incident on the top of the atmosphere, and are always conservative. The replacement of Γ by Γ_N as a highly accurate approximation for space radiation applications has the added advantages that Γ_N is the natural quantity for comparison with laboratory simulations and has the following properties: If Γ_N is known at a plane a distance x_o from the boundary (assumed at the origin), then the value of Γ_N at any plane $x \geq x_o$ is

$$G_N(x) = G_N(x - x_o)\, G_N(x_o) \tag{27}$$

Setting $x = x_o + h$, where h is small and of fixed-step size gives rise to the marching procedures such as those in the code HZETRN (Wilson et al. 1991b).

Estimates of the charged particle and nucleonic components (NCRP 1987) as a function of depth in the atmosphere are shown in figure 13. The neutron and pion components show a net increase (buildup) near the top of the atmosphere reaching a maximum at atmospheric depths of 50 to 100 g/cm^2 followed by an exponential decline. Protons show a steady decline in intensity. The decay of the charged mesons into charged muons causes a buildup of the muon component that shows little decline. The reason is that most of the nucleons undergo nuclear reactions, which accounts for their exponential decline while the charged pions are depleted by weak decay. Since most pions are produced near the top of the atmosphere where high-energy nuclear collisions are plentiful, the pions decline at greater depths. The muons from the pion decay are mainly produced in the upper atmosphere and have no nuclear reactions and are therefore little attenuated in reaching the larger depths. Furthermore, their long lifetime is effectively increased by relativistic time dilation, allowing many muons to reach the ground before they decay. The electrons are from the electromagnetic cascade driven by the high-energy gamma ray decay of the neutral pion, which are mainly produced in the upper atmosphere. The electron population declines as they loose energy through bremsstrahlung and atomic collisional processes. The relationship between atmospheric depth and altitude is given in figure 14.

Atmospheric radiations. The ionizing radiation within the earth's atmosphere has been studied by many groups, over many decades, and with various instruments. The observation over many decades with a common instrument allows the study of the time and latitude structure on a consistent basis. Such long-term studies are by necessity immune to modern detector development and their main value is the self-consistency of the resulting database. Two such detectors have played such a role: high-pressure ion chambers (Neher and Pickering 1962, Neher 1961, 1967, 1971, Neher and Anderson 1962) and Geiger-Mueller counters (Bazilevskaya and Svirzhevskaya 1998). A more limited study was made over most of solar cycle 20 (1965 to 1972) using tissue-equivalent ion chambers, nuclear

emulsion, and fast neutron spectrometers (Foelsche et al. 1974). The detectors give complementary information, the ion chamber relates directly to exposure (rate of ion formation in standard air), the Geiger-Mueller tube counts number of particles (insensitive to neutral particles), and the neutron spectrometer provides new data not available in the other two packages. The high-pressure ion chamber measures the ion current generated by the cosmic rays in the filling gas. The filling gas is usually argon within a steel walled chamber to maintain electron equilibrium at the gas/wall interface. It is relatively more sensitive to gamma radiation than the air molecules but the charged particles can be more directly related to air exposure rates. It is insensitive to neutrons. The Geiger-Mueller tube is nearly 100 percent efficient in counting charged particles and rather inefficient in counting uncharged particles such as gamma rays and neutrons. Only the neutron spectrometer allows clear identification of neutrons and their spectral properties.

The Geiger-Mueller counter has the advantage of being lightweight and compact allowing radiosound balloon studies that are relatively inexpensive as is necessary for long-term support. A remarkably detailed database on many of the small temporal details was obtained over the years of 1957 to 1997 in the studies of Bazilevskaya and Svirzhevskaya (1998). The cosmic ray flux is shown in figure 15 for low solar activity (February 1987) and high solar activity (September 1989) at two locations with differing geomagnetic cutoffs (R_c = 0.6 GV at Murmansk and R_c = 6.7 GV at Alma-Ata). The count rate increases with atmospheric depth as the multitude of secondary charged particles are added with deeper penetration into the atmosphere. The secondary particle generation process depends on the energy of the initiating cosmic particles at the top of the atmosphere; low energies are less deeply penetrating, with greater penetration depths at higher energies. The high latitude data (R_c = 0.6 GV) in figure 15 shows only a net modest increase in count rate with depth at the top of the atmosphere near solar minimum since the number of low energy particles present at the top of the atmosphere tend to dominate the GCR spectrum (see figure 5) at this time in the solar cycle. As solar maximum is approached, the low energy particles can no longer penetrate the solar modulation cavity (figure 5) and the resulting maximum atmospheric count rate moves deeper into the atmosphere as seen in figure 15. Note also the percent increase in the count rate is likewise much higher near solar maximum as one would expect. The low energy cosmic particles present at the top of the atmosphere are likewise removed by the geomagnetic field at lower latitudes as seen by comparing the Murmansk curves (triangles) with those measured at the lower latitudes at Alma-Ata (circles). Note that the count rates near the surface (~1,000 g/cm^2) are nearly independent of solar modulation and geomagnetic cutoff. This results from the fact that only the highest energies primary particles contribute significantly to the ground level radiation and are little affected by either factor (for example, see figure 5 for solar modulation effects).

Balloon flights during solar particle events (SPE) were likewise made by Bazilevskaya and Svirzhevskaya in which large perturbations in the atmospheric radiation was observed (figure 16). In this case, the observed particles are mainly protons since SPE are relatively low in energy for which meson production with their associated electromagnetic cascades is limited. The proton mean free path to nuclear absorption is on the order of several tens of g/cm^2 so that relatively few of the protons beyond 100 g/cm^2 depths are primary particles. There is a nucleonic cascade in which high-energy neutrons are in part responsible for carrying the radiation deep into the atmosphere

where they are converted into protons in nuclear reactions. The observations depicted in figure 16 show that the SPE can easily dominate the radiation fields at aircraft altitudes even when the ground level fields are only slightly affected as seen for the October 1989 event (compare figure 16 with figure 9). We anticipate that the much larger ground level events will have correspondingly large disturbances in aircraft radiations as will be addressed subsequently in this paper.

Observations were also made during large geomagnetic storms. In this case, the perturbations of the geomagnetic field during the storm main phase compresses the geomagnetic field increasing the loss of trapped electrons by increasing the rate of collision with the earth's atmosphere. It is those trapped particles that populate the trapped belts near the poles seen in figure 2 that are mainly lost to the atmosphere. These electrons were observed on May 1994 at high altitudes as seen in figure 17. As estimated by Foelsche et al. (1974), these particles pose no hazard to high altitude aircraft as can be judged by the results in the figure 17.

Although not a naturally occurring event, many of the balloon flights were made during the period of atmospheric nuclear testing. Measurements made in 1970 are shown in figure 18 in which high altitude radioactive pollution is clearly observed. The particles observed here are mainly gamma rays. The main concerns for these types of radiations is for aircraft surface contamination and intake into the cabin air circulation system (FAA 1975) followed by inhalation.

The Geiger-Mueller count rate is not sufficient to relate to human risks. Additional information on linear energy transfer (LET) is required as shown in figure 19 (Tobias 1952). In addition to the count rate is shown the average rate of energy loss that is nearly proportional to the average specific ionization. As the composition of the radiation changes through interaction with atmospheric constituents the energy loss rate of the radiation field is modified having important implications on radiation risks. Evaluation of risks requires specific knowledge of the particles and their corresponding energies present at the exposure.

Starting at the top of the atmosphere, a significant feature of GCR exposures is the presence of heavy ions which are potentially very damaging. A comparison of the solution of equation (21) with measurements of Webber and Ormes (1967) is shown in figure 20. The more massive ions attenuate more quickly in the atmosphere due to their larger nuclear cross sections. They fragment into smaller ions and neutrons producing mesons in the process. The fragmentation of the iron ions results in 120 different isotopes that need to be accounted (Kim et al. 1994). The data in the figure groups the isotopes by charge number to improve the statistics of the experiment. The fragmentation of the heavier ions result in contributions to the lightest ion group (Li, Be, B) which hardly changes at all over to relatively large penetration depths. Clearly, the composition of the GCR is undergoing large changes in the upper atmosphere. The penetrating component of the heavy ions poses some issues at high altitude commercial operations as one hit per gram tissue each month is anticipated for the crew in supersonic transport operations (Allkofer and Heinrich 1974).

It was generally regarded that although neutrons played an important role in understanding the trapped radiations and for the formation of many cosmogenic isotopes in the atmosphere, the role of neutrons in direct human exposure was believed to be very limited (ICRP 1966) and estimates of dose equivalent was largely taken as the air exposure (Wallace and Sondhaus 1978). However, when humans entered the space program the concern for space radiation led to the development of computational shield models that uncovered the important role of neutrons as secondary radiations. When the supersonic transport was first proposed, Foelsche proposed a number of concerns relating to neutrons as a potentially important component in atmospheric radiation (Foelsche 1961, Foelsche and Graul 1962). As a result a study of atmospheric radiations was made over most of solar cycle 20 in which neutrons and other biologically important components were the focus. The study consisted of over 300 airplane flights using the General Dynamics/Martin RB-57F, Lockheed U-2, and Boeing 707 aircraft and 25 high-altitude balloon flights as indicated in figure 21. The intent was to gain information on GCR background levels and attempt to make measurements during a SPE. A more detailed description is given by Foelsche et al. (1974) and Korff et al. (1979). The acquired data set was used to derive a parametric atmospheric ionizing radiation model (Wilson et al. 1991b).

Figure 22 shows measurements by the neutron spectrometer and tissue-equivalent ion chamber made on a high-altitude balloon flight near solar minimum (maximum GCR intensity) over Ft. Churchill, Canada (Rc = 0.2 GV). The instruments were only lightly shielded (less than 1 g/cm^2 fiberglass and foam). The features to be noted are the broad maximum in the neutron flux, with peak at 60 to 70 millibars (mbar) and a leveling off of the ion chamber dose rate above 50 mbar (1 mbar $\approx$ 1 g/cm^2). Also shown is the parametric environmental model (Wilson et al. 1991b). A second flight one month later above St. Paul, Minnesota (Rc = 1.3 GV) is shown in figure 23. The lower energies of cosmic rays are removed by deflection in the geomagnetic field which reduces the ion chamber dose rate considerably above 100 mbar and leaves the neutrons, produced mainly by higher energy cosmic rays, little affected. This conclusion applies only above the latitude knee and at high altitudes where low energy particles mainly contribute to the radiation field near solar minimum. As solar maximum is approached, the low energy particles are eliminated by the solar modulation and this effect is reduced as noted below. At lower altitudes and latitudes both ionization and neutron components result from high energy particles and the variations of ionization and the neutron fields are comparable (Hewitt et al. 1980, Goldhagen et al. these proceedings). A third flight about a week later over St. Paul shown in figure 24 includes the effects of a 15 cm thick tissue equivalent spherical phantom on the measurements in which the neutrons are dramatically reduced with little affect on the ion chamber dose rate. A reflight from Fort Churchill two years after solar minimum in figure 25 in which the neutron flux and ion chamber dose rate have decreased by about the same percentage. Also shown in the figure are the resulting model developed from the project (solid curve) and results of Monte Carlo calculations for the same time period (dashed curve). The Monte Carlo evaluated neutron spectra were used to estimate those neutrons not seen by the spectrometer as shown in figure 26. The conversion into dose and dose equivalent are shown in the figure. As can be seen, over half of the neutron dose and nearly half of the dose equivalent are from neutrons above 10 MeV. The contributions to dose equivalent from charged particle ionization, neutrons, and charged particle nuclear events in tissue are shown in figure 27. The data in the figure is for high latitudes and various times in the solar cycle. The

conversion to dose equivalent used the older quality factors which limit to 20 at 100 keV/micron and do not decrease at higher values of LET.

There is a lower level short-term structure in the atmospheric radiation levels, shown in figure 28, which has two sources. The diurnal variation is due to the relative tilt of the geomagnetic dipole to the solar wind direction during daily rotation. The amplitude depends on the temporal intensity of the local solar wind. The longer sidereal variation is related to solar rotation as the emitted coronal plasma depends on local features in the solar surface at the time of emission. The solar wind expands as an archimedean spiral that co-rotates with the solar surface (similar to a rotating water sprinkler) and long lived surface features will show a 28-day recurrence in the local cosmic ray intensities accounting for the longer-period structure in the figure. Such time variations, up to a few percent, should be taken into account in interpreting measured data such as that shown in figure 29. Figure 29 shows the model results for ionization in air and a flight measurement of relative values of ionization rate using a high-pressure ion chamber on an ER-2 aircraft on June 13, 1997. The model results in figure 29 do not yet include the short-term variations.

Background exposure levels. The data set obtained by Foelsche et al. had sufficient coverage that a parametric model by interpolation over geomagnetic cutoff, Deep River neutron monitor count rate, and altitude allowed a global model of atmospheric radiations for all times to be made. For example, the modeled 1 to 10 MeV neutron flux is shown in figure 30 in comparison to the flight data. The atmospheric ionization data was obtained from Neher (1961,1967, 1971) and Neher and Anderson (1962) as compiled by S. B. Curtis (Boeing 1969) in table 12 for solar minimum and table 13 for solar maximum and utilized by Wallace and Sondhaus (1978). The tissue equivalent ion chamber is taken as the conversion of air exposure rate to dose rate in tissue from all but the neutron dose rate which is related to the 1-10 MeV flux (figure 30) assuming the Monte Carlo extension of the neutron spectrum (figure 26). Added to this is a parametric representation of the nuclear stars in tissue estimated by the nuclear emulsion data after subtraction of the neutron-induced stars. The resulting dose equivalent per 1000 hours of operations (the maximum number of flight hours for crew members which does not include the "dead head times") is shown at solar minimum in figure 31. One can see that there is a high plateau in the Polar Regions where dose equivalent rates are maximum for any given altitude with a broad deep valley in equatorial regions. These are effects due to the geomagnetic field on the incident primary cosmic particles. The height of the polar plateau relative to the equatorial valley increases at the higher altitudes. The concentration of iso-dose equivalent contours in the intermediate latitudes is referred to as the knee of the latitude dependence. The irregularity of the contours relative to geographic coordinates is due to the tilt of the dipole field and presence of the quadrupole moments of the geomagnetic field. The north Atlantic flight corridor is one of the busiest in the world and is among the most highly exposed routes in aircraft operations. Much of European flight is near or below the latitude knee and somewhat lower exposures are expected. In distinction, flights over Canada are among the most exposed. The maximum solar modulation in solar cycle 20 is shown in figure 32. As expected, the effects of modulation show strong latitude and altitude dependence. Mainly those regions affected by the lower-energy particles show significant modulation effects.

Although most studies of atmospheric radiation are the result of concern for airline crew exposures, most individuals are exposed as a result of the ordinary circumstances of life (where they live and work). The populations of the world are located in large part on the coastal plains of the greater landmass. As a result, several studies of cosmic ray exposures from sea level to a few thousand meters have been made. Measurements of the associated environment require some care since the terrestrial radionuclide emissions are a confusing factor requiring some care in evaluation since the terrestrial radiations depend on local geological factors. In addition, even the cosmic radiations change character at ground level since interaction with the local terrain modifies the neutron fields above the surface. One can see from figure 13 that the near sea level environment is mainly composed of muons with smaller number of photons (not shown), electrons and neutrons which are produced high in the atmosphere by high-energy cosmic rays. As a consequence, the sea level ionization rate in a high-pressure ion chamber is closely related to both the absorbed dose and dose equivalent as the muons, photons, and electrons are minimum ionizing radiation (quality factor is unity) and the neutron absorbed dose is small. The difficulty in use of the ion chamber to study cosmic radiation near the surface is the confusion from the terrestrial radiation contributions that can be relatively large on the surface and decline with increasing altitude from the surface. From the earliest measurements of Wulf and Hess it was known that the atmospheric ionization rates declined with altitude followed by an increase at higher altitudes until the ground levels are achieved again at about 1,500 m.

The sea level cosmic ray ionization rate at middle to high latitudes was reviewed and consistently found to be in the range of 1.9 to 2.6 ion pairs/cm^3-s and the value of 2.1 ion pairs/cm^3-s has been consistently adopted since that evaluation (UNSCEAR 1982). Note that this is significantly lower than the value given by Wallace and Sondhaus in tables 12 and 13. Assuming the average energy for the formation of an ion pair in moist air is 33.7 eV, the absorbed dose rate corresponding to 2.1 ion pairs/cm^3-s is 32 nGy/h. Measurements near 15^o geomagnetic north in Taiwan by Weng and Chen (1987) on Mount Ali and by aircraft are shown in figure 33. The offset in dose rates on Mount Ali seen in the figure results from the terrestrial radionuclide emissions from the moutain. Extrapolation of the aircraft data to 100 m gives 34.5 nGy/h. Additional measurements over two deep water reservoirs and over South Bay yielded 31±6 nGy/h. Subtracting contributions of radionuclides in the air and water yields the cosmic ray contribution to be 26±7 nGy/h accounting for both uncertainty in Rn contributions in air and in the measurements. The value adopted by UNSCEAR (1982) is in the range of uncertainty of the Taiwanese measurements although lower values are indicated for the lower latitudes. Similar values were measured at Hong Kong (27-31 nGy/h at 6.5^o geomagnetic north) by Tsui et al. (1991) and Shenzen, China (28 nGy/h near 6.5^o geomagnetic north) by Yue and Jin (1987) indicating the ionization rates are lower by about 10-15 percent near the geomagnetic equator. The absorbed dose at high and low latitudes is given by Hewitt et al. (1980) shown in figure 34.

The neutron flux at sea level is estimated (Hajnal et al. 1971) at 50 degree geomagnetic North to be 0.008 neutrons/cm^2-s. The energy spectrum is very broad and difficult to measure so that dose equivalent estimates are still uncertain (Hajnal and Wilson 1991). Average effective dose equivalent was taken as 2.4 nSv/h by UNSCEAR (1988). With the changing quality factor (ICRP 1991) the dose equivalent is estimated to increase by about 50

percent (Wilson and Townsend 1988, Hughes 1993) for which UNSCEAR (1993) adopted the value of 3.6 nSv/h. The latitude dependence was further studied by Nakamura et al. (1987) using He-3 counters in a multi-sphere arrangement (six polyethylene spheres ranging from 5.1 cm to 45.2 cm) with results shown in figure 35 (older quality factors). Changes in quality factors would require increasing these results by about 50 percent. The altitude dependence over Japan was further studied using a high efficiency dose equivalent counter which was cross calibrated with the multi-sphere spectrometer as shown in figure 36. Again these results should be increased by about 50 percent for the changing quality factors.

The dose equivalent rate has been represented by the following functions. The direct ionization contribution is approximated as

$$H_I(z) = H_I(0)\,[0.205\,\exp(-1.649\,z) + 0.795\,\exp(0.4528\,z)] \tag{28}$$

where z is in km and $H_I(0)$ is 32 nSv/h. The corresponding neutron dose equivalent is approximated (Bouville and Lowder 1988) by

$$H_N(z) = H_N(0)\,\exp(1.04\,z) \tag{29}$$

for $z < 2$ km and

$$H_N(z) = H_N(0)\,[1.98\,\exp(0.698\,z)] \tag{30}$$

for $z > 2$ km where $H_N(0)$ is 3.6 nSv/h. The results are shown in figure 37. The neutron dose equivalent is small for altitudes less than 3 km and increases rapidly to be half of the total dose equivalent near 6 km.

Atmospheric SPE. It was clear from the observations in figure 16 that even a rather modest ground level SPE such as that which occurred in October 1989 could dominate the particle flux at aircraft altitudes, but their importance to human exposure needs to be explored. This requires measurements with instrumentation capable of distinguishing the biologically important components, such as that of Foelsche et al. (1974). Two such flights were achieved on March 30-31, 1969. The event was very modest as a ground level event but provides important information on exposures to high altitude aircraft (see figure 38). Assuming Nymmik's approximation is correct (see equation 4) then the high-energy fluence important to aircraft exposure would be nearly proportional to the ground level response. This relationship has been assumed to estimate the dose equivalent rate of other larger ground level events as indicated in the figure. An independent assessment using the estimated spectral flux of the February 23, 1956 event is shown in figure 39 and is in reasonable agreement with the estimate obtained from projecting the flight data.

The global distributions of dose equivalent rate during the February 23, 1956 event are shown in figure 40 at selected altitudes using the methods of Wilson et al. (1970). Again one sees a radiation plateau in the polar region and a broad valley at lower latitudes. Of particular note are the high rates over the north Atlantic as was the case for the background levels only the knee is sharper and at higher latitudes. The altitude dependence of the dose equivalent rate in the extreme north section of the usual US-to-Europe flight lanes is shown in figure 41. The accumulated dose equivalent on a flight during this event can be quite high even at subsonic altitudes. One should

keep in mind that this is the only event of this magnitude observed in over fifty years of observation and so is extremely rare. The next larger event is the September 29, 1989 event in which dose equivalent rates were an order of magnitude lower. The events of the magnitude of the September 29, 1989 are in fact rare with only one such event per decade on the average.

Cosmogenic radionuclides. Cosmogenic radionuclides are produced in the many nuclear reactions with the air atomic nuclei and to a lesser extent with the ground materials. The dominant isotopes are produced in reactions with the oxygen and nitrogen atoms and to a lesser extent with other trace gases as argon and carbon dioxide. Their importance in human exposure depends on the production rate, radionuclide lifetime, the chemical/physical processes of the atmosphere/terrain, and the body processing following ingestion and/or inhalation. There are only four such isotopes of importance to human exposure as given in table 14. The carbon-14 is mainly produced by neutron (n,p) events in nitrogen-14. The hydrogen-3 and berylium-7 are produced in high-energy interactions with nitrogen and oxygen nuclei. The sodium-22 is produced in high-energy interactions with argon. All of these radionuclides are mainly produced in the atmosphere in which residence times can be 1 year in the stratosphere before mixing with the troposphere. Residence times in the troposphere are only 30 days for nongaseous products. Carbon-14 undergoes oxidation soon after production to form carbon-14 dioxide. Not all of these radionuclides are accessible to human exposure. For example, about 90 percent of the carbon-14 is dissolved into deep ocean reservoirs or resides as ocean sediment with the remainder on the land surface (4 percent), in the upper mixed layers of the ocean (2.2 percent) and in the troposphere (1.6 percent). Carbon-14 enters the biosphere mainly through photosynthesis. Hydrogen-3 oxidizes and precipitates as rain water. The berylium-7 concentrations are unevenly distributed over the earth's surface being strongly effected by global precipitation patterns (NCRP 1987). The bioprocessing of sodium-22 is affected by the overlying canopy cover which serves as a filter to ground vegetation (Jenkins et al. 1972) and shows large variation in tissues of elk, deer, and caribou (Jenkins et al. 1972).

External exposures. Although most studies of atmospheric radiation have been the result of concern for airline crew exposures, most individuals are exposed as a result of the ordinary circumstances of life. Knowing the local galactic cosmic ray environment is the beginning of the problem but the effects of shielding of building structures and the human body are further modifying factors. It is usually assumed that the effective dose equivalent from the directly ionizing component is the same as the dose equivalent (28 to 32 nGy/h from equator to high latitudes). One must account then for modifications for building structures and occupancy factors. Indoor measurements in a 12-storey building showed a steady decline in cosmic ray exposures from the roof to the basement as shown in table 15. Additional studies by various groups are shown in table 16. The effective shielding factors vary by 30 percent depending on where the measurement is made within the building as shown by Fujitaka and Abe (1984a). Fujitaka and Abe (1984b) also show that the dose rate does not depend on the details of the building interior. However, the location of other buildings can have an effect on exposures on the lower floors but all such parameters will have only a 30 percent effect on the exposure. The single most important parameter is the floor material and structure (Fujitaka and Abe 1986). The neutron transmission factors are usually taken as unity (UNSCEAR 1988, 1993). The neutron spectrum must be better understood to improve on this estimate.

The distribution of effective dose equivalent was modeled by Bouville and Lowder (1988) and used to estimate the world population exposures based on terrain heights and population distributions. The annual effective dose equivalent was estimated from equations (28) to (30) in UNSCEAR (1988) with slightly different values of $H_I(0)$ and assuming a building shielding factor of 0.8 and an occupancy factor of 0.8. The distribution of collective dose in each altitude interval is shown in figure 42. About one half of the effective dose equivalent is received by people living at altitudes below 0.5 km and about 10 percent of those exposed are above 3 km. Thus, 90 percent of all exposures have less than 25 percent of the dose equivalent being contributed by neutrons (see figure 37). A small fraction of people living at high altitudes receive exposures for which 40 to 50 percent of the exposure is from neutrons. Some countries like the United States have large coastal regions where the population effective dose is near that at sea level. Other countries with large cities on elevated plateaux such as Mexico, Kenya, Ethiopia, and Islamic Republic of Iran have relatively high exposures (see table 17). For example, the cities of Bogata, Lhasa, and Quito receive annual effective dose equivalents from cosmic radiation in excess of 1 mSv (UNSCEAR 1988) of which 40 to 50 percent are from neutrons.

Passenger and crewmembers of commercial aircraft experience even higher dose equivalent rates of which 60 percent are from neutrons. The exposures are dependent on altitude, latitude, and time in the solar cycle. Most operating aircraft have optimum operating altitudes of 13 km but the many short flights operate at lower altitudes of 7-8 km at speeds of 600 km/h. For longer flights 11-12 km is typical. Estimates of human exposures were made by UNSCEAR (1993), assuming $3 \cdot 10^9$ passenger-hours aloft annually and 2.8 μSv/h at 8 km found 10,000 person Sv as the collective dose equivalent. Worldwide, this is an annual average effective dose of 2 μSv although in North America it is about 10 μSv. In any case, air travel is a small contribution to the annual worldwide average effective dose from cosmic rays of 380 μSv.

A small number of supersonic airplanes operate at cruise altitudes of 15-17 km. The average dose equivalent rate on the six French planes for the two years following July 1987 (from solar minimum through near solar maximum) was 12 μSv/h with monthly values up to 18 μSv/h (UNSCEAR 1993). During 1990 the average for the French planes was 11 μSv/h and the annual dose equivalent to the crew was about 3 mSv (Montagne et al 1993) while 2,000 flights of the British planes had an average of 9 mSv/h with a maximum of 44 mSv/h (Davies 1993). All of the dose equivalent estimates of the Concorde use older values of quality factor and revised estimates would be about 30 percent higher. The exposures to passengers on supersonic aircraft would be about the same as for the equivalent subsonic flight wherein the higher rate of exposure is nearly matched by the shorter supersonic flight time. Crew exposures can be substantially higher since time at altitude is about the same independent of speed. There is only a negligible contribution to the collective dose since the supersonic traveler and crew represent a small fraction of the airline industry.

Internal exposures. Cosmic rays produce a number of radionuclides of which the four most important are given in Table 14. The most significant exposures are for Carbon-14. The assessment of the exposures was made by UNSCEAR (1977) from the known specific activity of Carbon-14 of 230 Bq per kg of carbon leading to an annual effective dose of 12 μSv. The next most abundant of the radionuclides of Hydrogen-3, Berylium-7, and Sodium-22 in table 14 are totally negligible (UNSCEAR 1997). A concern for surface contamination by Be-7 for operations in the stratosphere has not yet been answered.

Neutron Exposure Issues

It is useful to understand exposures in aircraft in relation to other exposures. This is especially true in terms of neutron exposures for which the corresponding neutron exposure risk coefficients are uncertain. The main exposures to neutrons are either occupationally related and/or from the result of cosmic rays. Estimates of occupational neutron exposures within the US were given by the NCRP (1987) for the year 1980. These estimates are based on data gathered in the years 1977 to 1984 and are given in table 18. Studies by the Environmental Protection Agency indicate that such exposures had decreased by a factor of two in the years 1970 to 1980 due to improvement in protection practice (Klement et al. 1972, EPA 1984). Not included in the table are crew members of aircraft.

The cosmic ray dose equivalent rates were discussed in an earlier section. In that section the rates were evaluated on the basis of measurements made with various instruments. The ratio of the neutron dose equivalent rate to the total dose equivalent rate according to the parametric atmospheric radiation model is shown in figure 43. It is clear from the figure that 40 to 65 percent of the dose equivalent at ordinary aircraft altitudes are due to neutron exposures depending on latitude and longitude of the flight trajectory. The fraction of neutron exposure is altitude dependent but varies little over most aircraft operating altitudes. Since most commercial flights take place at relatively high latitudes, one can assume that about 60 percent of the dose equivalent is from neutrons in commercial airline operations.

Although a consistent data set over most of the geomagnetic latitudes and altitudes during most of solar cycle 20 has been measured, many of the individual components were not resolved due to instrument limitations at the time of measurement and the major portion of the neutron spectrum depends on theoretical calculations for proton interactions with the atmosphere (see figure 26). Prior measurements of the atmospheric neutron spectrum are shown in figure 44. Hess et al. (1959) estimated the neutron spectrum using moderated boron trifluoride counters and a bismuth fission chamber supplemented with a model spectrum. Korff et al. (1979) used a liquid scintillator spectrometer sensitive mainly to 1-10 MeV neutrons with analysis assuming a simple power law spectrum (note that the Korff et al. data in the figure is at a higher altitude). Hewitt et al. (1978) measured the neutron spectrum using a Bonner sphere setup at subsonic altitudes and analyzed the data assuming a simplified spectral analysis. The Hewitt et al. result confirms the importance of the high-energy neutrons but left the exact nature of the spectrum uncertain due to limitations of the analysis methods. Nakamura et al. (1987) used a Bonner sphere setup at much lower latitudes and his results are multiplied by 3X for comparison of spectral shape. Ferenc Hajnal of the US Department of Energy Environmental Measurements Laboratory developed new analysis techniques for unfolding

Bonner sphere neutron spectral data and found important structural features in Hewitt's data near 100 MeV (see figure 45) that have important implications for aircraft exposures (Hajnal and Wilson 1991, 1992).

A study of the atmospheric neutron spectrum lead by H. Schraube of GSF in Neuherberg has been funded by the Directorate General XII of the European Union. The experimental component consists of a Bonner sphere spectrometer with a ^{3}He proportional counter (Schraube et al. 1998) on a mountaintop (Zugspitze). The theory part of the study uses the FLUKA code at the University of Siegen and the known cosmic rays incident on the atmosphere (with the multiple charged ions assumed to be dissociated into constituents, Roesler et al. 1998). It is interesting to note that the structure expected from the analysis of Hajnal at 100 MeV (figure 45) appears in both the measurements and the FLUKA calculation (see figure 46). Note that this feature is absent in the results from the LUIN code (also shown in figure 46) which depended on the Hess spectrum for guidance as the LUIN code is not a fundamental calculation in that information outside the LUIN result is used to patch an answer into the final values (O'Brien and Friedberg 1994). The importance of the Schraube et al. study is that the neutron ambient dose equivalent is about a factor of two larger than that estimated using the LUIN code (Schraube et al. 1998) and the added contributions are from high-energy neutron interactions with tissue nuclei resulting in an array of high LET reaction products at each collision event (see figure 47 where LET spectra of a 1 GeV neutron event is compared to a typical alpha decay spectrum). Very little biological data exist on such radiation interactions (Baarli 1993, Wilson et al. 1990, 1995) and the important cancer risk coefficients are very uncertain.

Further studies were started at the NASA Langley Research Center. An instrument package was developed in accordance with the NCRP (1995) recommendations through an international guest investigator collaborative project, thereby ensuring the availability of the numerous instruments required to measure the many components of the radiation spectra. Selection criteria included: (a) the instruments had to fit within the cargo bay areas of the ER-2 airplane and be able to function in that environment, (b) each instrument must have a principal investigator with independent resources to conduct data analysis, and (c) the instrument array must be able to measure all significant radiation components for which the NCRP (1995) had established minimal requirements. Also, the flight package had to be operational and the first flight occur before or near the maximum in the galactic cosmic ray intensity (ca. spring/summer 1997). Flights of the ER-2 package were in June 1997 during the maximum of the galactic cosmic ray intensity (several months after sunspot minimum in September 1996, see figure 3). Preliminary results of these flights will be presented at this workshop.

Estimates of dose equivalent rates are available from a number of sources. Only a few give separate values for neutron contributions. Bagshaw et al. (1996) give average rates for long haul flignts from London to Tokyo as 3 μSv/hr for neutrons and an additional 3 μSv/hr for other components for a total of 6 μSv/hr. Schalch and Scharmann (1993) employed a proton recoil spectrometer to estimate the neutron dose equivalent arriving at 8 μSv/hr for neutrons and 11.5 μSv/hr total on Frankfort/New York routes and 9.5 μSv/hr for neutrons and 11.8 μSv/hr total on Dusseldorf/San Francisco routes. Altitude and latitude dependent results using a high-pressure ion chamber and spherical remmeter are given by Akatov (1993) in table 19. Although the quality of the ionization dose

is not given, it is seen that the neutron dose equivalent rate is on the order of half or more of the exposure. Since these measurements are made at solar minimum where the cosmic ray intensities are maximum, it can be concluded that a discrepancy appears between the Schalch and Scharmann result measured at much lower altitudes during elevated solar activity and the neutron dose equivalent rate given by Akatov at SST altitudes.

In addition to the flight routes used, the commercial aircraft crew exposures depend on the actual number of flight hours, which may be as many as 1,000 hours per year. Hughes and O'Riordan (1993) estimate that long haul crews are airborne 600 h/yr while short haul crews log only 400 h/yr and they used the average value of 500 h/yr. Bagshaw et al. (1996) quote for a mix of ultra long haul and long haul as 600 h/yr while exclusive ultra long haul crews fly up to 900 h/yr. Oksanen (1998) lists annual average cabin crew hour as 673 while the technical crew hours are 578. The range of hours given by Oksanen range from 293 to 906 hours per year. In addition to exposures in actual flight operations, added exposure is due to off duty flights in returning to a home base estimated by some to be twenty percent of the actual flight hours that are logged.

Hughes and O'Riordan (1993) estimate an average annual dose equivalent 3mSv/yr (≈ 1.8 mSv/yr neutron) for UK airlines with 6 mSv/yr (≈ 3.6 mSv/yr neutron) for near polar flights. Montagne et al. (1993) estimate and average for Air France long haul pilots of 2 – 3 mSv/yr (≈ 1.2 – 1.8 mSv/yr neutron). Wilson et al. (estimate during the years 1982 – 1983 that domestic crews in Australia received 1 – 1.8 mSv/yr (≈ 0.6 – 1.1 mSv/yr neutron) while international flights receive 3.8 mSv/yr (2.3 mSv/yr neutron). Preston (1985) gives average dose equivalent rates of 9.2 μSv/hr (≈ 5.5 μSv/hr neutron) in British Airways operations of the Concorde for the year of 1979 with a maximum observed rate of 38.1 μSv/hr (≈ 22 μSv/hr neutron). Observed technical crew exposures were on average 2.8 mSv/yr (1.7 mSv/yr neutron) and 2.2 mSv/yr (≈ 1.3 mSv/yr neutron) for the cabin crew (there are few flight hours for these crews). Similar differences (20 – 30 percent) between flight deck exposures and cabin exposures were observed by Wilson et al. (1994). Even differences between aircraft type (20 percent) were observed.

In estimating the collective dose equivalent we will follow the UNSCEAR (1993) who assumed $3 \bullet 10^9$ passenger-hours in flight during 1985 and an annual average rate of 2.8 μSv/hr (≈ 1.6 μSv/hr neutron) resulting in a collective dose equivalent of 8,400 person-Sv (5,040 person-Sv neutron). By 1997, air travel had grown to $4.3 \bullet 10^9$ passenger-hours in flight leading to a collective dose equivalent of 12,000 person-Sv (7,200 person-Sv neutron). The crew add little to the collective exposure due to their small number. If we assume that the worldwide occupational exposure to neutrons is five times that in the US and consider the exposures in the high cities we can construct the following table 20. The greatest collective dose equivalent of any group is the citizens of the high cities (12,280 person-Sv) with aircrew the largest occupationally exposed group (7,200 person-Sv). The nuclear workers are next largest with 338 person-Sv.

Concluding Remarks

In the present paper, we have given an overview of aircraft exposures and placed it in the context of world population exposures. It is clear that among occupational exposures that the aircrews are among the most consistently highly exposed individuals. In addition, a large fraction of these exposures are from high-energy

neutrons for which there is inadequate biological response data. It is also clear from table 20 that aircrew are among the highest exposed from neutrons as a result of their occupation. Still, the largest group exposures are those living in the high cities for which the present study is of great interest, especially in view of the uncertainty in the associated risk coefficients. The results of the present study for the development of the High Speed Civil Transport will reach beyond the objective of evaluation of the radiation safety of the associated operations to an improved understanding of the exposures of the world population which is of considerable interest (UNSCEAR 1993).

References

Akatov, Yu. A., Some results o dose measurements along civil airways in the USSR. Radiat. Prot. Dosimetry 48: 59-63; 1993.

Allkofer, O. C., Heinrich, W. (1974). "Measurement of galactic cosmic ray nuclei at supersonic transport altitudes and their dosimetric significance." Health Phys. 27, 543-551.

Armstrong, H., Haber, H., Strunghold, H. (1949), "Aero medical problems of space travel-panel meeting, School of Aviation Medicine," *J. Aviation Med.* **20**, 383-417.

Armstrong, T. W.; Chandler, K. C., Barish, J. (1973) "Calculation of neutron flux spectra induced in Earth's atmosphere by galactic cosmic rays." *J. Geophys. Res.* **78**, 2715.

Baarli, J. Radiological problems connected to exposure from cosmic radiation. Radiat. Prot. Dosimetry 48: 101-105; 1993.

Badhwar, G. D. (1997). Deep space radiation sources, models, and environmental uncertainties. In *Shield Strategies for Human Space Exploration,* J. W. Wilson, J. Miller, A. Konradi, and F. A. Cucinotta, eds. NASA CP-3360, pp.17-28, 1997.

Badhwar, G. D. , Cucinotta, F. A. , and O'Neill, P. M. (1994). An Analysis of Interplanetary Space Radiation Exposure for Various Solar Cycles, Radiat. Res. 138:201-208.

Bagshaw, M. Irvine, D., Davies, D. M., Exposure to cosmic radiation of British Airways flying crew on ultralonghaul routes. Occupational and Environmental Medicine **53**: 495-498; 1996.

Balasubramanyan, V. K., Bolt, E., Palmerira, R. A. R., Solar Modulation of Galactic Cosmic Rays, J. Geophys. Res. 72: 27-26; 1967.

Bazilevskaya, G.A., Svirzhevskaya, A. K. (1998). On the stratospheric measurements of cosmic rays. Space Sci. Rev. 85: 431-521.

Bethe, H. A., Korff, S. A., Placzek, G. (1940). "On the interpretation of neutron measurements in cosmic radiation," *Phys. Rev.* **57**, 573-587.

Bouville, A., Lowder, W.M. (1988) Human polulation exposure to cosmic radiation. Radiat. Prot. Dosim. 24: 293-299.

Cleghorn, T. F.; and Badhwar, G. D.(1997). Comparison of the SPE Model with Proton and Heavy Ion Data. *Impact of Solar Energetic Particle Events for Design of Human Missions Workshop*, September 9-11, 1997.

Cucinotta, F.A., Katz, R., Wilson, J.W. (1998) Radial distribution of electron spectra from high-energy ions. Radiat. Environ. Biophys. 37: 259-265.

Cucinotta, F.A., Katz, R., Wilson, J.W., Dubey, R.D., (1996) Radial dose distributions in the delta-ray theory of track structures. In: Proceedings of Two Center Effects in Ion-atom Collisions. AIP Conference Proceedings 362:245-265.

Cucinotta, F.A., W. Schimmerling, J.W., Wilson, L.E. Peterson, G.D. Badhwar, P. Saganti, J.F. Dicello, (2001) Space radiation cancer risks and uncertainties for Mars missions. *Radiat. Res*. **156**: 682-688.

Davies, D.M. (1993) Cosmic radiation in Concorde operations and the impact of new ICRP recommendations on commercial aviation. Radiat Prot. Dosim. 48: 121-124.

EPA (1984) Occupational Exposure to Ionizing Radiation in the United States: A Comprehensive Summary for the Year 1980 and a Summary of Trends for the years 1960-1985. EPA 520/1-84-005 (Environmental Protection Agency, Washington D.C.).

FAA Advisory Committee on the Radiobiological Aspects of the SST. "Cosmic radiation exposure in supersonic and subsonic flight." *Aviat., Space, & Environ. Med.* **46**: 1170-1185; 1975.

Fipov, R. A., Krisiuk, E.M. (1979) Radiation dose of the population of the Soviet Union from cosmic radiation. Atomnaja Energiya 47: 420-421.

Foelsche, T. (1961). Radiation Exposure in Supersonic Transports. NASA TN D-1383.

Foelsche, T., Mendell, R. B., Wilson, J. W., Adams, R. R. (1974). Measured and calculated neutron spectra and dose equivalent rates at high altitudes: relevance to SST operations and space research, NASA TN D-7715.

Fujii, Z., McDonald, F. B. Radial intensity gradients of galactic cosmic rays (1972-1995) in the heliosphere, J. Geophys. Res. 102(A11): 24,201-24,208; 1997.

Fujitaka, K., Abe, S. (1984a) Calculation on cosmic-ray muon exposure rate in non-walled concrete buildings. Radioisotopes 33: 350-356.

Fujitaka, K., Abe, S. (1984b) Modelling of cosmic-ray muon exposure in building's interior. Radioisotopes 33: 343-349.

Fujitaka, K., Abe, S. (1986) Effects of partition walls and neighboring buildings on the indoor exposure rate due to cosmic-ray muons. Health Phys. 51: 647-659.

Goldhagen, P., (2000) Overview of aircraft radiation exposure and recent ER-2 measurements. Proceedings No. *20 Cosmic Radiation Exposure of Airline Crews, Passengers, and Astronauts*. 1998 Annual Meeting of the NCRP, Washington, DC, March 30, 1998. Health Phys. **79**, 526-544.

Hajnal, F., Wilson, J. W. (1991). "High-altitude cosmic-ray neutrons: a significant contributor to the radiation exposures at aircraft altitudes." Seventh Symposium on Neutron Dosimetry, Berlin, October 14-18, 1991.

Hajnal, F., Wislon, J. W. (1992) High-altitude cosmic ray neutrons: probable source for the high energy protons at the earth's radiation belts. In Proc. 8th Congress Intl. Radiat. Prot. Ass. Montreal, p. 1620.

Hall, D. L., Duldig, M. L., Humble, J. E. (1996) Analysis of sidereal and solar anisotropies in cosmic rays, Space Sci. Rev. 17: 401-442.

Halliday, D. (1962). *Introductory Nuclear Physics*, Wiley and sons, New York, 1962.

Hess, V. F., And Eugster, J. (1949). *Cosmic Radiation and Its Biological Effects*, Fordham University Press, New York.

Hess, W. N., Canfield, E. H., Lingenfelter, R. E. (1961). "Cosmic-ray neutron demography." *J. Geophys. Res.* **66**, 665-667.

Hewitt, J. E., Hughes, J. B., McCaslin, et al. (1980) Exposure to cosmic-ray neutrons at commercial jet aircraft altitudes. Natural Radiation Environment III, Conf-780422, pp. 855-881.

Hughes, J. S., O'Riordan, M. C., Radiation Exposures of the UK Population-1993 Review. NRPB-R263, 1993.

Ibrahiem, N. M., Abd el Ghani, A. H., Shawky, S. M., Ashraf, E. M., Farouk, M. A. Measurement of radioactivity levels in soil in the Nile delta and Middle Egypt. Health Phys 64: 620-627; 1993.

ICAO, Annual Civil Aviation Report 1997. Available at www.icao.org/icao/en/jr/5306_ar3.htm, 1999.

ICRP (1991). *The 1990 Recommendations of the International Commission for Radiological Protection*, ICRP Report 60, Pergamon Press, Oxford, UK.

ICRP Task Group (1966). "Radiobiological aspects of the supersonic transport." Health Phys. 12, 209-226.

International Congress of Radiology, X-ray and Radium Protection, Br. J. Radiol. 1, 359-363: 1928.

Jenkins, C. E., Wogman, N. A., Rieck, H. G. (1972). "Radionuclide distributions in Olympic National Park, Wa." Water, Air, Soil Pollut. Vol. 1, p. 181.

Johnson, F. S. ed. (1965). *Satellite Environment Handbook*, Standford University Press.

Julius, H. W., van Dongen, R. (1985) Radaition doses to the population in the Netherlands, due to external natural sources. Sci. Total Environ. 45: 449-458.

Kim, M., Wilson, J. W., Kiefer, R. L., Thibeault, S. A. Effects of Isotope Selection on Solution Convergence in HZE Transport. NASA TP-3445, 1994.

Klement, A.W., Miller, C.R., Minx, R.P., Shleien, B. eds. (1972) Estimates of Ionizing Radiation Doses in the United States 1960-2000, ORP-CSD 72-1 (Environmental Protection Agency, Washington D.C.).

Kuhn, E., Schwamb, F. E., Payne, W. T. (1965) Solar Flare Haxard to Earth-Orbiting Vehicles. *Second Symposium on Protection Against Radiations in Space*, NASA SP-71, pp. 429-434.

Lal, D., Peters, B. (1967). "Cosmic ray produced radioactivity on the earth." Encyclopedia of Physics, Fluegge, S. and Sitte, K, Eds., vol. XLVI/2 on Cosmic Rays, Springer-Verlag, Berlin, p. 551.

Lauterbach, U., Kolb, W. (1978) Beitrag der kosmischen Strahlung zur naturlichen Strahlenbelastung in Wohnund Arbeitsraumen. Proceedings of the 12th Annual Meeting of the Fachverband fur Strahlenschutz e. V., in Radioaktivitat und Umwelt, II/993.

Mason, G. C., Radiation assessment of mineral sand and mining in Australia. Proceedings of the International Congress of International Radiation Protection Association (Vol. III), Pergamon Press, pp 1347-1350; 1988.

McCracken, K. G. (1962) The cosmic-ray flare effect. 1. Some new methods of analysis. J. Geophys. Res. 67:423-446.

McDonald, F. B., (1964). "Review of Galactic and Solar Cosmic Rays." *Second Symposium on Protection Against Radiations in Space,* Arthur Reetz , ed., NASA SP-71, 19-29.

Merker, M. (1973). "Contributions of galactic cosmic rays to atmospheric neutron maximum dose equivalent as function of neutron energy and altitude." *Health Phys*. **25**, 524.

Meyer, P., Parker, E. N., Simpson, J. A., Solar cosmic rays of February, 1956 and their propagation through interplanetary space. Phys. Rev. **104**: 768-781; 1956.

Miller, K.M., Beck, H.L. (1984) Indoor gamma and cosmic ray exposure rate measurements using a Ge spectrometer and pressurized ionization chamber. Radiat. Prot. Dosim. 7:185-189.

Montagne, C., Donne, J. P. Pelcot, D. et al. (1993) Inflight radiation measurements aboard French airliners. Radiat. Prot. Dosim. 48: 79-83.

Nakamura, T., Uwamino, Y., Ohkubo, T., Hara, A. (1987) Altitude variation of cosmic-ray neutrons. Health Phys. 53: 509-517.

NCRP (1987) Ionizing Radiation Exposure of the Population of the United States. Report No. 93.

NCRP (1987) Exposure of the population in the United States and Canada from Natural Background Radiation. Report No. 94.

NCRP (1995) Radiation Exposure and High Altitude Flight. NCRP Commentary No. 12.

National Council on Radiation Protection, Principles and Application of Collective Dose in Radiation Protection. NCRP Report 121, 1995.

NCRP, *Exposure of the Population in the United States and Canada from Natural Background Radiation*. NCRP Report No. 94, 1987.

Neher, H. V. (1961). "Cosmic-ray knee in 1958." J. Geophysical Res. 66, 4007-4012.

Neher, H. V. (1967). "Cosmic-ray particles that changed from 1954 to 1958 to 1965.", J. Geophys. Res. 72: 1527-1539.

Neher, H. V. (1971). "Cosmic rays at high latitudes and altitudes covering four solar maxima," J. Geophys. Res. 76: 1637-1851.

Neher, H. V., Anderson, H. R. (1962). "Cosmic rays at balloon altitudes and the solar cycle." J. Geophysical Res. 67, 1309-1315.

Neher, H. V., Pickering, W. H. (1942). "Results of a high altitude cosmic ray survey near the magnetic equator". Phys Rev. 61: 407-413.

Nymmik, R. A. (1997). Space environment (natural and artificial) – Probabilistic Model for Fluences and Peak Fluxes of Solar Cosmic Ray Particles. International Standard ISO WD 15391.

Oakley, D. T., Natural radiation exposures in the United States. USEPA Report ORP/SID-72-1; 1972.

O'Brien, K., Friedberg, W. (1994). "Atmospheric cosmic rays at aircraft altitudes." *Enviornment International* **20**, 645-663.

Parker, E. N. (1965).The Passage of Energetic Charged Particles Through Interplanetary Space, Planetary Space Sci. 13: 9-49.

Parker, J. F. West, V. R., eds. (1973) Bioastronautics Data Book, Second edition, NASA SP-3006.

Pearson, J. E., Natural Environmental Radioactivity from Radon-222, US Public Health Service Pub. 999-RH-26.

Pfeiffer, W. C., et al. Measurements of environmental radiation exposure dose rates at selected sites in Brazil, An. Acad. Bras. Cienc. 53: 683-691; 1981.

Preston, F. S., Eight years; experience of Concorde operations: medical aspects. *J. Royal Soc. Med.* **78**:193-196; 1985.

Reames, D.V., (1999) Particle accereration at the sun and in the heliosphere. Space Sci. Rev. 90: 417-491.

Roesler, S., Heinrich, W., Schraube, H. (1998). "Calculation of Radiation Fields in the Atmosphere and Comparison to Experimental Data." *Radiat. Res.* **149**, 87-97.

Schaefer, H. J. (1950). "Evaluation of present-day knowledge of cosmic radiation at extreme altitude in terms of the hazard to health," *J. Aviation Med.* **21**, 375-94.

Schaefer, H. J. (1959). "Radiation and man in space." *Adv. Space Res.* **1**, 267-339.

Schimmerling, W. , Wilson, J. W. , Cucinotta, F. A., Kim, M. Y. (1998). Evaluation of risks from space radiation with high-energy heavy ion beams, Physica Medica **14** (Suppl. 1): 29-38.

Schraube, H., Leuthold, G., Roesler, S., Heinrich, W. (1998). Neutron spectra at Flight Altitudes and Their Radiological Estimation." *Adv. in Space Res.* 21: 1727-1738; 1998.

Shea, M. A., Smart, D. F. (1993). "History of energetic solar protons for the past three solar cycles including cycle 22 update." *Biological Effects and Physics of Solar and Galactic Cosmic Radiation,* C. E. Swenberg, G. Horneck, G. Stassinopoulos, eds. Plenum Press, 37-71.

Shea, M. A.; and Smart, D. F. (1983). A world grid of calculated cosmic ray vertical cutoff rigidities for 1980.0. *18th International Cosmic Ray Conference-Conference Papers*, MG Sessions, Vol. 3, Tata Inst. Of Fundamental Research (Colaba, Bombay), 415-418.

Shea, M. A.; and Smart, D. F. (1990). A Summary of Major Solar Proton Events. Solar Physics, **127**, pp. 297-320.

Shinn, J.L., Wilson, J.W. (1991) Nuclear Reaction Effects in Use of Newly Recommended Quality Factor. Health Physics, 61: 415-419.

Simpson, J. A. (1983). Elemental and isotopic composition of the galactic cosmic rays. Annual Rev. of Nucl. and Part. Sci. 33: 323-381.

Störmer, C. (1955). *The Polar Aurora,* Oxford at the Clarendon Press.

Störmer, C. (1930). Periodische Elektronenbahen im Felde eines Elementarmagneten und ihre Anwendung auf Bruches Modellversuche und auf Eschenhagens Elementarwellen des Ermagnetismus. *Z. Astrophys.*, Bd. 1, pp. 237-274.

Sunta, C. M. A review of the studies of high background areas of the S-W coast of India. Proceedings of the International Conference on High Levels of Natural Radiation, Ramsar, IAEA, pp. 71-86; 1993.

Tobias, C. A. (1952). Radiation hazards in high altitude aviation. J. Aviat. Med. 23: 345-372.

Tsui, K. C., Wong, M. C. Lee, B. Y., (1991) Field estimation of cosmic contribution to total external gamma radiation in Hong Kong. Environmental Radiation Monitoring, Hong Kong, Technical Report No. 4.

UNSCEAR Ionizing Radiation: Sources and Biological Effects. UN publ. E.82.IX.8, 1982.

UNSCEAR, Sources, Effects, and Risks of Ionizing Radiation. UN publ. E.88.IX.7, 1988.

UNSCEAR Sources and Effects of Ionizing Radiation. UN publ E.94.IX.2, 1993.

Upton, A. C. (1989). *Radiobiology and Radiation Protection: The Past Century and Prospects for the Future*. NCRP Lecture No. 13, Bethesda.

Van Dongen, R., Stoute, J. R. D. Outdoor nautral background radiation in the Netherlands. Science of the Total Environ. 45: 381-388; 1985.

Von Frieben, A. (1903). "Hodenverauderungen bei tieren nach Rontgenstrahlung," *Muchen Med. Wuhnschi* **50**, 2295.

Wallace, R.G., Sondhaus, C. A. (1978). "Cosmic ray exposure in subsonic air transport." Aviation Space, & Environ. Med. 74, 6494-6496.

Webber, W. R., Ormes, J. F. (1967). "Cerenkof-scintillation counter measurements of nuclei heavier than helium in the primary cosmic radiation. 1. Charge composition and energy spectra between 200 MeV/nucleon and 5 beV/nucleon." J. Geophys. Res.--Space Phys. 72, 5957-5976.

Wehr, M. R., Richards, J. A. (1960). *Physics of the Atom*, Addison-Wesley Publ., Reading, MA.

Weng, P.-S., Chen, C.-F. (1987) Cosmic-ray ionization in the lower atmsophere. Health Phys. 52: 347-352.

Weng, P.-S., Chu, T.-C., Chen, C.-F., Natural radiation background in metropolitan Taipei, J. Radiat. Res. 32: 165-174; 1991.

Wilson, J. W., Lambiotte, J. J., Foelsche, T., Filippas, T. A. (1970). *Dose Response Functions in the Atmosphere Due to Incident High-energy Protons with Application to Solar Proton Events*. NASA TN D-6010.

Wilson, J. W., Denn, F. M. (1976). *Preliminary Analysis of the Implications of Natrural Radiations on Geostationary Operations*. NASA TN D-8290.

Wilson, J. W., Townsend, L. W. (1988) Radiation safety in commercial air traffic: a need for further study. Health Phys 55: 1001-1003 and Health Phys. 56: 973-974.

Wilson, J. W., Shinn, J. L., Townsend, L. W. (1990). "Nuclear reaction effects in conventional risk assessment for energetic ion exposures." *Health Phys*. **58**, 749-752.

Wilson, J. W., Townsend, L. W., Badavi, F. F. (1987). Galactic HZE propagation through the earth's atmosphere. Radiat. Res. 109:173-183.

Wilson, J.W., Cucinotta, F.A., Hajnal, F. (1991a)Analytical Relationships of Nuclear Fields and Microdosimetric Quantities for Target Fragmentation in Tissue Systems. Health Phys. 60, 559.

Wilson, J. W., Townsend, L. W., Schimmerling, W., Khandelwal, G. S., Khan, F., Nealy, J. E., Cucinotta, F. A., Simonsen, L. C., Shinn, J. L., Norbury, J. W. (1991b) Transport methods and interactions for space radiation. NASA RP-1257.

Wilson, J. W., Nealy, J. E., Cucinotta, F. A., Shinn, J. L., Hajnal, F., Reginatto, M., Goldhagen, P. (1995) Radiation safety aspects of commercial high-speed flight transportation. NASA TP-3524.

Wilson, J.W. (2000) Overview of radiation environments and human exposures. *Health Phys*. **79**: 470-494.

Wilson, O. J., Young, B. F., Richardson, C. K., Cosmic radiation doses received by asutralian commercial flight crews and the implications of ICRP 60. *Health Phys*. **66**: 493-502; 1994.

Yanagisawa, K. Muramatsu, Y. Transfer factors of technetium from soil to vegetables, Radiochimica Acta. 63: 83-86; 1993.

Yanagisaw, K. Muramatsu, Y., Transfer of technetium from soil to paddy and upland rice. J. Radiat. Res. 36: 171-178; 1995.

Yue, Q. Y., Jin, H. (1987) Measurement of ionization distribution in the lower atmosphere caused by cosmic ray. In Proceedings of Workshop on Occupational and Environmental Radiation Protection, Hong Kong.

Table 1. Principal nuclear decay sequence of Actinium Series (U-235).

Isotope	Lifetime	Decay mode(s)	Decay energy, MeV
U-235	7.1x10^8 yr	α	4.4
Th-231	25.5 h	-e	0.09 - 0.3
Pa-231	3.2x10^4 y	α	5.0
Ac-227	21.6 y	-e	0.05
Th-227	18.2 d	α	5.8 – 6.0
Ra-223	11.4 d	α	5.5-5.7
Rn-219	4.0 s	α	6.4-6.8
Po-215	1.8x10^-3 s	α	7.4
Pb-211	36.1 min	-e	1.4, 0.5
Bi-211	2.15 min	α	6.3, 6.6
Tl-207	4.79 min	-e	1.44
Pb-207	–	--	--

Table 2. Principal nuclear decay sequence of the Uranium Series (U-238).

Isotope	Lifetime	Decay mode(s)	Decay energy, MeV
U-238	4.5x10^9 yr	α	4.2
Th-234	24.1 d	-e	0.2, 0.1
Pa-234	1.17 min	-e	2.3
U-234	2.45x10^5 yr	α	4.7-4.8
Th-230	7.7x10^4 yr	α	4.6-4.7
Ra-226	1600 yr	α	4.8
Rn-222	3.82 d	α	5.5
Po-218	3.05 min	α	6.0
Pb-214	26.8 min	-e	0.7, 1.0
Bi-214	19.9 min	-e	0.4-3.3
Po-214	1.64x10^-4 s	α	7.7
Pb-210	22.3 yr	-e	~0.1
Bi-210	5.01 d	-e	1.2
Po-210	138 d	α	5.3
Pb-206	–	--	--

Table 3. Principal nuclear decay sequence of Thorium Series (Th-232).

Isotope	Lifetime	Decay mode(s)	Decay energy, MeV
Th-232	1.4x10^10 yr	α	4.0
Ra-228	5.75 yr	-e	~0.1
Ac-228	6.13 h	-e	0.4-2.2
Th-228	1.91 yr	α	5.3, 5.4
Ra-224	3.66 d	α	5.7
Rn-220	55.6 d	α	6.3
Po-216	0.15 s	α	6.8
Pb-212	10.6 h	-e	0.3, 0.6
Bi-212	60.6 min	-e (64%) a (36%)	2.2, 6.1
Tl-208	3.07 min	-e	1.0-1.8
Po-212	3.05x10^-7 s	α	8.8
Pb208	–	--	--

Table 4. Concentrations (Bq/kg) of radioactivity in major rock types and soils (NCRP 1987)

Rock type	K-40	Rb-87	Th-232	U-238
Igneous rocks				
Basalt (average)	300	30	10-15	7-10
Mafic	70-400	1-40	7-10	7-10
Salic	1100-1500	150-180	60-80	50-60……
Granite (average)	>1000	150-180	70	40
Sedimentary rocks				
Shale sandstones:	800	110	50	40
Clean quartz	<300	<40	<8	<10
Dirty quartz	400?	80?	10-25?	40?
Arkose	600-900	80	<8	10-25?
Beach sands (unconsolidated)	<300	<40	25	40
Carbonate rocks	70	8	8	25
Continental upper crust				
Average	850	100	44	36
Soils	400	50	37	66

Table 5. Concentrations (Bq/kg) of radioactivity in soil of Nordic countries (Christen et al 1990).

Soil type	K-40	Ra-226	Th-232
Sand and silt	600-1200	5-25	4-30
Clay	600-1300	20-120	25-80
Moraine	900-1300	20-80	20-80
Soils with Alum shale	600-1000	100-1000	20-80

Table 6. Mean concentrations (Bq/kg) of radioactivity in the Nile delta and middle Egypt (Ibrahiem et al. 1993).

Soil type	K-40	U-238	Th-232
Coastal sand (monazite, zirconium)	223.6	26.4	47.7
Sand	186.4	10.7	9.8
Sandy loam and sandy clay	288.6	14.8	15.5
Clay loam and silty loam	317.	15.5	17.9
Loam	377.5	19.6	19.1
Clay	340.7	15.5	17.9

Table 7. Concentrations of natural radionuclides and absorbed dose rates in air (UNSCEAR 1993).

Radionuclide	Concentration (Bq/kg)		Dose Coefficient (nGy/h per Bq/kg)	Dose rate (nGy/h)	
	Mean	Range		Mean	Range
China					
K-40	580 ± 200	12 - 2190	0.0414	24	0.5 - 90
Th-232 series	40 ± 28	1.5 - 440	0.623	31	0.9 - 270
U-238 series	40 ± 34	1.8 - 520	--	See Ra subseries	--
Ra-226 subseries	37 ± 22	2.4 - 430	0.461	17	1.1 - 200
Total				72	2 - 560
United States					
K-40	370	100 - 700	0.0414	15	4 - 29
Th-232 series	35	4 – 130	0.623	22	2 – 81
U-238 series	35	4 – 140	--	See Ra subseries	
Ra-226 subseries	40	8 – 160	0.461	18	4 – 74
Total				55	10 - 200

Table 8. Estimated absorbed dose rates in air within masonry dwellings (UNSCEAR 1993).

Material	Concentration (Bq/kg)			Activity utilization index[a]	Absorbed dose rate in air for indicated fractional mass of building material (nGy/h)			
	C_K	C_{Ra50}	C_{Th}		1.0	0.75	0.5	0.25
Typical masonry	500	50	50	1.0	80	60	40	20
Granite blocks	1200	90	80	1.9	140	105	70	35
Coal ash aggregate	400	150	150	2.4	180	135	90	45
Alum shale concrete	770	1300	67	9.0	670	500	390	170
Phosphogypsum	60	600	20	3.9	290	220	145	70
Natural gypsum	150	20	5	0.25	20	15	10	5

[a]Assuming full utilization of materials

Table 9. Conversion coefficients from air kerma to effective dose for terrestrial gamma rays (UNSCEAR 1993).

Radionuclides	Conversion coefficient (Sv per Gy)		
	Adults	Children	Infants
K-40	0.74	0.81	0.95
Th-232 series	0.72	0.81	0.92
U-238 series	0.69	0.78	0.91
Overall	0.72	0.80	0.93

Table 10. Fluence levels of solar events of cycle 19-22 associated with ground level events.

Date			Proton fluence (p/cm^2) at energies greater than--	
Month	Day(s)	Year	10 MeV	30 MeV
2	23	56	$2x10^9$	$1x10^9$
7	10-11	59	$5x10^9$	$1x10^9$
7	14-15	59	$8x10^9$	$1x10^9$
7	16-17	59	$3x10^9$	$9x10^8$
11	12-13	60)[a]	$8x10^9$	$2x10^9$
11	15	60	$3x10^9$	$7x10^8$
7	18	61	$1x10^9$	$3x10^8$
11	18	68	$1x10^9$	$2x10^8$
4	11-13	69	$2x10^9$	$2x10^8$
1	24-25	71	$2x10^9$	$4x10^8$
8	4-9	72)[b]	$2x10^{10}$	$8x10^9$
2	13-14	78	$2x10^9$	$1x10^8$
4	30	78	$2x10^9$	$3x10^8$
9	23-24	78	$3x10^9$	$4x10^8$
5	16	81	$1x10^9$	$1x10^9$
10	9-12	81	$2x10^9$	$4x10^8$
2	1-2	82	$1x10^9$	$2x10^8$
4	25-26	84	$1x10^9$	$4x10^8$
8-9	12-7	89	$8x10^9$	$2x10^8$
9-10	29-13	89	$4x10^9$	$1x10^9$
10-11	19-9	89	$2x10^{10}$	$4x10^9$
11-12	26-5	89	$2x10^9$	$1x10^8$

[a]Foelsche et al (1974)

[b]Wilson and Denn (1976)

Table 11. Relation of Magnetic Indices to Magnetic Storm Field Strength

K_p	a_p	$\lvert H_{st} \rvert$, nT
0	0	0
1	4	8
2	7	14
3	15	30
4	27	54
5	48	96
6	80	160
7	132	264
8	207	414
9	400	800

Table 12. Ionization Rates in Air Measured by Argon-Filled Chambers[a] at Solar Minimum (C = 98.3 in 1965)

R, GV	Ion pairs, cm^{-3}, for air depths, g/cm^2, of—													
	30	40	50	60	70	80	90	100	120	140	200	245	300	1034
0	445.0	430.0	414.0	399.0	383.0	366.0	349.0	332.0	298.0	266.0	181.0	136.0	95.0	11.4
.01	445.0	430.0	414.0	399.0	383.0	366.0	349.0	332.0	298.0	266.0	181.0	136.0	95.0	11.4
.16	444.0	430.0	414.0	399.0	383.0	366.0	349.0	332.0	298.0	266.0	181.0	136.0	95.0	11.4
.49	411.8	404.3	394.4	382.0	369.0	354.8	339.4	325.0	292.3	264.5	181.0	136.0	95.0	11.4
1.97	325.0	333.0	340.0	335.0	330.0	312.5	308.0	300.0	285.0	264.0	181.0	134.0	95.0	11.4
2.56	300.0	305.0	310.0	305.0	300.0	290.0	285.0	280.0	255.0	230.0	173.0	126.0	95.0	11.4
5.17	185.0	195.0	208.0	208.0	208.0	208.0	208.0	208.0	195.0	185.0	135.0	103.0	75.0	10.6
8.44	127.6	137.0	145.0	150.2	153.8	155.8	156.0	154.6	149.7	142.2	111.3	87.0	66.6	10.4
11.70	85.0	92.0	98.0	100.0	102.0	105.0	107.0	110.0	108.0	105.0	80.0	77.0	60.0	10.0
14.11	70.0	75.0	82.0	85.0	89.0	93.6	95.0	100.0	98.0	95.0	78.0	68.8	50.0	10.0
17.00	66.3	73.8	80.0	84.8	88.5	91.1	92.6	93.5	93.4	90.5	75.0	62.3	48.0	10.0

[a]Experimental data extrapolated to provide estimates of ionization rates over a wide range of altitudes and geomagnetic cutoffs.

Table 13. Ionization Rates in Air Measured by Argon-Filled Chambers[a] at Solar Maximum (C = 80 in 1958)

R, GV	Ion pairs, cm^{-3}, for air depths, g/cm^2, of—													
	30	40	50	60	70	80	90	100	120	140	200	245	300	1034
0	264.6	267.5	267.0	265.0	258.0	252.0	243.0	235.0	216.3	197.0	145.0	109.2	78.8	11.4
.01	264.6	267.8	267.0	265.0	258.0	251.0	243.0	235.0	216.3	197.0	145.0	109.2	78.8	11.4
.16	264.0	264.9	265.0	264.0	257.0	250.0	243.0	233.0	215.0	197.0	145.0	109.2	78.8	11.4
.49	264.0	264.9	265.0	262.0	256.0	249.0	242.0	231.0	213.2	197.0	145.0	109.2	78.8	11.4
1.97	264.0	265.0	265.0	262.0	252.0	245.0	241.0	231.0	212.5	197.0	145.0	107.8	78.8	11.4
2.56	235.0	237.5	240.0	240.0	239.0	238.0	237.0	230.0	209.0	197.0	145.0	101.6	78.8	11.4
5.17	162.5	168.0	179.0	182.0	178.0	175.2	174.0	173.8	170.0	160.0	159.0	88.3	65.0	10.6
8.44	95.0	103.5	112.0	118.0	118.0	119.0	120.0	122.0	118.0	117.0	100.6	78.7	60.2	10.4
11.70	78.2	85.0	90.7	92.7	94.8	98.0	100.0	103.1	101.2	98.4	75.0	72.2	56.2	10.0
14.11	65.7	70.7	77.5	80.5	84.3	89.0	90.5	95.5	93.5	90.9	74.0	65.9	47.9	10.0
17.0	63.0	70.3	76.4	81.4	84.8	87.5	89.1	90.2	90.1	87.4	72.6	60.3	46.5	10.0

[a]Experimental data extrapolated to provide estimates of ionization rates over a wide range of altitudes and geomagnetic cutoffs.

Table 14. Cosmogenic radionuclides contributing to human exposures (Lal and Peters 1967).

Radionuclide	Half-life	Main decay modes	Target nucleus	Global Inventory
Hydrogen-3	12.33 years	β 18.6 keV	N, O	3.5 kg
Berylium-7	53.3 days	Electron conversion, γ 477 keV	N, O	3.2 g
Carbon-14	5730 years	β 156 keV	N, O	68 mt
Sodium-22	2.60 years	β^+ 545, 1,820 keV; γ 1,275, 511 keV	Ar	1.9 kg

Table 15. Cosmic ray absorbed dose rate in the center of a 12 storey building in NY, NY (Miller and Beck 1984)

Level	Dose rate, nGy/h	Transmission factor
Roof	31.4	1
12	20.2	0.64
10	20.2	0.64
8	18.1	0.58
5	17.4	0.55
4	13.7	0.44
2	11.5	0.37
Basement	8.6	0.27

Table 16. Cosmic ray shielding factors in various dwellings

Dwelling	Sheilding factor	Reference
20 cm concrete	0.85	Lauterbach and Kolb 1978
Single homes, wood ceilings	0.82	Julius and van Dongen 1985
Row houses and office buildings, wood ceilings	0.76	Julius and van Dongen 1985
Dwellings with concrete ceilings and floors	0.50	Julius and van Dongen 1985
Apartment buildings	0.42	Julius and van Dongen 1985
Wooden houses	0.81-0.96	Fipov and Krisiuk 1979
Stone buildings	0.72-0.92	Fipov and Krisiuk 1979
Modern buildings	0.54-0.86	Fipov and Krisiuk 1979

Table 17. Average annual exposures to cosmic rays (UNSCEAR 1993)

Location	Population (millions)	Altitude (m)	Annual effective dose (μSv)		
			Ionizing	Neutron	Total
High-altitude cities					
La Paz, Bolivia	1.0	3,900	1,120	900	2,020
Lhasa, China	0.3	3,600	970	740	1,710
Quito, Ecuador	11.0	2,840	690	440	1,130
Mexico City, Mexico	17.3	2,240	530	290	820
Nairobe, Kenya	1.2	1,600	410	170	580
Denver, United States	1.6	1,610	400	170	570
Tehran, Iran	7.5	1,180	330	110	440
Sea level			240	30	270
World average			300	80	380

Table 18. *Neutron exposure estimates for radiation workers for the year 1980.* (NCRP 1987)

Occupational category	Number of exposed individuals	Average annual effective dose equivalent (mSv)	Collective effective dose equivalent (person- Sv)
US DOE contractors	25, 000	2.6	64
US Nuclear power	1,100	0.5	0.6
US Navy	12,000	0.24	2.9
Totals	38,100	1.8 (mean)	67.5

Table 19. Atmospheric dose equivalent rates measured onboard the TU-144 during March to June 1977 near Solar minimum (Akatov 1993).

	Radiation levels at latitudes of --					
	40°- 45° N		46°- 58° N		65°- 72° N	
Altitude, km	Ionising, μGy/hr	Neutron, μSv/hr	Ionising, μGy/hr	Neutron, μSv/hr	Ionising, μGy/hr	Neutron, μSv/hr
13	2.3	2.6	2.9	4.2	3.5	5.0
14	2.6	3.0	3.2	5.0	4.1	5.9
15	2.8	3.0	3.4	5.4	4.7	6.7
16	2.9	3.2	3.5	5.8	5.2	7.6
17	3.0	3.5	3.7	6.1	-	-
18	3.1	3.4	3.8	5.5	-	-

Table 20. Neutron collective dose equivalents for various exposed groups.

Category	Collective dose equivalent, person-Sv
Occupational worker	338
Commercial aircraft operations	7,200
High cities	12,280

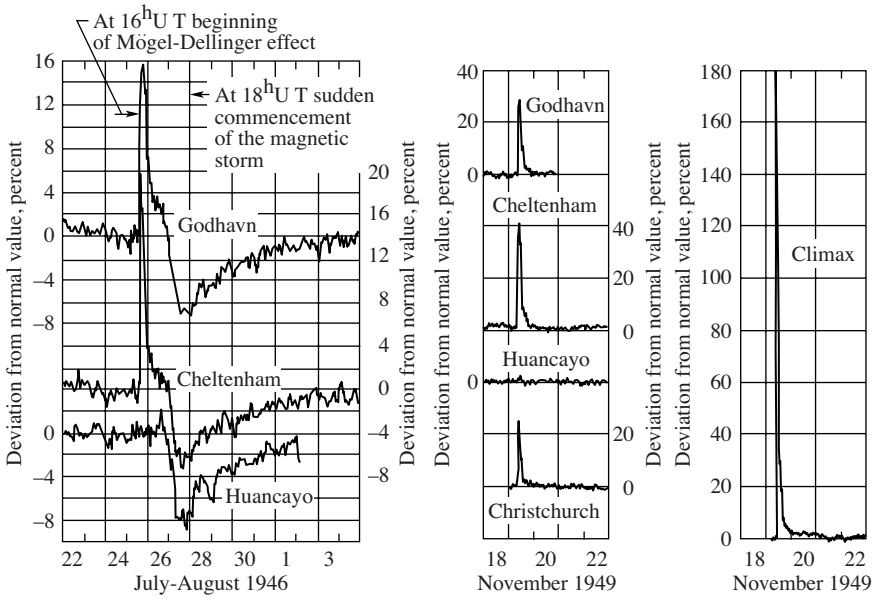

Figure 1. Ground level ion chamber observations of solar particle events of 1946 and 1949. (From Foelsche et al. 1974).

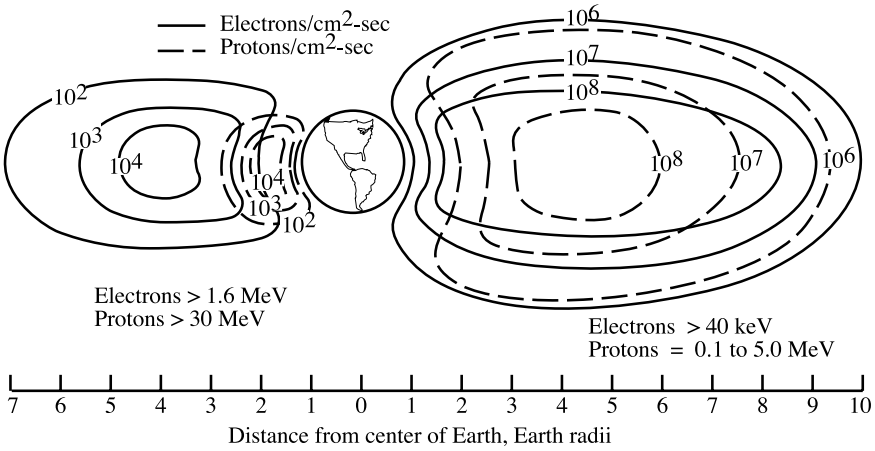

Figure 2. Near-Earth trapped radiation (Parker and West 1973).

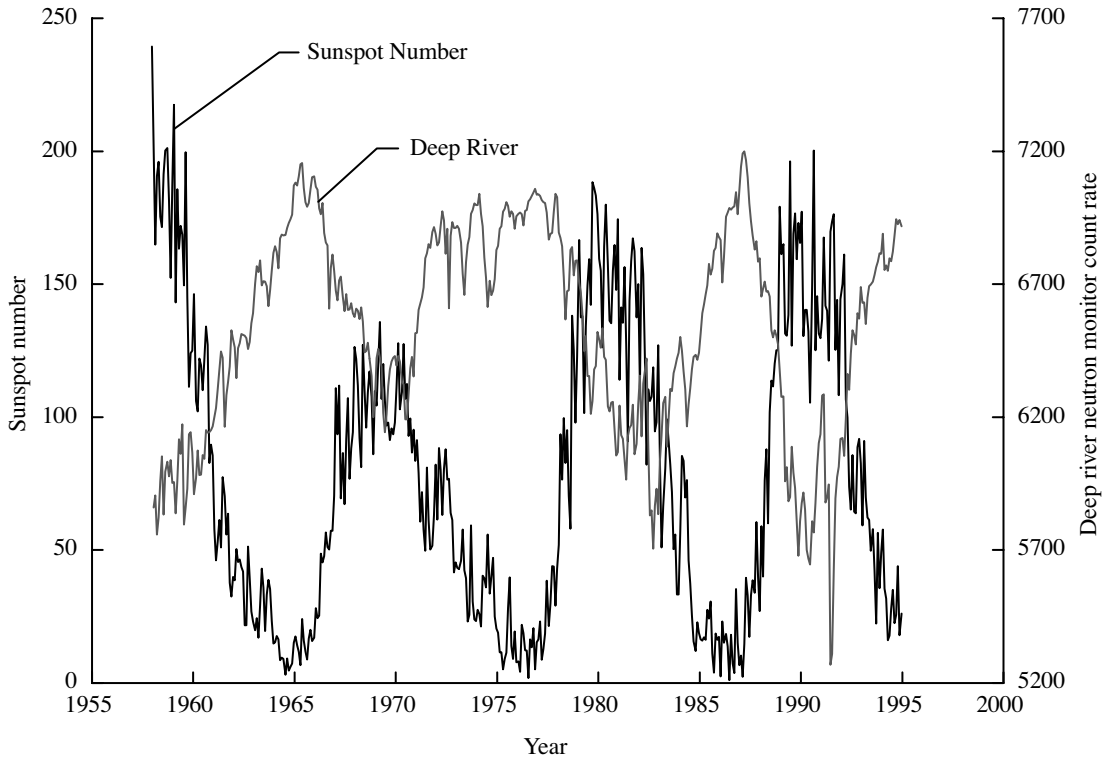

Figure 3. Sunspot number and Deep River neutron monitor count rate over the last few solar cycles.

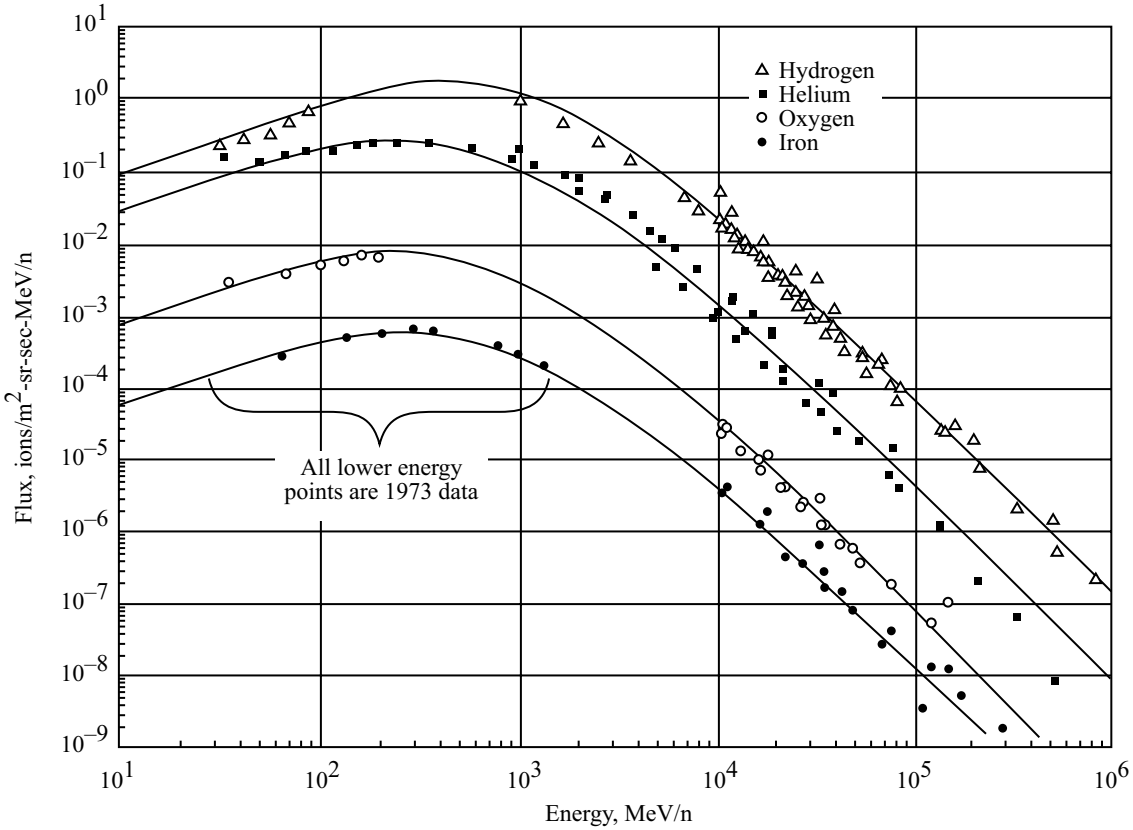

Figure 4. Fit the Fokker-Planck diffusion equation to 1973 differential energy spectra (Badhwar et al. 1994).

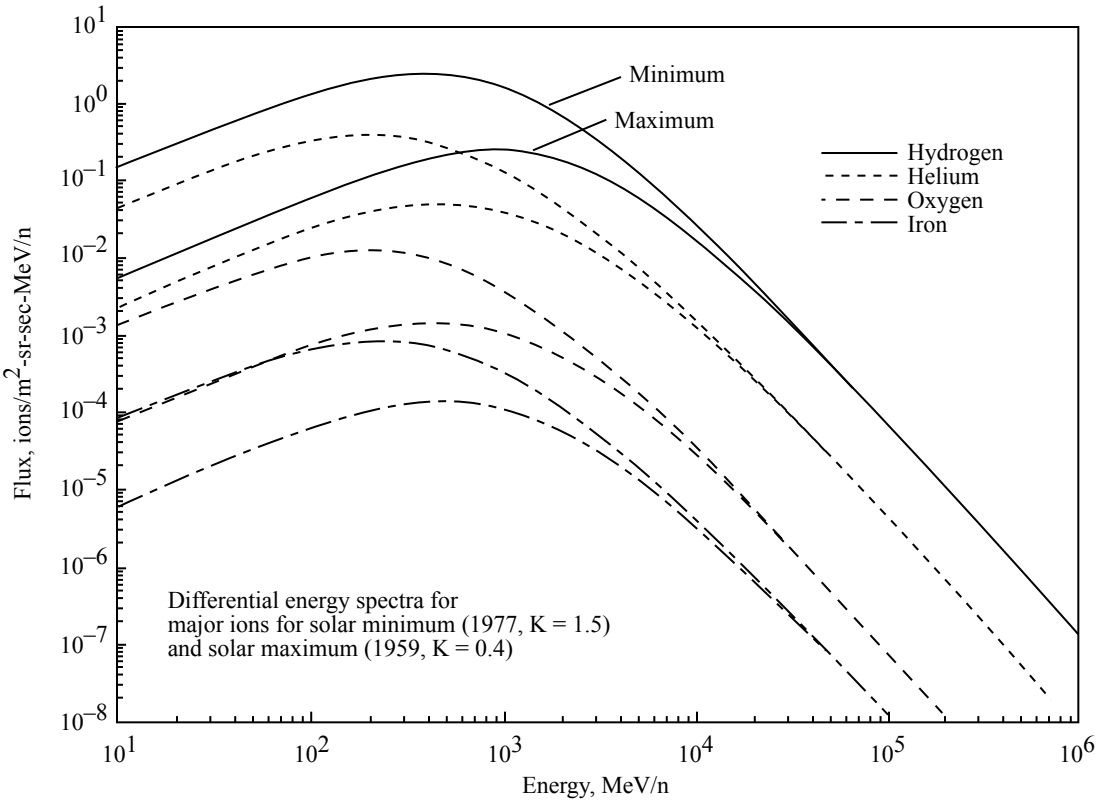

Figure 5. "Worst-case" differential energy spectra during solar minimum and solar maximum (Badhwar et al. 1994).

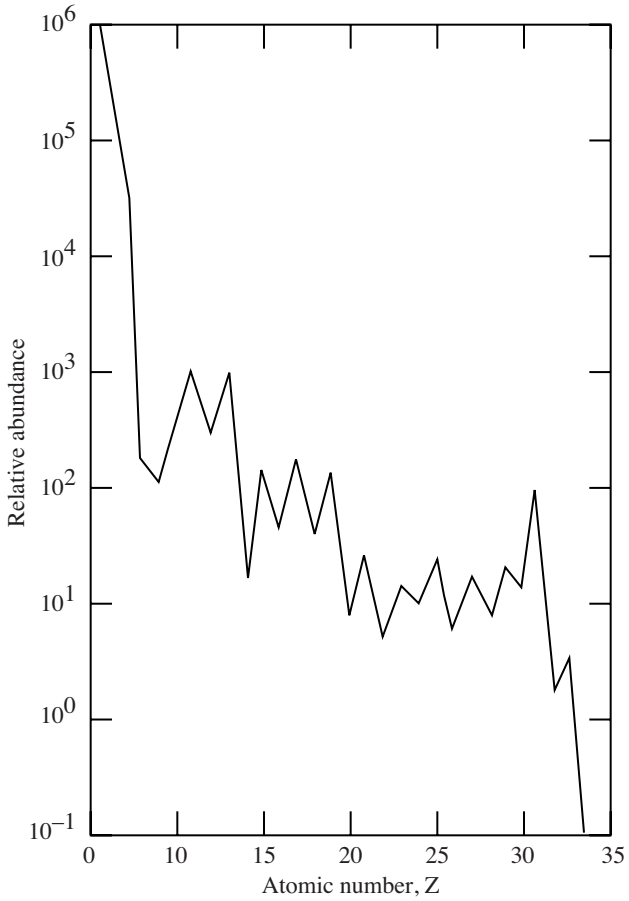

Figure 6. The charge distribution of GCR particles in atomic number (Simpson 1983).

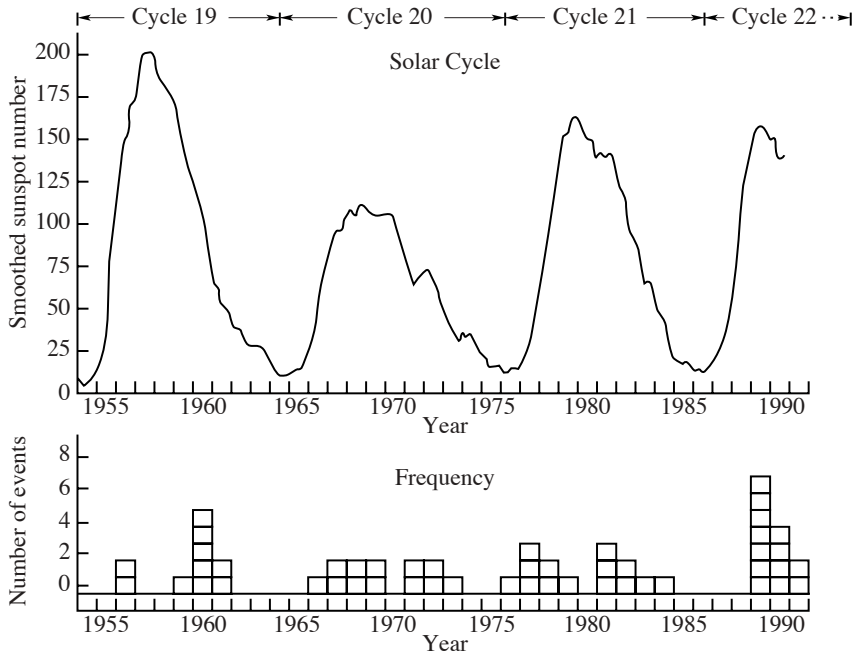

Figure 7. Temporal distribution of ground level solar particle events for the past 40 years. (Shea and Smart 1993).

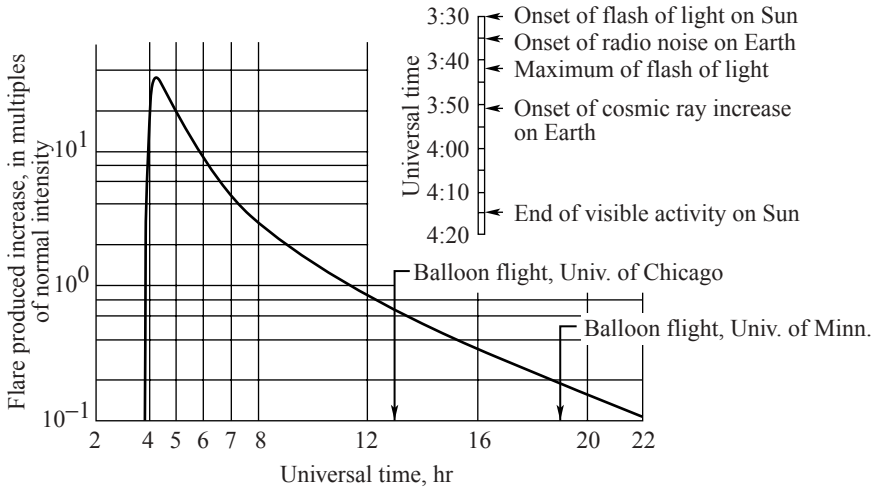

Figure 8. Ground level neutron monitor event seen at Durham, NH on Feb. 23, 1956. (Schaefer 1959).

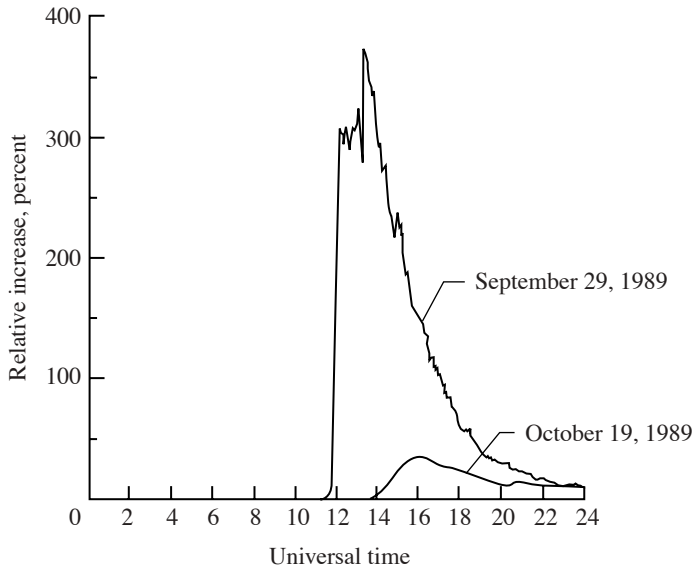

Figure 9. Deep River neutron monitor count rates during the solar particle events of October 19 and September 29 of 1989.

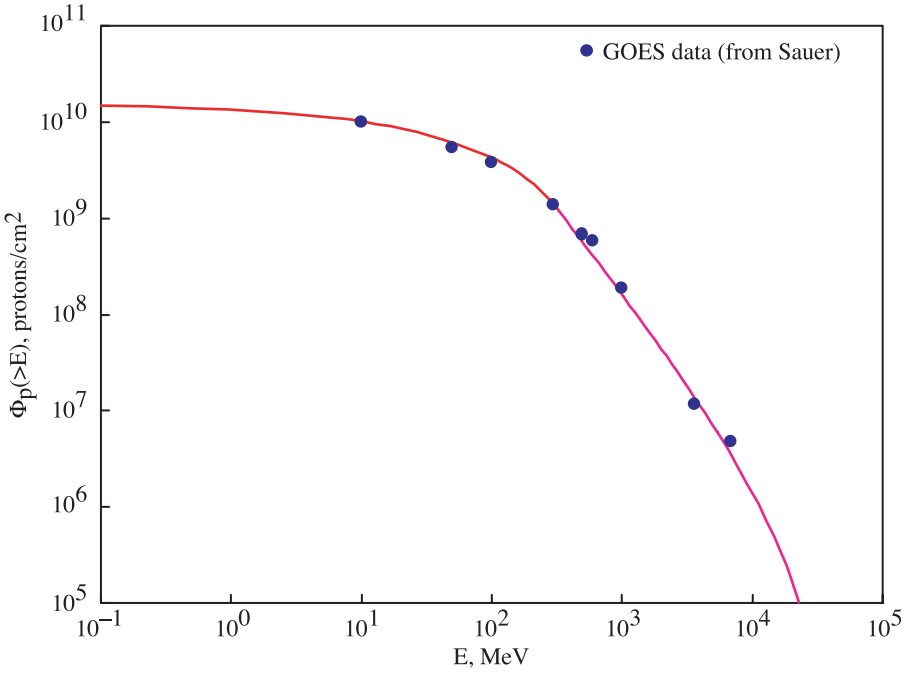

Figure 10. Solar particle event fluence spectra for the September 29, 1989 event.

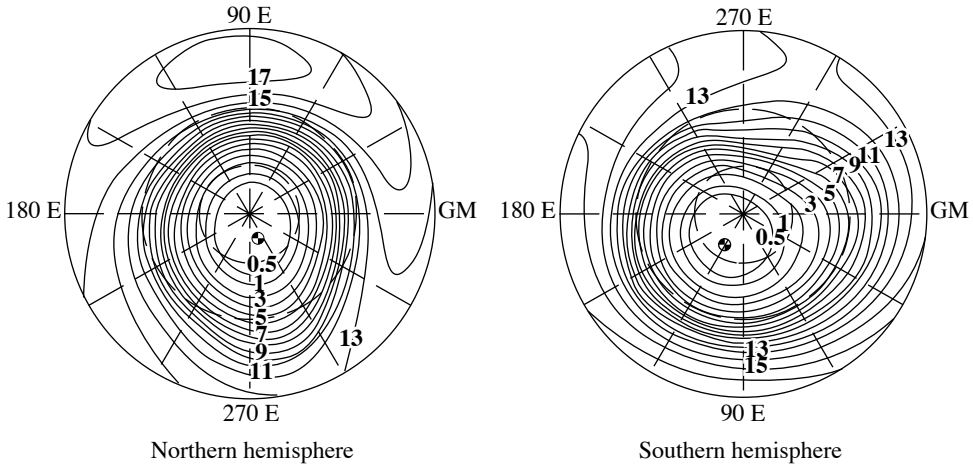

Figure 11. Contour of vertical geomagnetic cutoff values from data of Smart and Shea (1983). Contour increments are 1 GV except for the lowest (0.5 GV) contour. Magnetic pole locations are indicated.

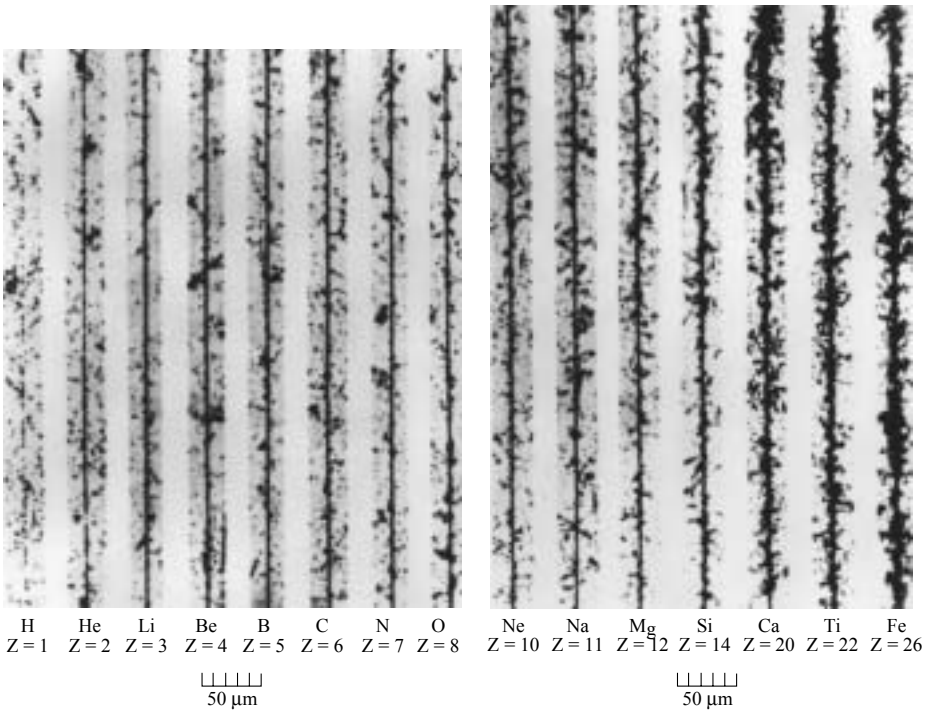

Figure 12. Cosmic-ray ion tracks in nuclear emulsion. (McDonald 1964).

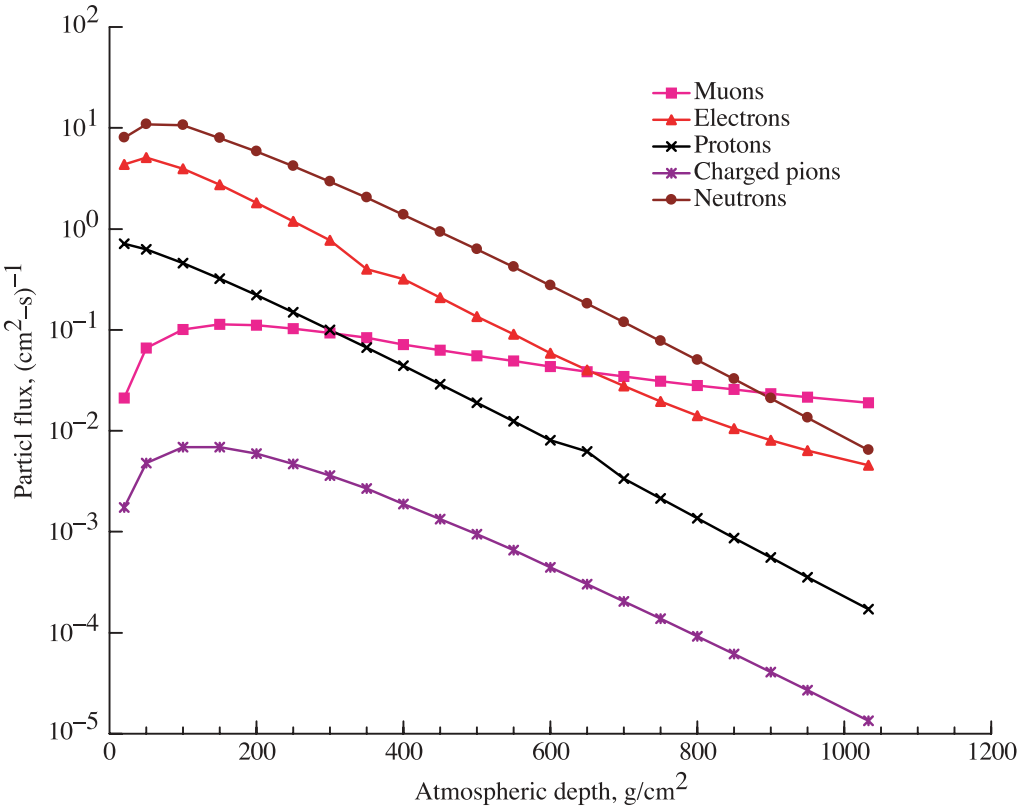

Figure 13. Calculated particle flux at 50° geomagnetic latitude as given by the NCRP (1987). Photon flux is not shown.

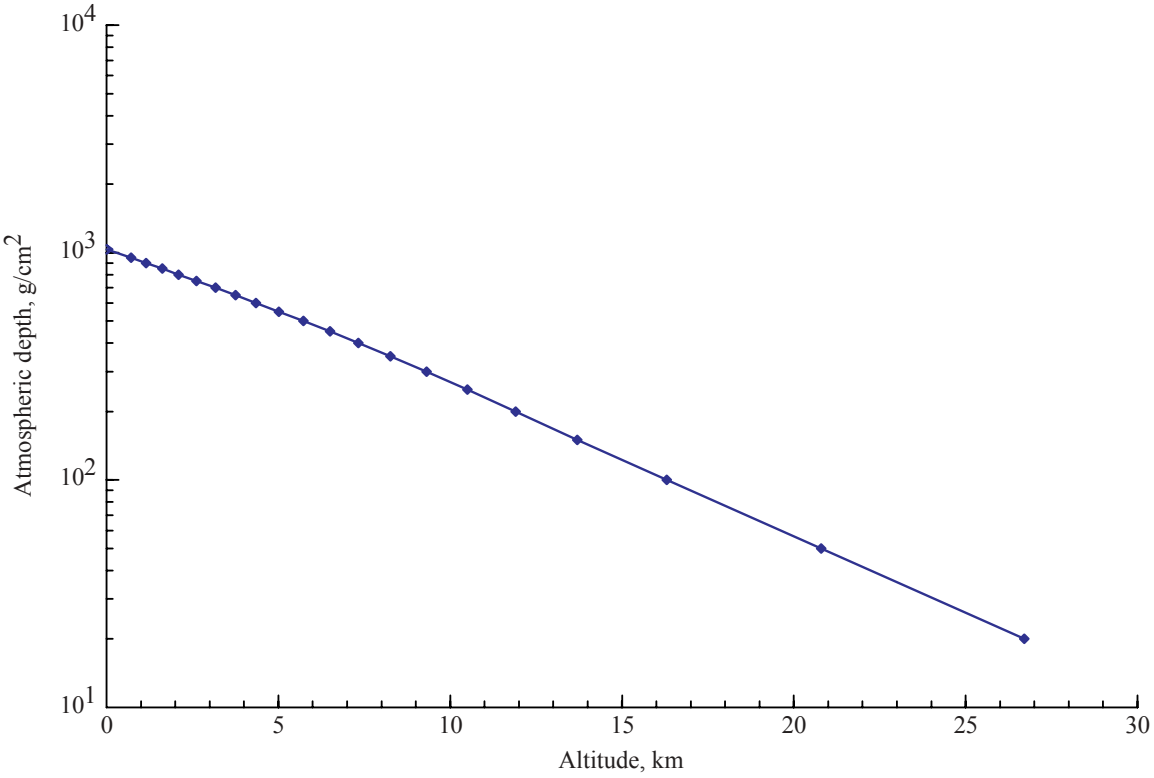

Figure 14. Atmospheric depth as a function of altitude as given by the NCRP (1987).

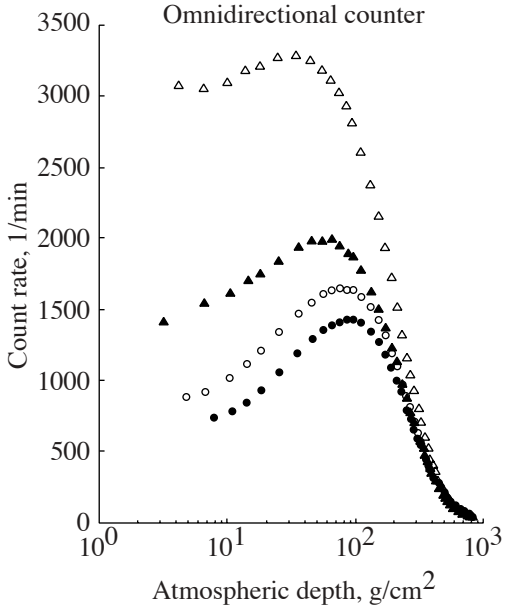

Figure 15. Atmospheric cosmic ray intensity at high latitude (triangles, Murmansk, R_c=0.6 GV) and intermediate latitude (circle, Alma-Ata, R_c = 6.7 GV) near solar minimum (open February 1987) and solar maximum (filled, September 1989). From Bazilevskaya and Svirzhevskaya (1998).

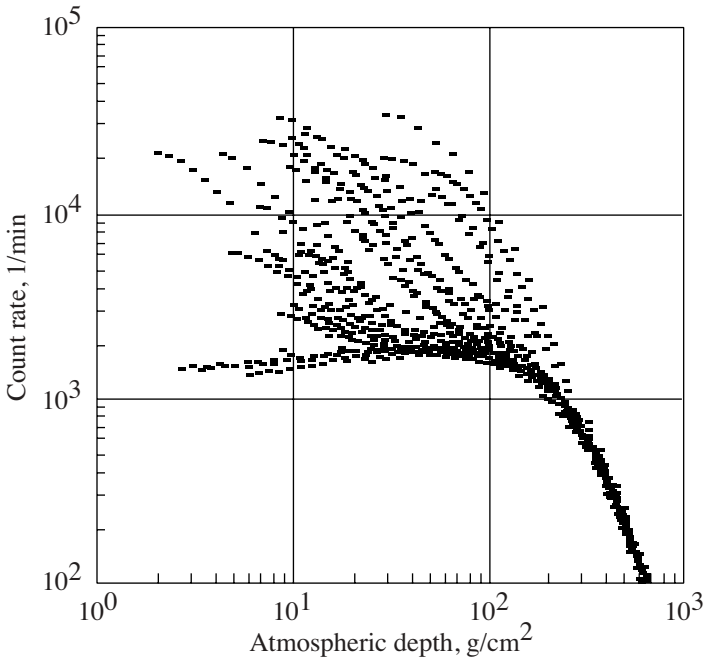

Figure 16. Atmospheric cosmic ray intensity during the October 1989 solar particle event (Bazilevskaya and Svirzhevskaya 1998).

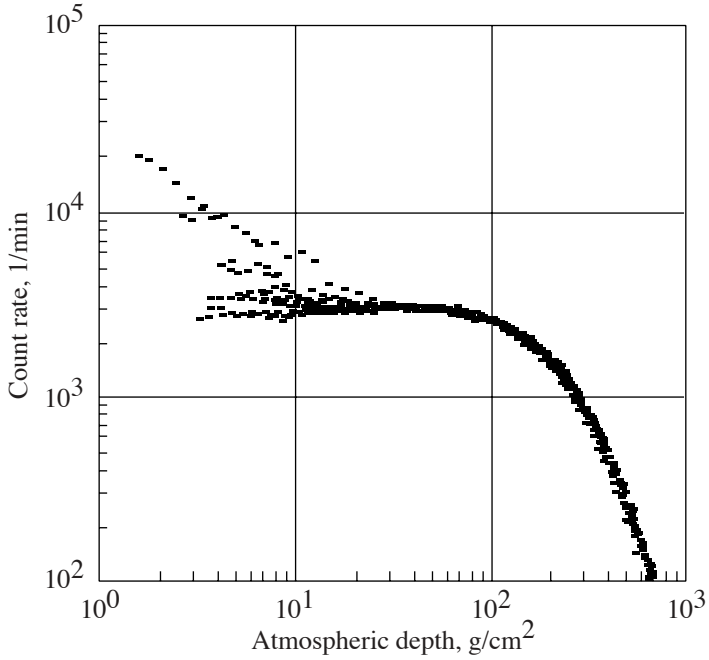

Figure 17. Magnetospheric electron precipitation event in May 1994 (Bazilevskaya and Svirzhevskaya 1998).

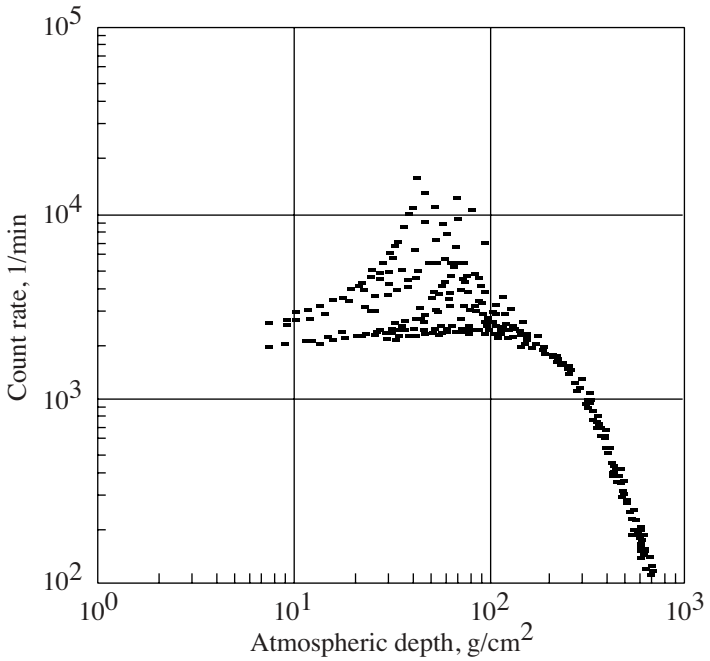

Figure 18. Atmospheric radioactivity following an atmospheric nuclear test in 1970 (Bazilevskaya and Svirzhevskaya 1998).

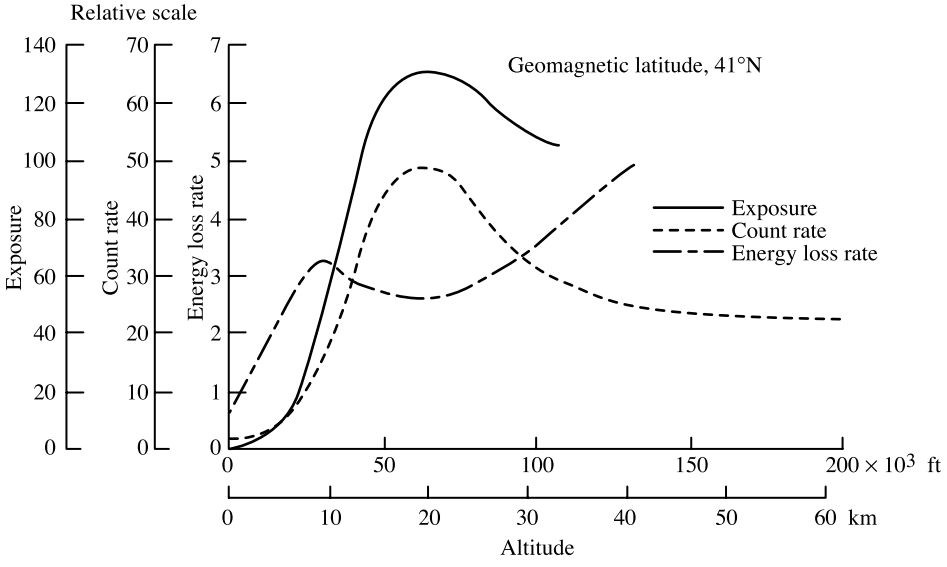

Figure 19. Ionization, counting rate, and average rate, and average rate of energy loss (proportional to specific ionization) (from Tobias, 1952).

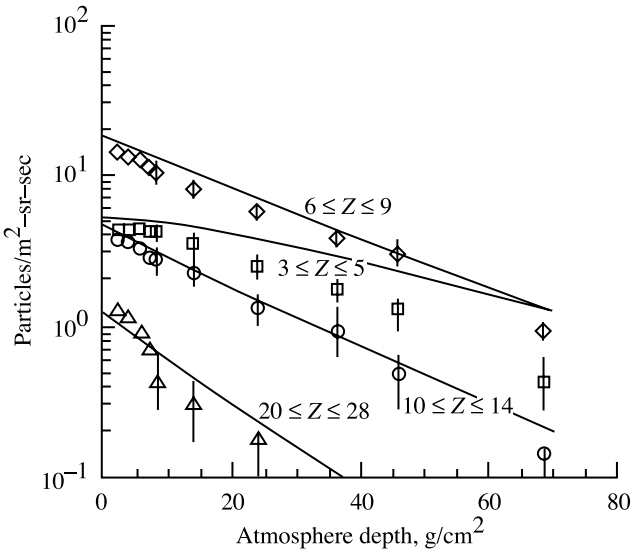

Figure 20. Vertical ion flux in upper atmosphere measured (symbols) by Webber and Ormes (1967) and calculated (lines) by Wilson et al. (1987).

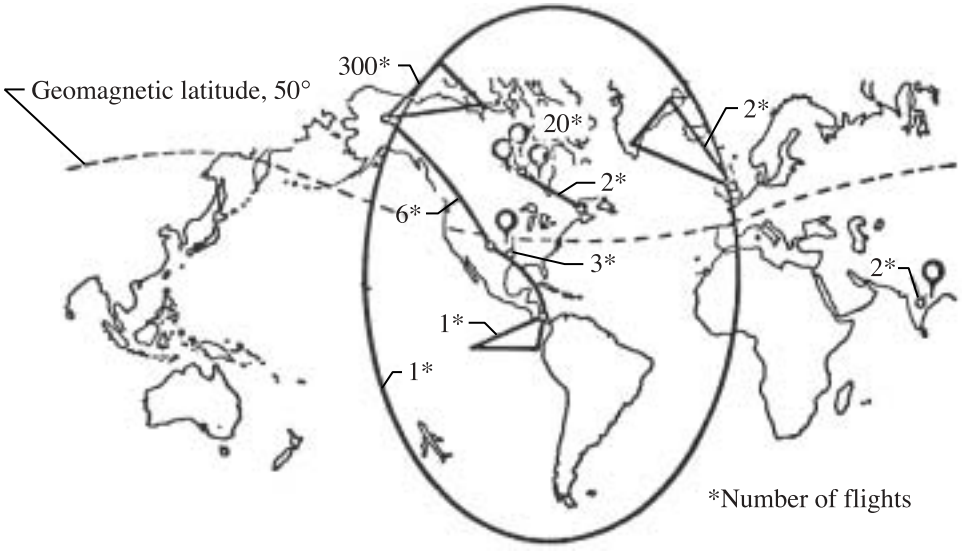

Figure 21. High-altitude radiation measurements made with neutron spectrometers and tissue equivalent ion chambers between 1965 and 1971 (Foelsche et al. 1974).

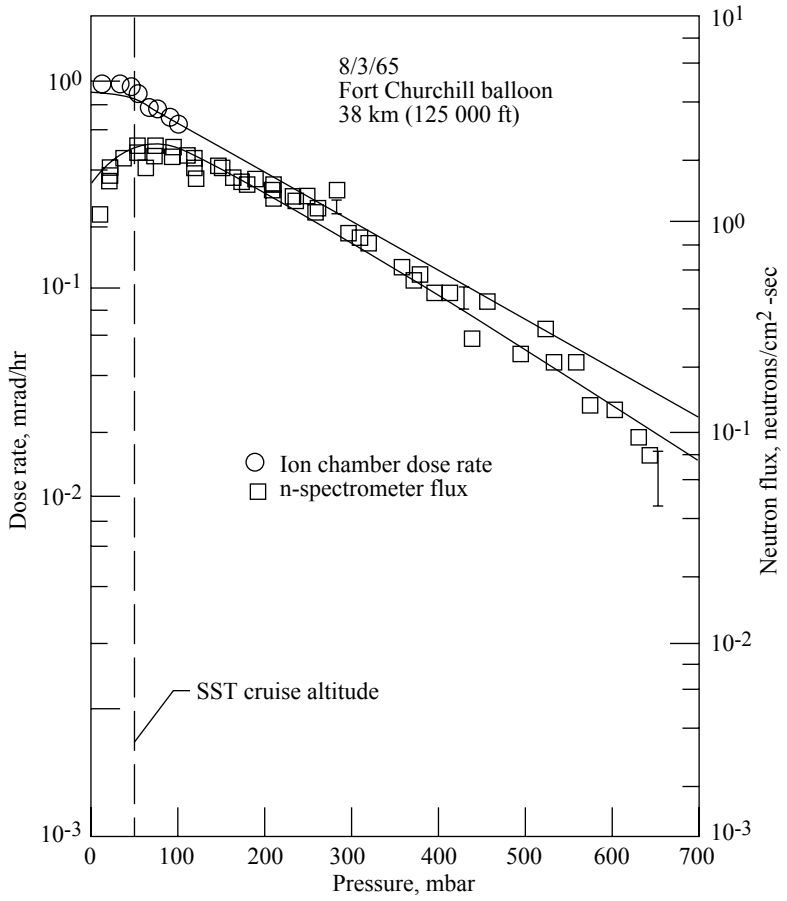

Figure 22. Galactic cosmic-ray maximum (August 3, 1965; 1 year after sunspot minimum: Fort Churchill, Canada; geomagnetic latitude ≈ 69º). Neutron flux from 1 to 10 MeV (right scale), and ion chamber dose rate (left scale) is a function of atmospheric depth (Foelsche et al. 1974). The solid lines are corresponding values from the AIR model (Wilson et al. 1991b).

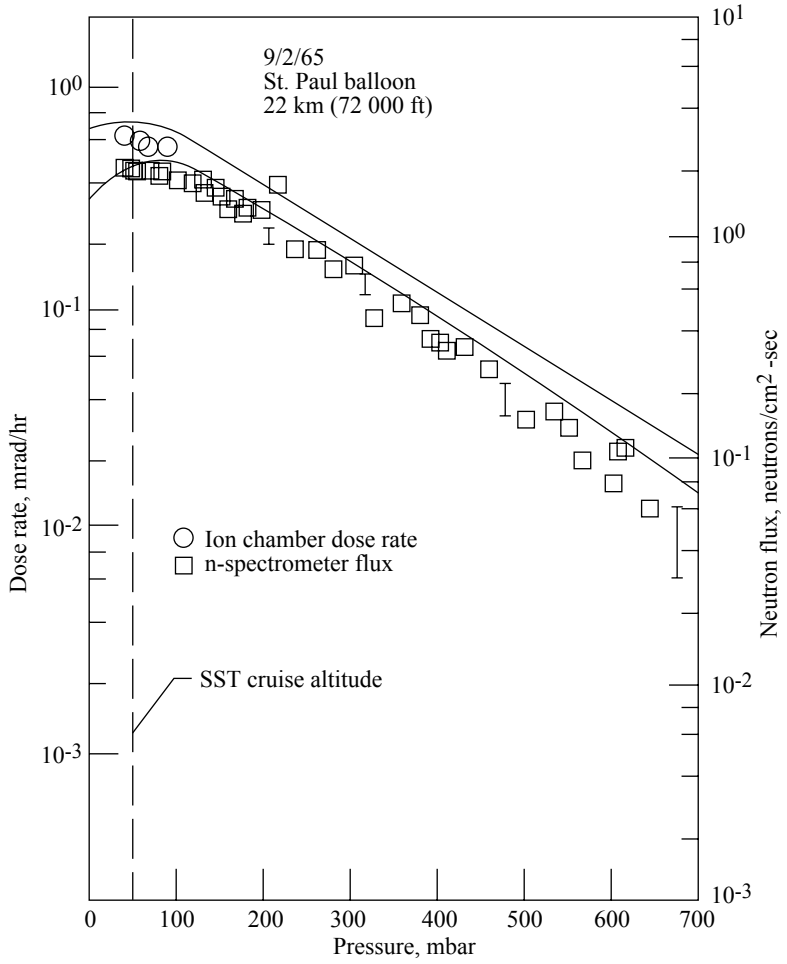

Figure 23. Galactic cosmic-ray maximum (September 2, 1965; St. Paul, Minnesota; geomagnetic latitude ≈ 55°). Neutron flux from 1 to 10 MeV (right scale), and ion chamber dose rate (left scale) is a function of atmospheric depth. Compare with data in figure 22 at higher latitude. (Foelsche et al. 1974) The solid lines are corresponding values from the AIR model (Wilson et al. 1991b).

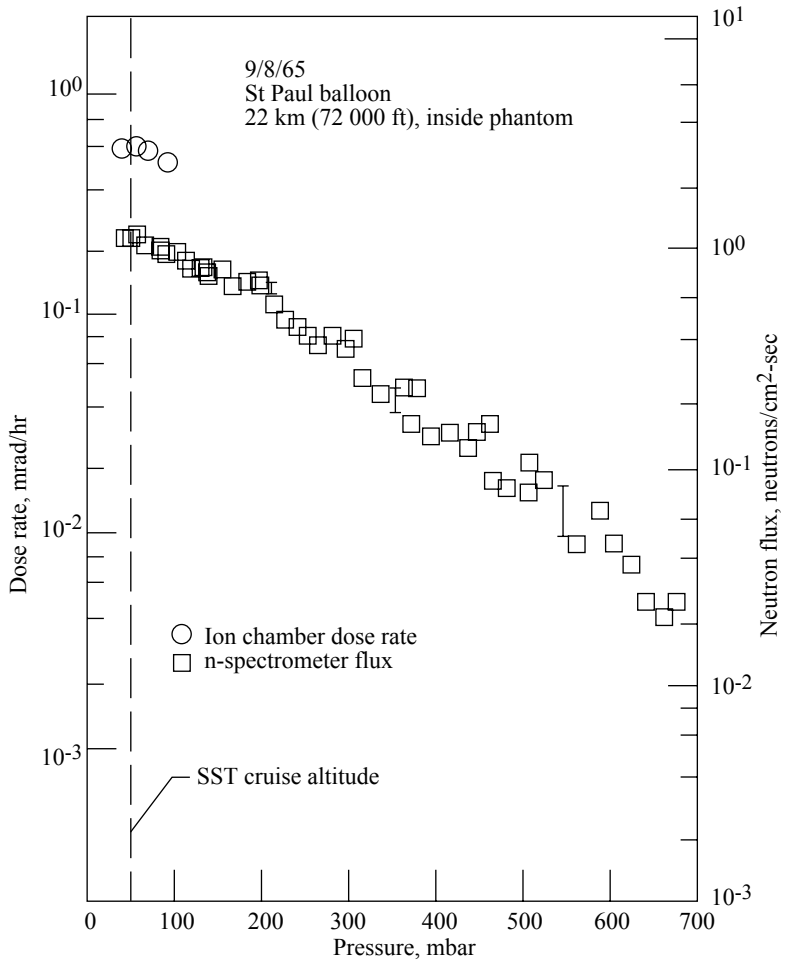

Figure 24. Galactic cosmic-ray maximum (September 8, 1965; St. Paul, Minnesota; geomagnetic latitude ≈ 55°). In flights of figures 22 and 23, the sensors were lightly shielded (less than 1 g/cm^2 of fiber glass and foam). In this flight, the sensors were surrounded by tissue equivalent material, including calcium, of about 15 g/cm^2 thickness to obtain an approximate measurement of the neutron fluxes and ion chamber dose rates in the center of the human body. (Foelsche et al. 1974)

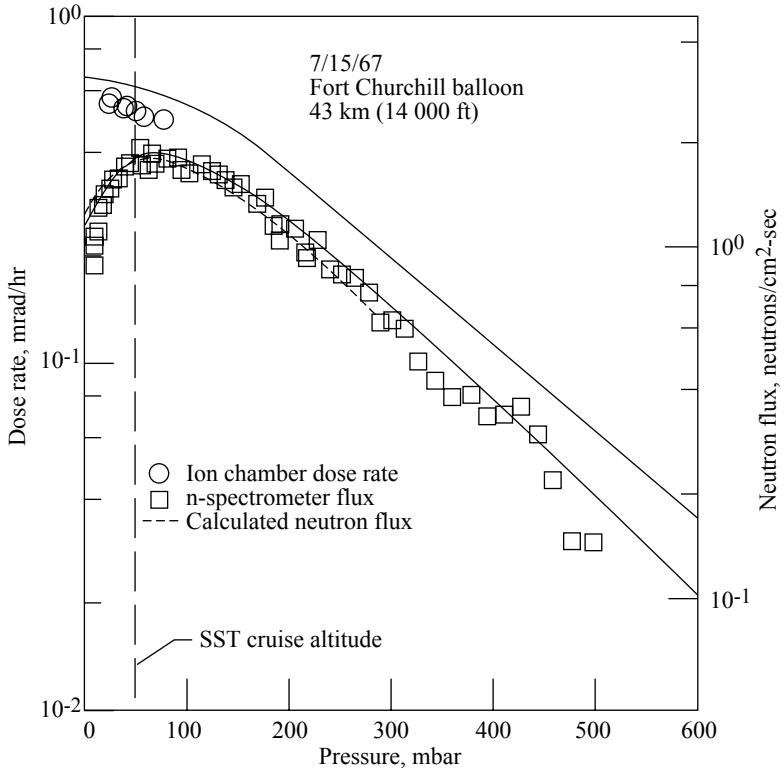

Figure 25. Galactic cosmic rays 2 years after galactic cosmic-ray maximum (July 15, 1967; Fort Churchill, Canada; geomagnetic latitude ≈ 69°). Compare with figure 22 for a flight at galactic cosmic-ray maximum. The neutron flux and ion chamber dose rate have both decreased about 25 to 30 percent at SST altitudes (solar modulation). The short-dashed line is the attitude dependence obtained by theory. (Foelsche et al. 1974) The solid lines are corresponding values from the AIR model (Wilson et al. 1991b).

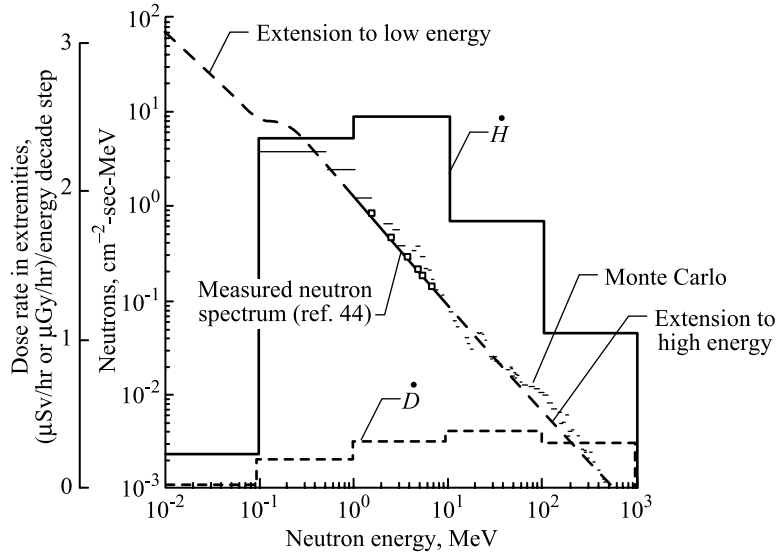

Figure 26. Neutron spectrum at 70,000 ft over Ft. Churchill on August 3, 1965. (Foelsche et al. 1974)

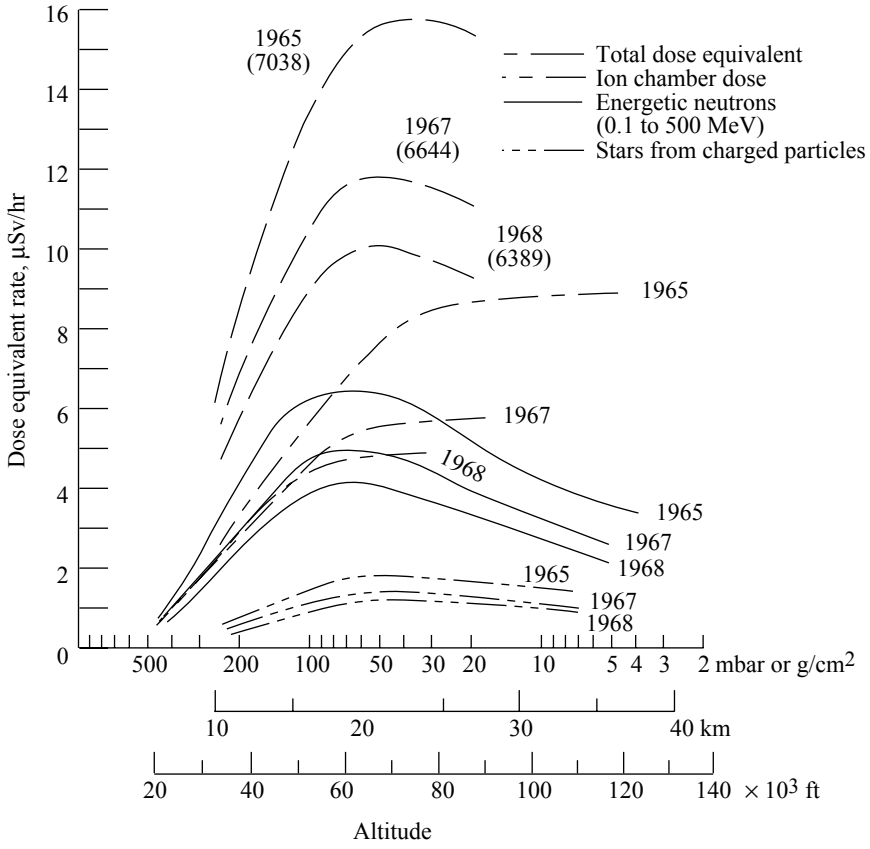

Figure 27. Galactic cosmic-ray dose equivalent rates for extremities (hands and feet) and approximately for eyes as a function of altitude at different phases of the solar cycle for high latitudes.

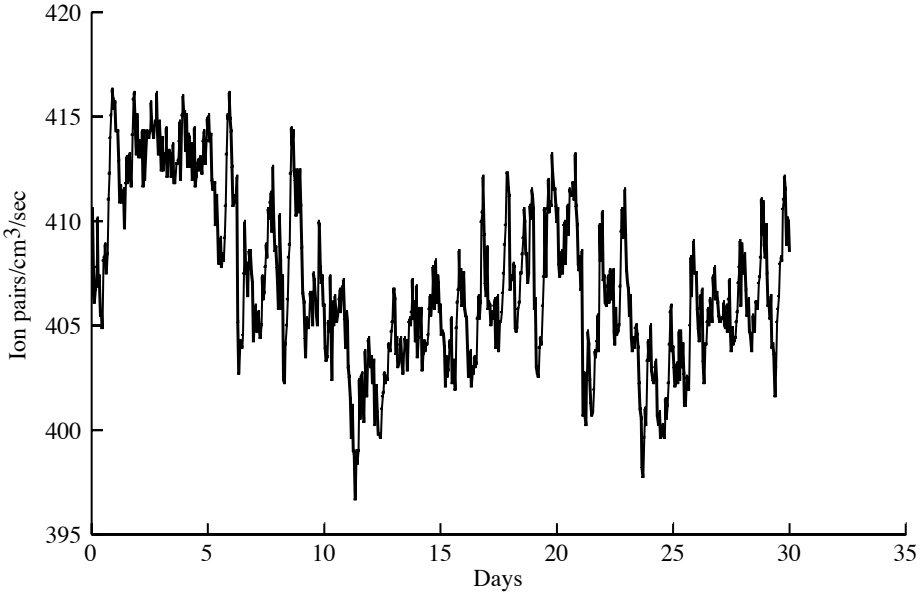

Figure 28. Ionization rate in the month of June, 1997, at 19.8 km near polar region. Atmospheric pressure is 55.2 mbar.

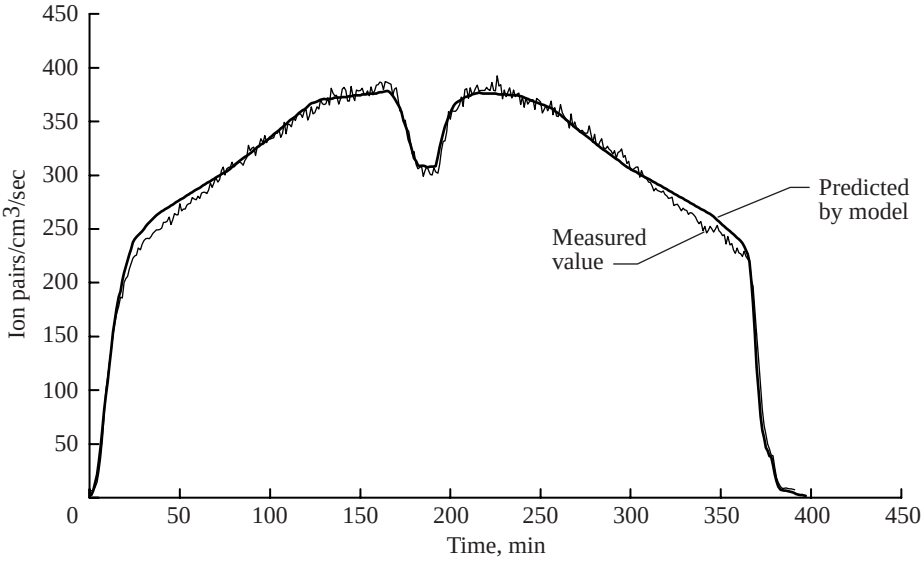

Figure 29. Predicted and measured (P. Goldhagen) values of air ionization rate as function of flight time for ER-2 flight on June 13, 1997. (See chapter 7).

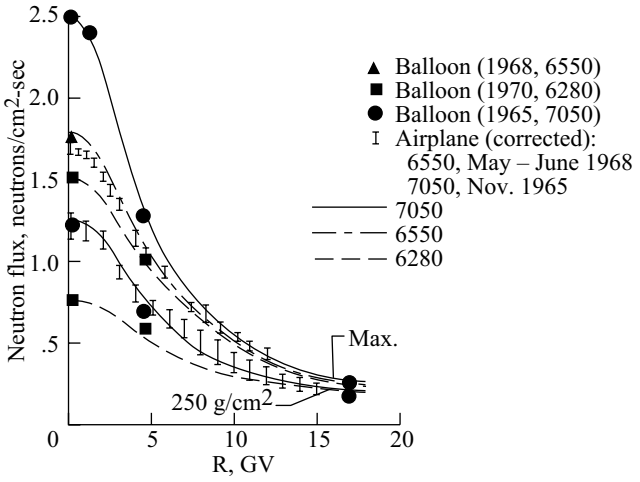

Figure 30. Fast neutron flux (in range from 1 to 10 MeV) at the transition maximum and 240-g/cm^2 depth as a function of vertical cutoff rigidity *R* for various times in the solar cycle and DRNM count rates.

H, mSv/1000 hr at 40 000 ft

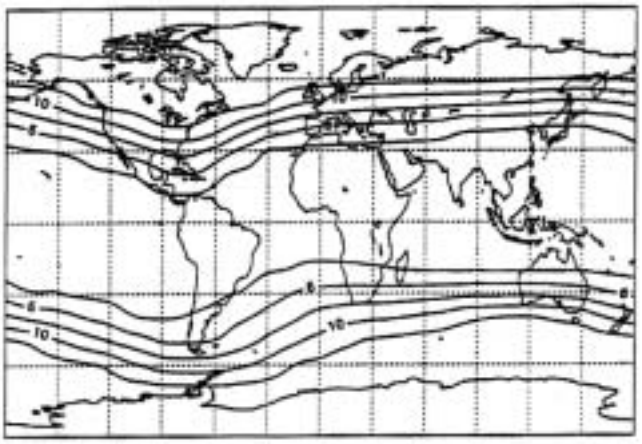

H, mSv/1000 hr at 50 000 ft

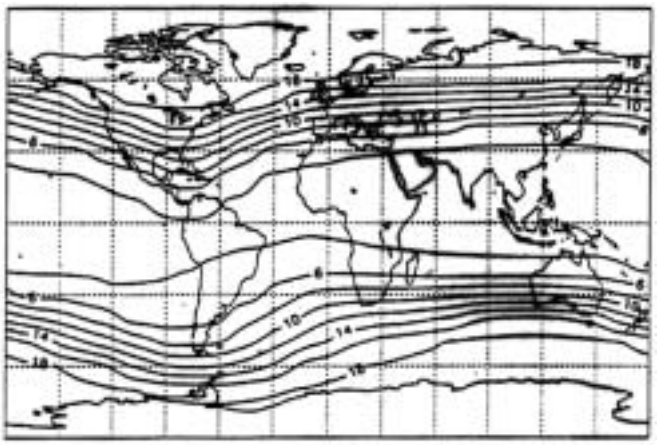

Figure 31. Background exposure levels in upper atmosphere at solar minimum (1965).

H, mSv/1000 hr at 65 000 ft

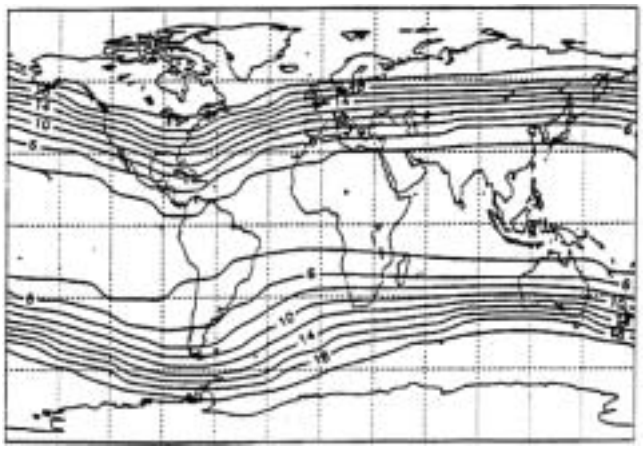

H, mSv/1000 hr at 73 000 ft

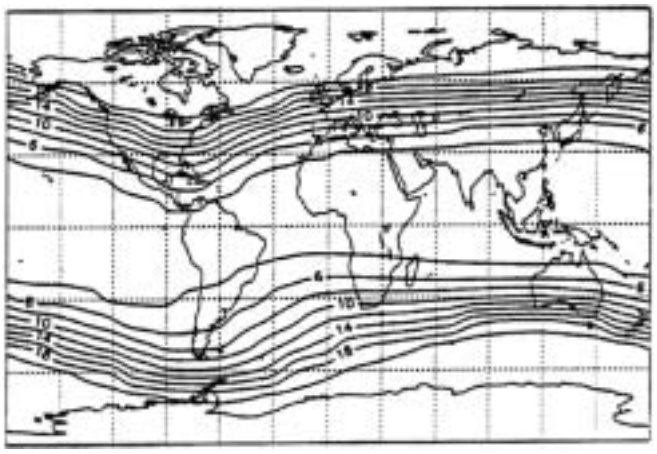

Figure 31. Concluded.

$(H_{sol})_{min}/(H_{sol})_{max}$ at 40 000 ft

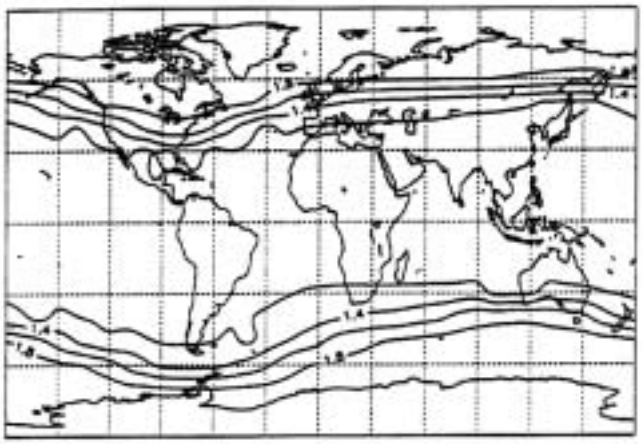

$(H_{sol})_{min}/(H_{sol})_{max}$ at 50 000 ft

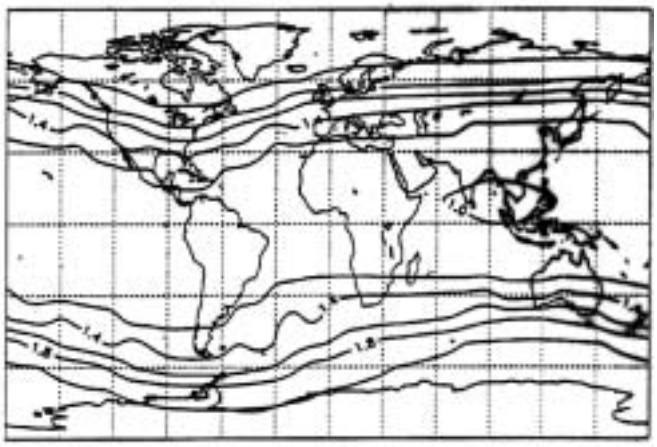

Figure 32. Maximum solar modulation ratio in atmospheric radiation levels.

$(H_{sol})_{min}/(H_{sol})_{max}$ at 65 000 ft

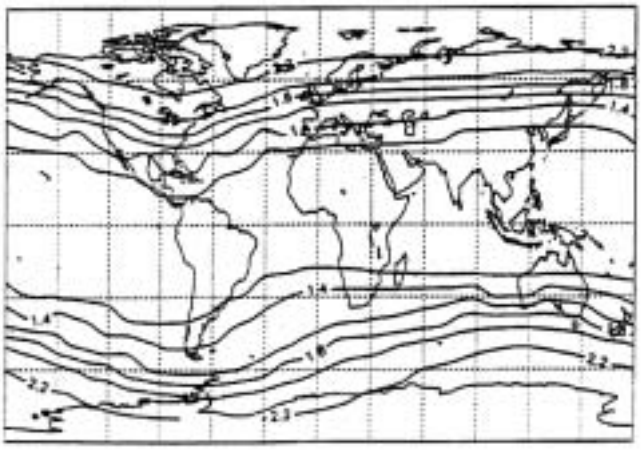

$(H_{sol})_{min}/(H_{sol})_{max}$ at 73 000 ft

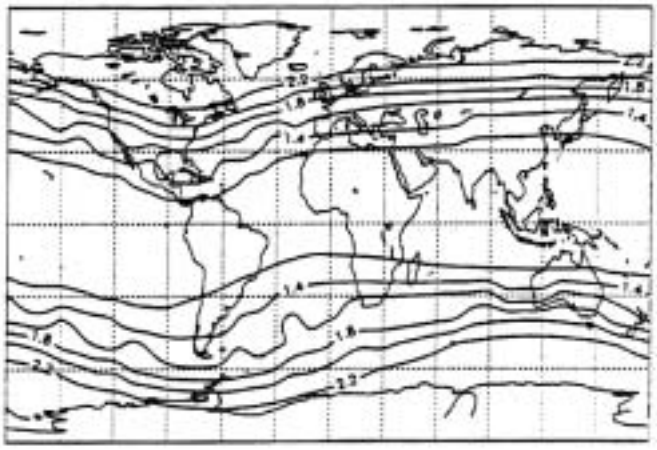

Figure 32. Concluded.

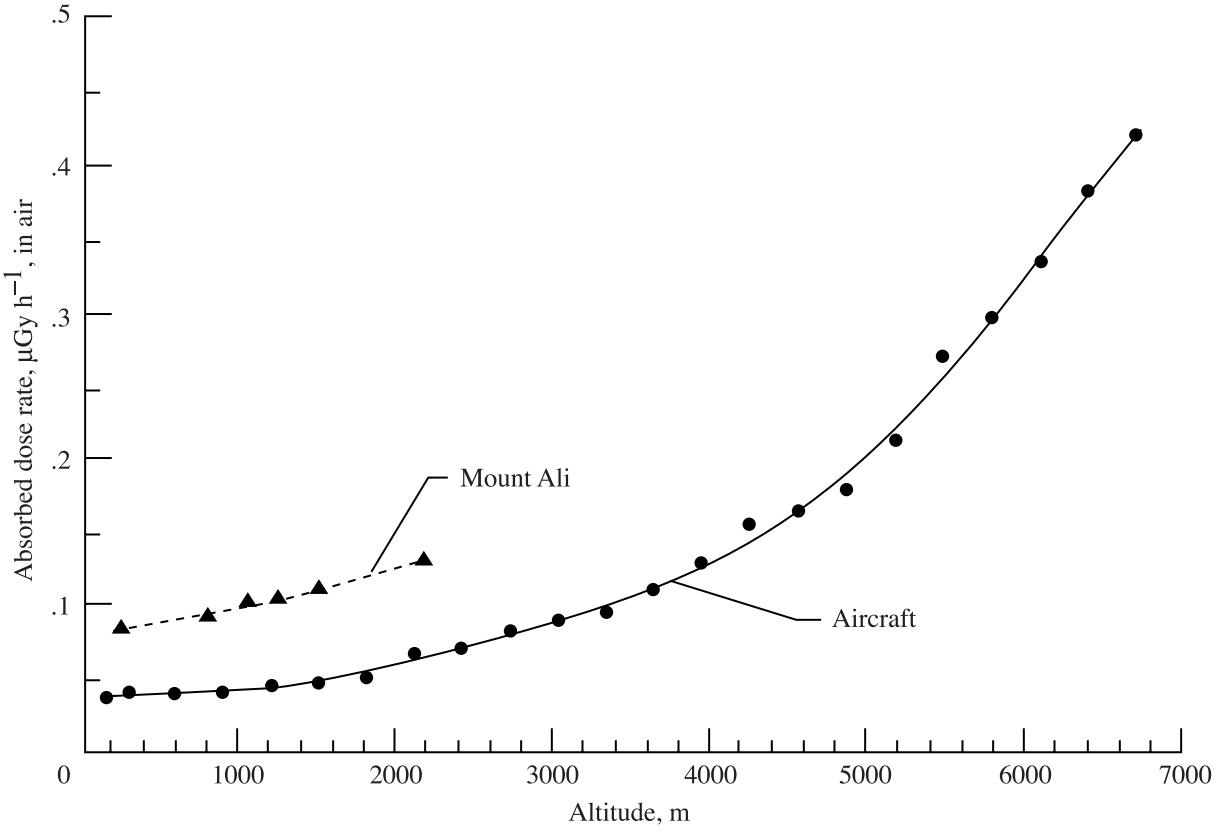

Figure 33. Measured absorbed dose rates on Mt Ali and in aircraft (Weng and Chen 1987).

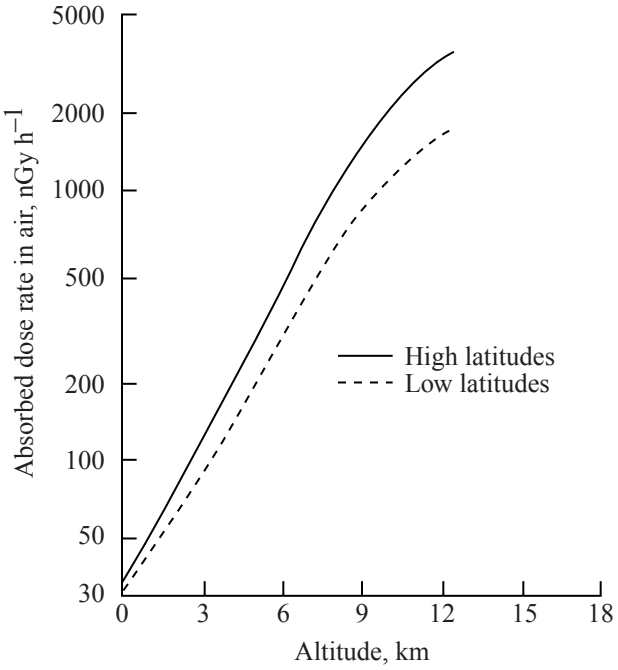

Figure 34. Absorbed dose rates in air as a function of altitude and geomagnetic latitude. (Hewitt et al. 1980)

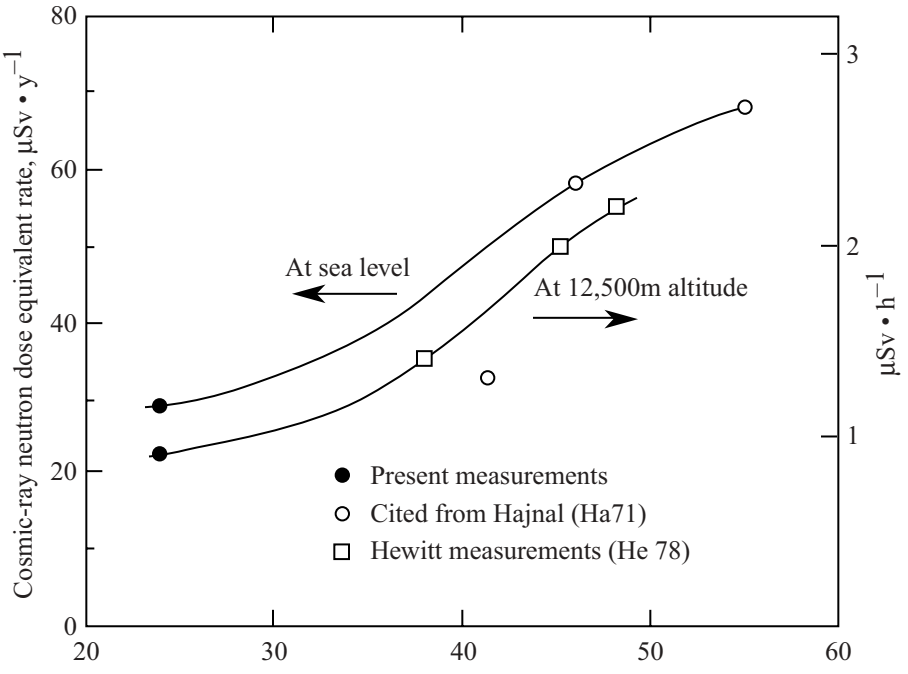

Figure 35. Measured neutron dose equivalent rate at various geomagnetic latitudes in the Northern Hemisphere. (Nakamura et al. 1987).

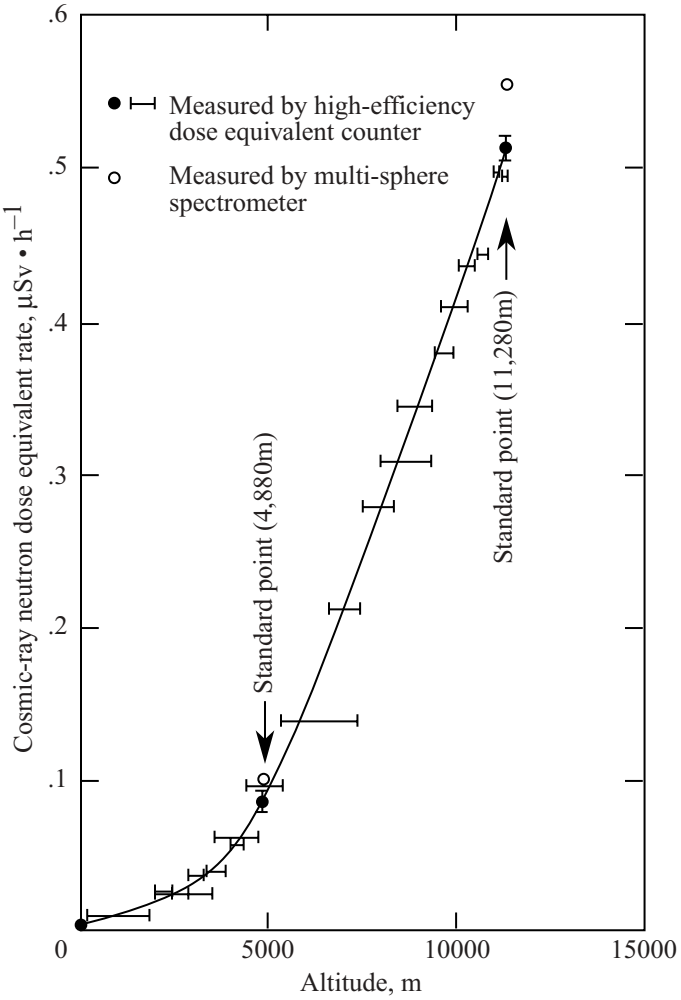

Figure 36. Altitude variation of neutron dose equivalent rates measure by the high-efficiency neutron dose equivalent counter. (Nakamura et al. 1987)

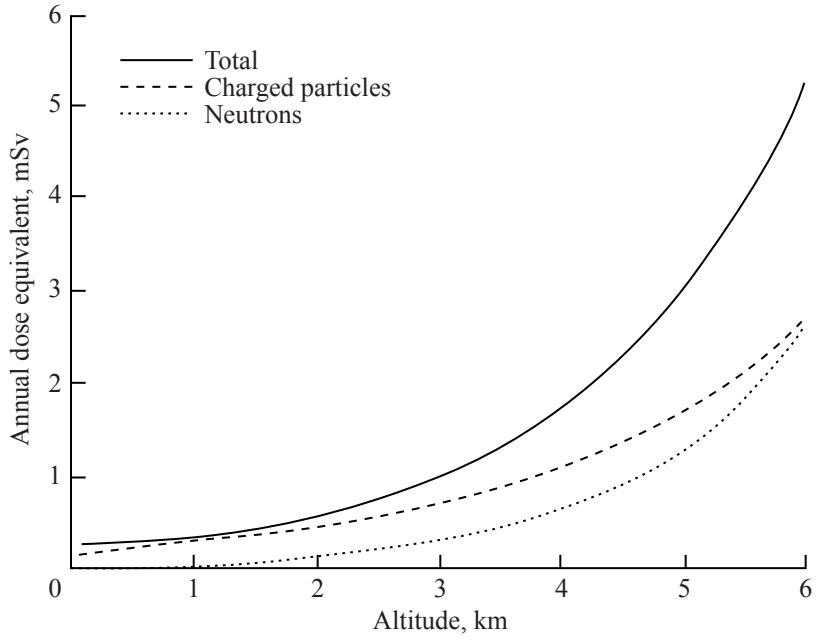

Figure 37. Variation of the annual effective dose equivalent from the Ionizing component and the neutron component of cosmic radiation as a function of altitude. (Bouville and Lowder 1988)

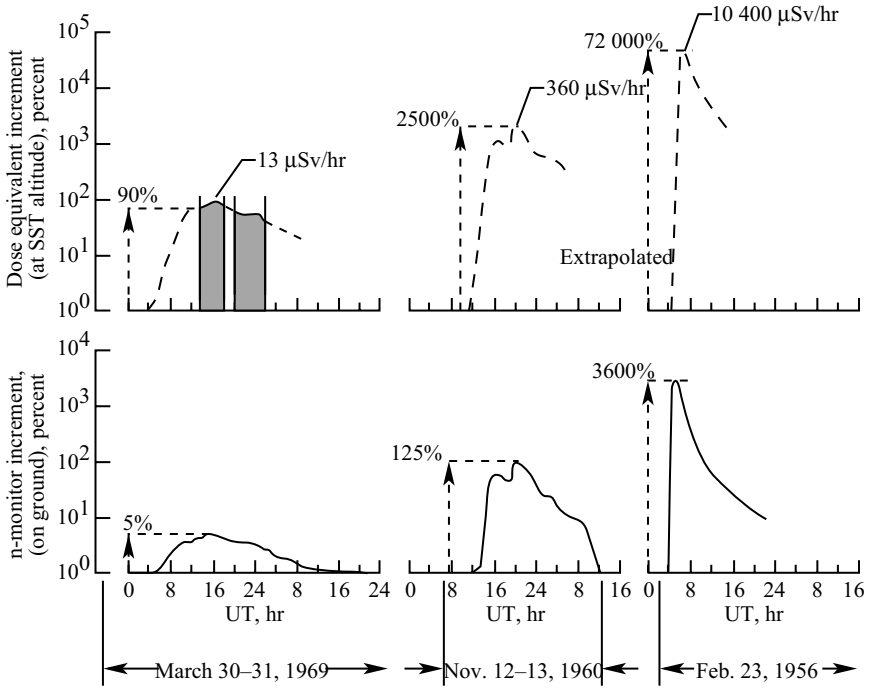

Figure 38. Energetic solar events measured on the ground and at SST altitude (Foelsche et al. 1974).

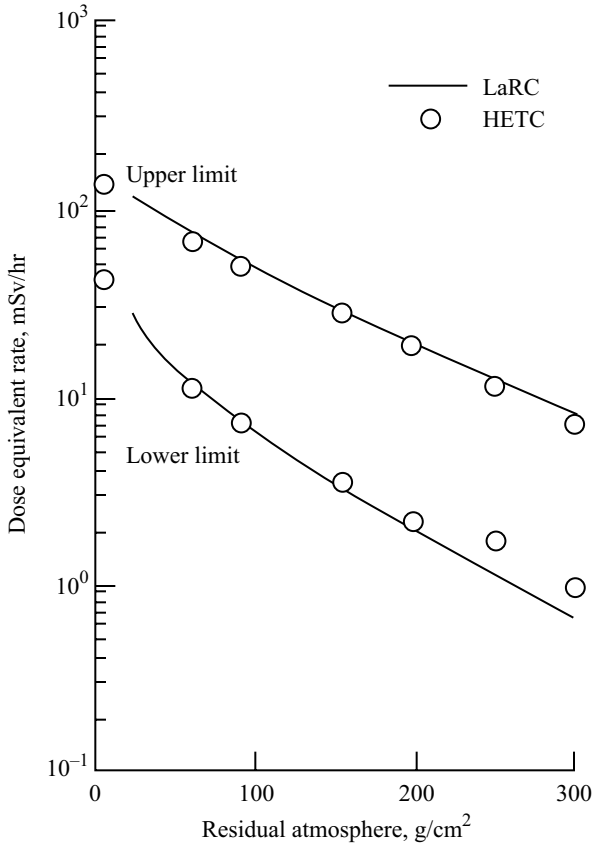

Figure 39. Calculated upper and lower limits for dose equivalent rate at high latitude for the Feb. 23, 1956 event (Foelsche et al. 1974).

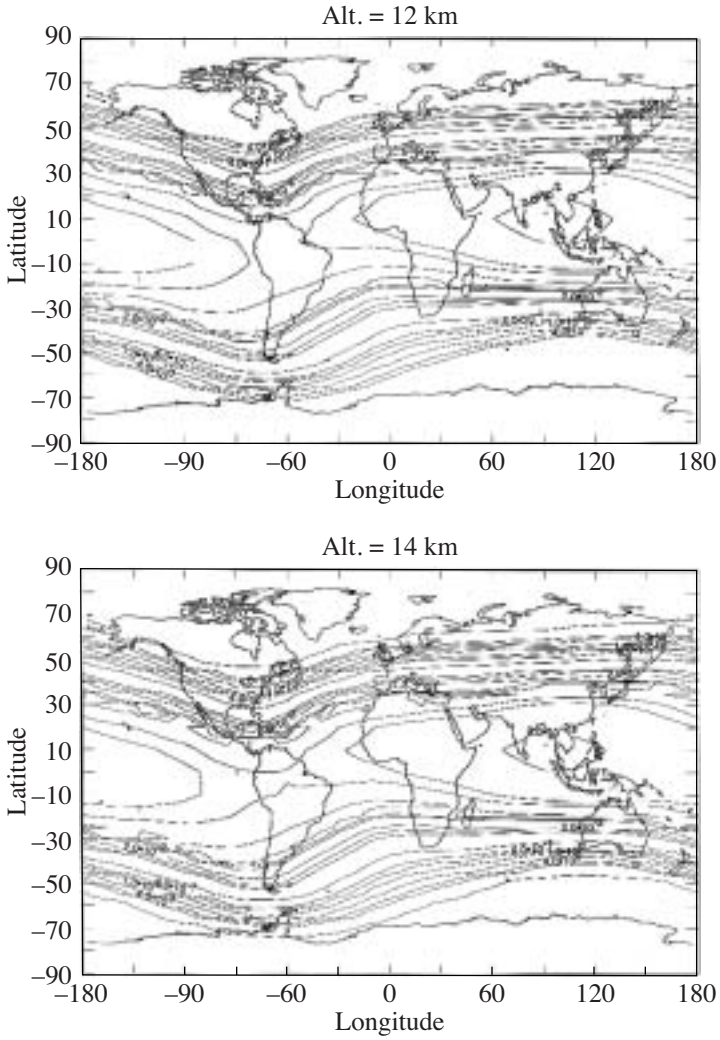

Figure 40. Global distribution of dose equivalent rate (mSv/h) at 0420 UT on Feb. 23, 1956 at various altitudes.

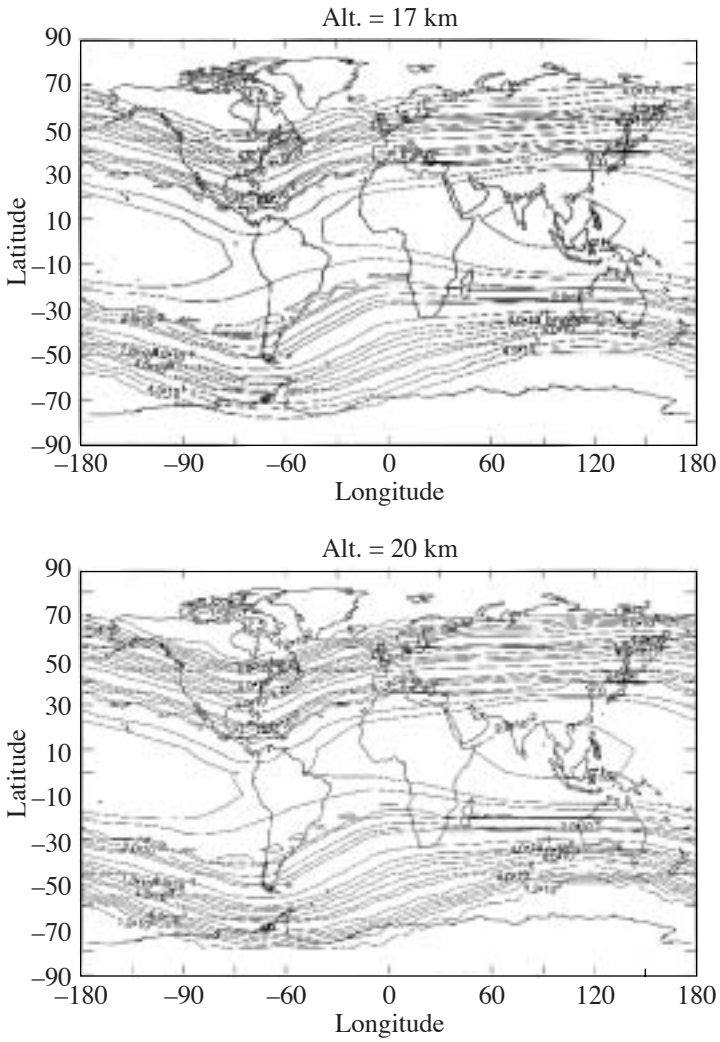

Figure 40 Concluded.

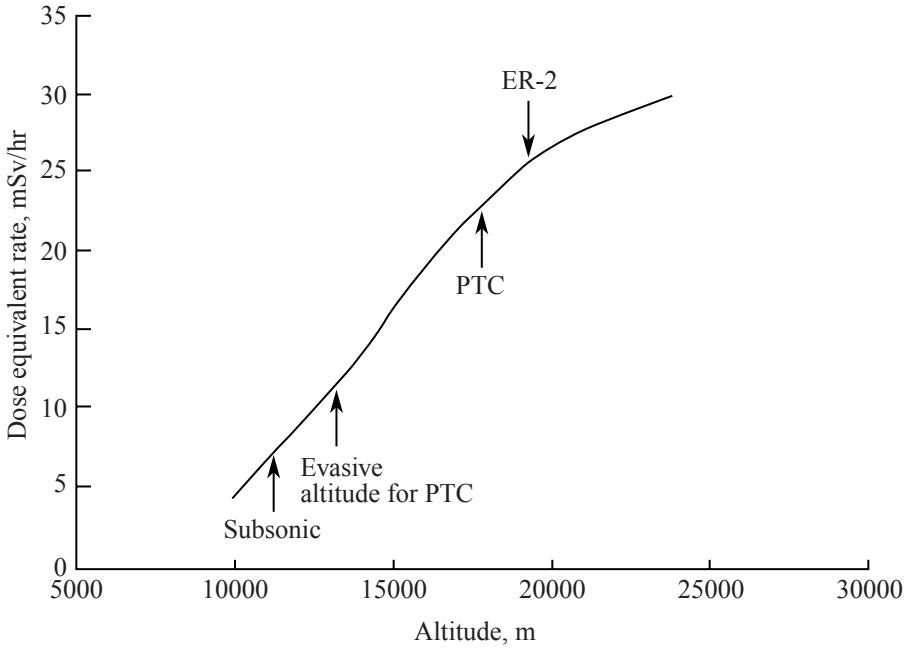

Figure 41. Dose equivalent rate at 55N 30W on Feb. 23, 1956 at 0410 UT.

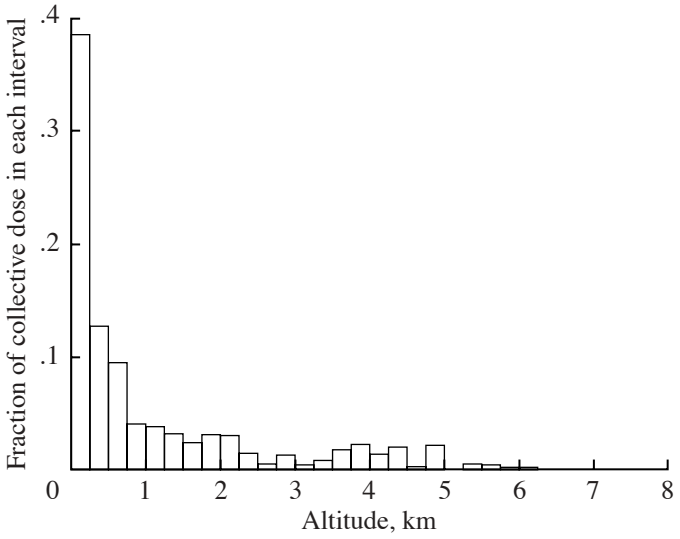

Figure 42. Distribution of the collective effective dose equivalent form cosmic radiation as a function of altitude (Bouville and Lowder 1988).

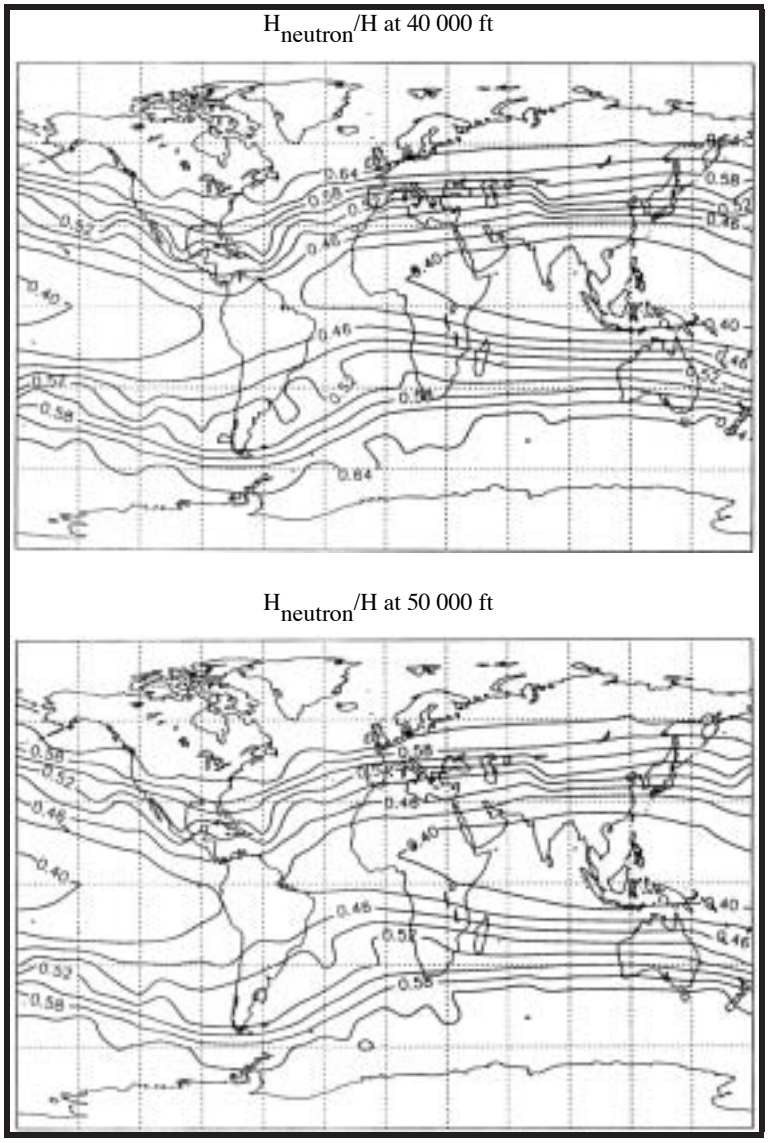

Figure 43. Fraction of dose equivalent due to neutrons at solar minimum (1965).

$H_{neutron}/H$ at 65 000 ft

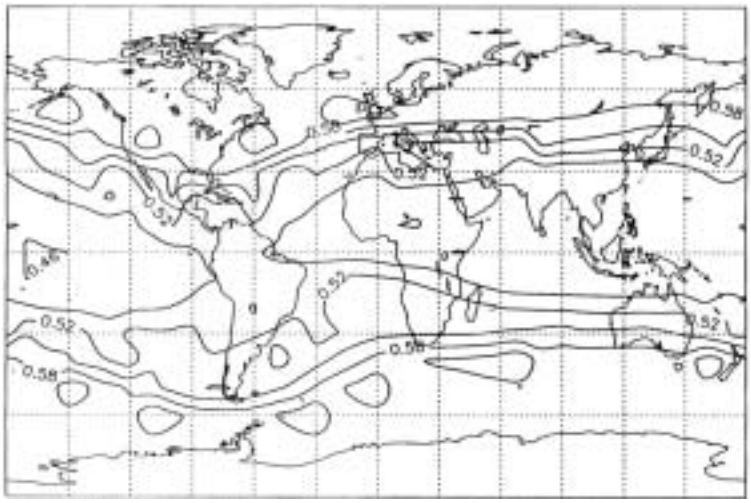

$H_{neutron}/H$ at 73 000 ft

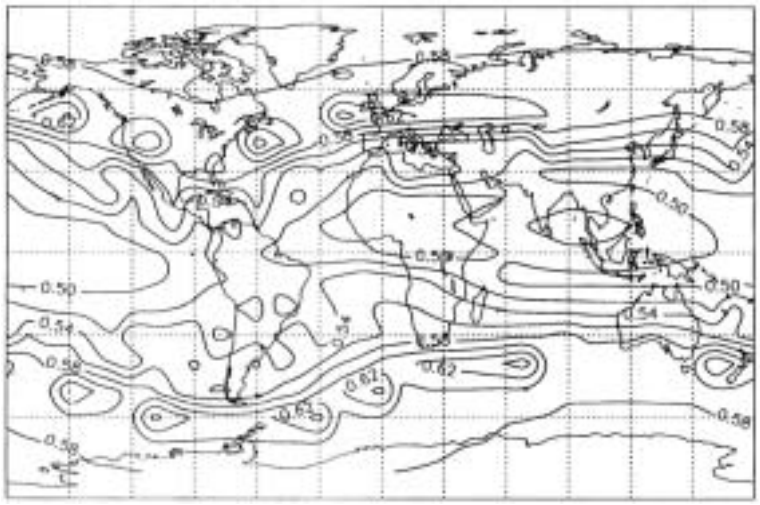

Figure 43. continued

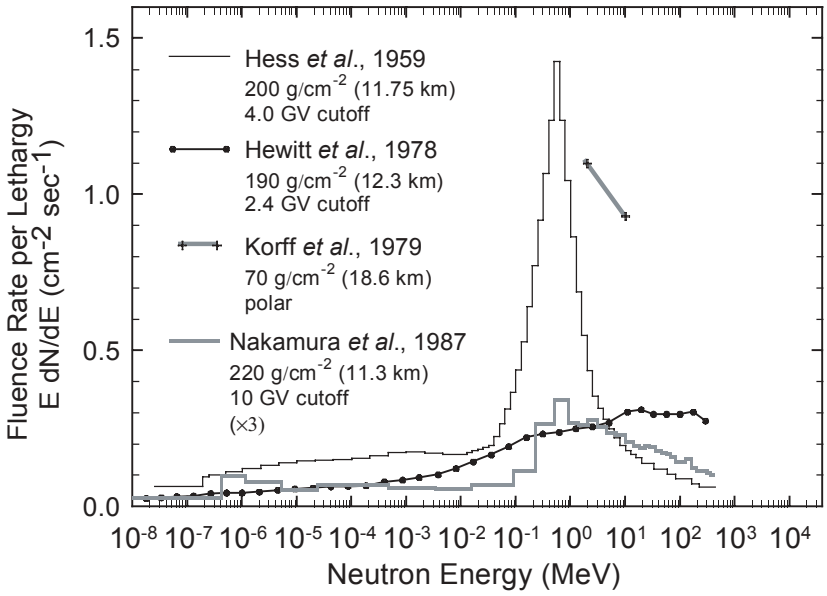

Figure 44. Cosmic-ray neutron spectra measured at jet airplane altitudes before 1997.

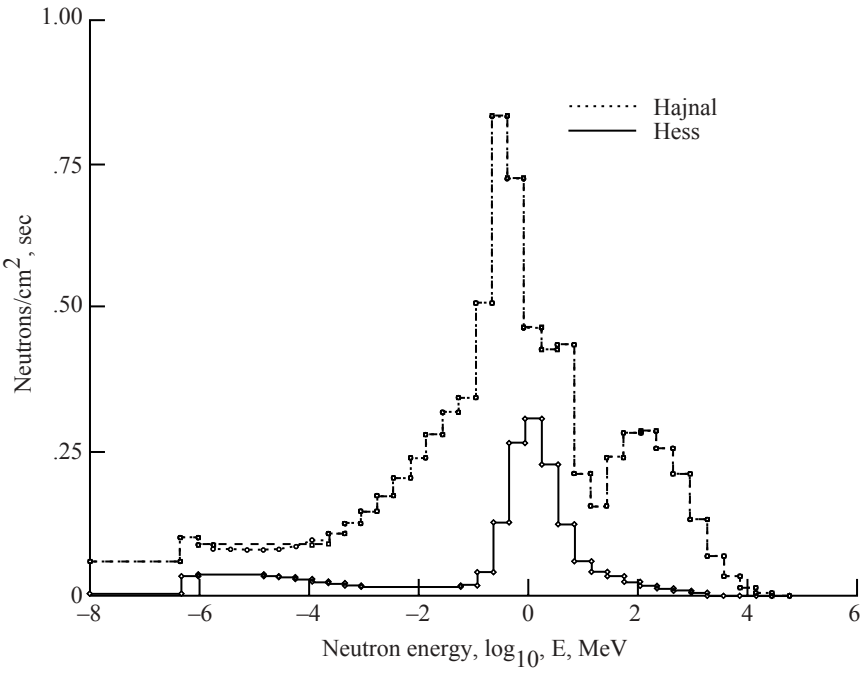

Figure 45. Hajnal unfolded neutron spectrum from Hewitt data measured at 17.46°N at 23.5 km compared to Hess spectrum.

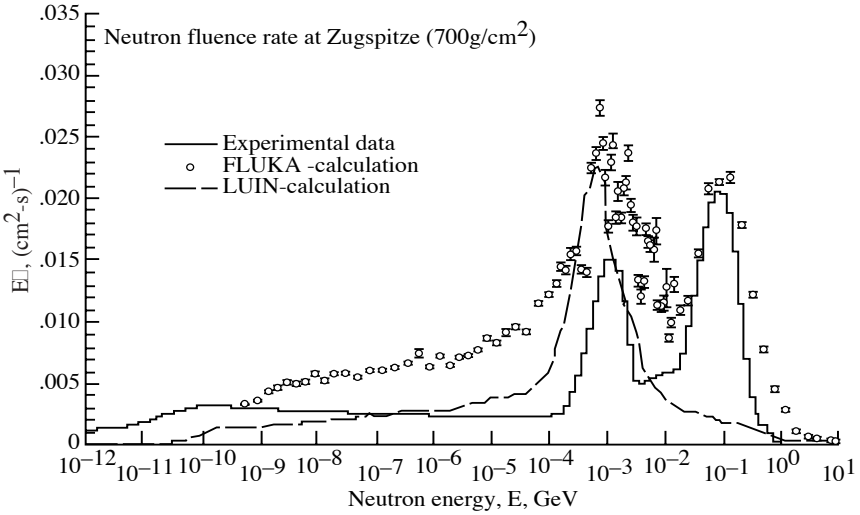

Figure 46. Spectral neutron fluence rate obtained by measurements and calculations on top of Zugspitze (by permission of Schraube et al. 1998).

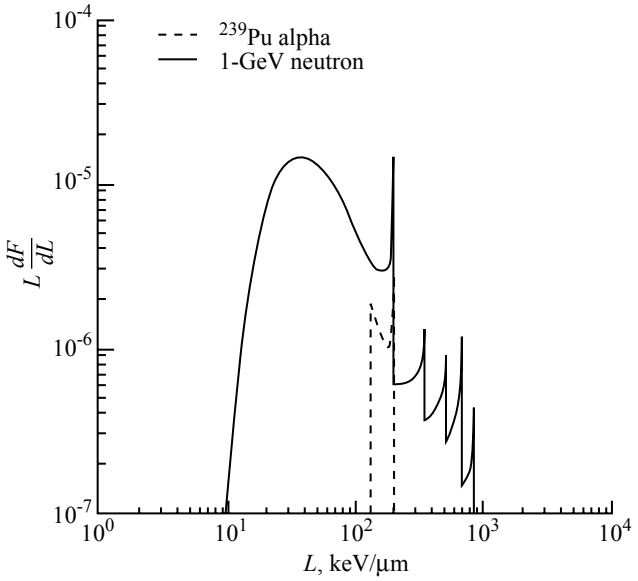

Figure 47. LET distribution porduced by 1-GeV neutron in tissue along with 239-Pu alpha decay spectrum.